LEVERAGING OPTO-MECHANICS TO DESIGN HIGH PERFORMANCE RF OSCILLATORS

A Dissertation

Presented to the Faculty of the Graduate School

of Cornell University

in Partial Fulfillment of the Requirements for the Degree of

Doctor of Philosophy

by

Siddharth Gurunath Tallur

January 2014

LEVERAGING OPTO-MECHANICS TO DESIGN HIGH PERFORMANCE RF OSCILLATORS

Siddharth Gurunath Tallur, Ph.D.

Cornell University 2014

Reference oscillators are ubiquitous elements used in almost every electronics system today. The need for miniaturized, batch manufacturable oscillators as chip-scale timing references arises from the quest to replace the well-established, high performance yet expensive quartz-based oscillators, without compromising performance. The electrical specifications of an oscillator depend on the application it serves, which has resulted in a variety of different mainstream oscillator technologies. Consumer RF applications can broadly be classified mechanical oscillators and electrical oscillators. In mechanical oscillators, the frequency selective element is a mechanical resonator, and typically quartz is the material of choice for high-end applications. For less demanding and cost-sensitive applications, micro-electromechanical (MEMS) resonators, being CMOS compatible and high quality factor resonators, offer a unique set of parameters well-suited for oscillator design. Electrostatic capacitive transduced silicon resonators and piezoelectric transduced thin film bulk acoustic resonators (FBARs) are commercially available for MHz range and GHz range applications respectively. Scaling MEMS oscillators to higher frequencies presents challenges in terms of reduced transduction efficiencies and material limitations on quality factors. Opto-mechanical transduction offers higher sensitivity and opens up possibilities to interrogate high frequency mechanical resonances hitherto inaccessible. The focus of this thesis is to leverage opto-mechanical transduction to design high frequency high performance MEMS

oscillators and exploring various designs and fabrication techniques to realize these devices.

This disertation explores two classes of oscillators, namely the opto-mechanical and opto-acoustic oscillators. The former oscillator type exploits parametric amplification and does not require external electrical feedback to sustain oscillations, thus doing away with a dominant noise source. To eliminate coupling environmental noise to the oscillation signal, the opto-mechanical resonator was fabricated on a silicon nitride chip with waveguides and grating couplers integrated on to the same chip. The device was used to demonstrate self-sustained mechanical oscillations at 41MHz with phase noise -91dBc/Hz at 1kHz offset from carrier. The integrated design results in immunity of the oscillation signal from environmental flicker noise. Designing low phase noise opto-mechanical oscillators for GHz range frequencies is very challenging, the limitations being mainly imposed by the efficiency of the optical drive scheme. A design worth exploring to overcome this limitation is the acousto-optic modulator designed and developed in the OxideMEMS lab, which marries the highly sensitive optical sense scheme with electrostatic capacitive transduced drive scheme. Operating the modulator in a feedback loop as an opto-acoustic oscillator has been realized by using the device as an intensity modulator. However the two-coupled opto-mechanical resonator design cannot be successfully scaled to design an oscillator at frequencies beyond GHz. An alternative efficient transduction scheme of interest for GHz range MEMS resonators is partial air gap capacitive transduction. Exploiting partial air-gap transduction using alumina in addition to designing an array of resonators employing a micromechanical displacement amplifier, an opto-acoustic oscillator employing a higher order radial mode at 2.1GHz was demonstrated. The oscillator has RF output power of +18dBm and phase noise -80dBc/Hz at 10kHz offset from carrier. The

inherent non-linearity of the opto-mechanical modulation based sensing generates oscilllation harmonics all the way up to 16.4GHz with greater than -45dBm signal power. A detailed phase noise model for such oscillators was derived and insights derived from the model were followed to identify appropriate photo-detectors to lower the far-from-carrier phase noise by 15dB. Fabrication techniques developed along the way were also used to design other interesting opto-mechanical devices for electromechanical detection of optical modulation and to study acousto-optic frequency modulation. In summary, the overall focus of this work is to bring together MEMS and photonics techniques and devices in ways that address long-standing needs in both communities.

BIOGRAPHICAL SKETCH

Siddharth Tallur was born in Mumbai, India to Mr. Gurunath Tallur and Mrs. Shantala Tallur on 21^{st} May 1986. He finished schooling at Smt. J. B. Khot High School in 2002 and D. G. Ruparel College of Science in 2004. He graduated with a B.Tech. in Electrical Engineering at IIT Bombay in 2008. His joined the OxideMEMS Lab at Cornell University in December 2009, where his work primarily focused on designing low phase noise RF opto-mechanical and opto-acoustic oscillators with a novel approach towards bringing together MEMS and photonic resonators. Prior to joining Cornell University, he was serving as a Business Analyst at the global strategy consulting firm A.T.Kearney Ltd. in their Mumbai office. Outside the cleanroom and laboratory, he presided over the activities of the Electron Devices Society (EDS) during August '11 - May '13 . His work on electro-opto-mechanical frequency modulation was the recipient of the best student paper award at the IEEE Photonics Conference 2012 held in Burlingame, California, and was recognized by the U.S. Advisory Committee to the International Commission for Optics (USAC/ICO). He has also won the Cornell ECE Director's 2013 Best Thesis Research Award for his doctorate thesis. He has also worked with the ApselLab in Cornell University and co-authored several papers on design and characterization of a low power ultra wide band (UWB) impulse radio transceiver. In addition to his research interests, he enjoys long distance running and has a keen interest in music.

To Ma and Pa,

whose wisdom and love I am only now beginning to understand.

ACKNOWLEDGEMENTS

It is customary to start the acknowledgments section of a thesis by offering gratitude to your advisor for all the support and guidance he/she has given you during the course of your doctorate studies. However if I choose to go down that route, I would have to write a separate book about all that Sunil has done for me. Perhaps I'll write one someday; a few sentences here will not do any justice to your kindness, your dedication, and to the wonderful friendship we share, that I am immensely fortunate to have discovered. I'll only say that if I ever end up becoming even half as good a man as you are, I will consider my life well lived.

I have been blessed with very good teachers since childhood, with my teachers at Cornell being the finest and the most influential in all walks of my life. Prof. Alyssa Apsel first introduced me to Cornell by inviting me for a summer internship in 2007, and later welcomed me into the Ph.D. program in 2009. Thank you for opening up this wonderful world to me. Prof. Ehsan Afshari rekindled my lost love for circuit design and it was a treat to learn from him and to watch him teach and educate. We shared plenty of very useful discussions that continued from the course office hours right through my Ph.D. Thank you for being a constant source of guidance and for the invaluable inputs you have always provided on my research - they have served as beacons that directed me towards the "bigger picture" whenever I was overwhelmed by miniscule details. I am also extremely grateful to Prof. Farhan Rana for sharing his wisdom with me. Your emphasis on rigor and attention to each and every detail always pushed me to attempt to do better than what I thought I could. Apart from providing insights and priceless comments on my research, you were also very generous to pitch in with all possible support when I was personally facing an uphill task in managing the affairs of the Electron Devices Society (EDS) - I have gained tremendously from our interactions,

and I shall always strive to uphold all that I have learnt from you and cherish it throughout my life. I also thank Prof. Alexander Gaeta for serving on my thesis committee. I also sincerely wish to thank Prof. Al Molnar, Prof. Amit Lal, Prof. Tsuhan Chen, Prof. Greg Fuchs and Prof. Mukund Vengalattore for the countless discussions and interactions we have shared that have gone long ways in making my stay at Cornell a valuable learning experience.

Isaac Newton once quoted Bernard of Chartres in a letter to Robert Hooke - "If I have seen further it is by standing on the shoulders of Giants". In my stay at Cornell, I came across three very tall giants, standing on whose shoulders I was able to not only attain sight of once distant goals, but their constant support, friendship and camaraderie meant that the strides taken towards achieving them felt more as pleasure and seldom as pain. Rajeev and Xiao mentored me through the first few months of my Ph.D., arguably the toughest phase for any graduate student. You have ever since served as ideals and still continue to do so. Later Suresh molded me entirely into the researcher that I am today - his proclivity for self-learning exhibited itself in a unique fashion as he refused to spoon-feed me and nudged me to think smartly and critically, firing probing questions at any loosely made comment or guesstimate, and solely trained me in performing experiments (lab) and cleanroom processing (fab). Thank you for always being there more as a brother than as a friend, and your happy attitude is something that I still continue to seek to attain.

To take credit for my research alone would be foolish - none of it would have been possible without the support of the OxideMEMS family. Dana and I overlapped very little as students at Cornell, but it is always very comforting to know that I can rely upon your support whenever I need it. Eugene personifies quintessential engineering excellence - it was an amazing experience working

with you at Cornell, and I can't wait to resume our association at Analog Devices. After Suresh and Eugene graduated, Tiffany has always been there as a senior graduate student/fortress - the one you look up to when all hope is lost. Thank you for teaching me what endurance means, and for never once refusing to help with debugging setups whenever I asked. Laura always reminds me that happiness is really a state of mind, and if you choose not to be bogged down by challenges then it is certainly possible. I very much look forward to carrying forward this teamwork at Analog Devices. David was always around to provide feedback and point out holes in any ideas and I am thankful for the support you provided in my initial days in the group. Ryan seems to know everything there is to know, thank you for knowing everything and sharing your knowledge whenever I hit a roadblock in my thinking. I cannot imagine the last four years without Suresh, Ajay and Tanay - your friendship and assistance meant a lot to me and helped me overcome all challenges. Maybe I'll write another book for you as well. Jon and Matt have certainly made the last few months at Cornell very enjoyable and made sure that I will definitely miss the group and our student office.

I have learnt a lot from Prof. Tal Carmon and his group at U Michigan, Ann Arbor, most notably Matt Tomes and Dr. Gaurav Bahl. They were instrumental in helping me learn how to build and operate a fiber taper pulling station on which I spent my first few months fiddling and learning how to handle microspheres and optical components. I benefitted tremendously from the time I spent at the Cornell CNF cleanroom and I am grateful to all the staff members for their help, especially Daron Westly, Meredith Metzler, Rob Ilic, Noah Clay, Sam Wright, Vince Genova and Dan McCollister. Scott Coldren was my go-to guy in times of crises and I can't even imagine how I would have been able to sail through the often rough waters otherwise known as graduate school requirements. Dan Richter and Kim

Stockton did a great job that made purchasing stuff a breeze. Patty Gonyea and Mark Malkin made sure the lab and my experimental setups were never hit by technical snags due to construction work in the department and certainly have ensured I did not have to spend any more years than necessary in Ithaca. I am indeed very thankful to all of them for their immense support.

Were it not for Suresh, Vivek, Amit and Anand, I would probably have spent every waking hour in the lab or cleanroom. The wonderful discussions we had over dinner every night and the times we spent exploring Ithaca added warmth to my stay here. Thank you for making sure I never felt homesick. Tanay has been a wonderful buddy and I will miss him the most when I leave Cornell. Krishna, Shantanu and Mustansir welcomed me into their vibrant social circles in Ithaca and have been pillars of strength to whom I have always turned to in times of frustration and desparation. I am also very grateful to have met such wonderful people as Adarsh, Shreesha, Amit, Abhinandan, Sachin, Poornima, Srinitya, Sushmit, Soumya, Triveni, Sarvani, Ved, Avik, Mihir and Ishita, and for the friendships forged and cherished. Also thanks are due to countless other souls who touched my life while at Cornell - there are too many names to thank each one in person, and I apologize if I missed someone.

In the darkest hours of my life, I always turned to my spiritual master HH Sadyojat Shankarashram Swami and the Shri Chitrapur Math at Shirali, India for guidance, and that has carried me through the biggest obstacles I faced over the course of my Ph.D. My life has been made worth living by the uncondtional love bestowed upon me by all my relatives, friends and well wishers. I was especially very lucky to have Krishnanand Dada, Viju vahini and Ronak living at a convenient driving distance from Cornell - without them maybe I would have chosen another school to begin with. Krishna and Ashima have been wonderful neighbors and the

most priceless of friends and I shall always cherish the times spent with them and hope the future has far more to offer. Kasturi has added newfound meaning to my life by filling it up with lots of love and has played a very important role in helping me earn my degree by always being there to help me vent out my frustrations. I wish Cornell was located in Bombay - I have missed Ma, Pa and Shivu and no amount of joy felt here at Cornell can take away from how I have longed to always be with you. Last but not the least, my utmost thanks to all the wonderful restaurateurs and cafe owners in Ithaca for providing culinary bliss and veggie food options without which life in Ithaca would have been quite dull.

TABLE OF CONTENTS

LIST OF TABLES

LIST OF FIGURES

CHAPTER 1

INTRODUCTION

1.1 Chip-Scale Oscillators and Time-Keeping

Reference oscillators are ubiquitous elements used in almost any electronics system and constitute a multi-billion dollar market in today's electronic industry. These oscillators are used for a wide range of applications varying from keeping track of real time, setting clock frequency for digital data transmission, frequency up- and down-conversion in RF transceivers and clocking of logic circuits. Obviously, the electrical specification of the oscillator depends on the application it is being used for. As a result, a variety of oscillator technologies exist today, each technology suiting a specific need.

For mainstream consumer applications, two technology families are distinguished: mechanical and electrical oscillators. In mechanical oscillators, the frequency selective element is a mechanical resonator made from quartz for high-end applications (e.g. wireless communication, realtime clocks, high-speed digital interfaces) [1], or silicon or other type of bulk piezoelectric material, such as barium titanate or lead-zirconium titanate, for less demanding and cost-sensitive applications (e.g. digital audio, video, household appliances) [2]. In electrical oscillators, the frequency-selective element is integrated on the chip and comprises a resistor-capactior (RC) or a g_mC filter for low-end applications (e.g. clocking of logic) or an inductor-capacitor (LC) filter for more demanding applications (e.g. in frequency synthesizers for wireless communication and digital interfaces).

Although the electrical performance of high quality factor (Q) mechanical os-

cillators cannot be met by electrical oscillators, conventional mechanical oscillators show some important drawbacks that prevent their use in any application [3]. Conventional mechanical resonators are relatively bulky and cannot be integrated on a CMOS die. Thus it is difficult to integrate such resonators into the same package that contains the CMOS die without increasing the manufacturing complexity and cost. Therefore, mechanical resonators have to interface with other circuit components on board level and hence they form a bottleneck for the ultimate miniaturization of micro-electro-mechanical systems (MEMS). In contrast, the use of low-Q electrical oscillators is limited to applications where accuracy and noise specification is relaxed. Their stability and phase noise can be improved by designing arrays of such oscillators to boost the signal-to-noise ratio (SNR), or by locking them to mechanical oscillators using a phase-locked loop (PLL) [4]. However, this again requires a bulky off chip component adding to the total size and cost of the system.

1.2 Micromechanical Oscillators

An emerging class of mechanical oscillators is based on MEMS technology [3, 5, 6]. The extraordinary small size, high level of integration, low cost and high volume manufacturing capability that is possible with MEMS appear to open exceptional possibilities for creating miniature-scale precision oscillators at low cost. MEMS oscillators can be integrated either on the CMOS die or as a separate die combined with a CMOS die in a single package using a standard low cost plastic package. It can be expected that a MEMS-based oscillator has a superior noise performance and frequency stability compared to electrical oscillators, since the MEMS-based oscillator is based on mechanical resonance exhibiting a high Q factor, typically

on the order of tens of thousands at microwave frequencies. At the same time, it is expected that the use of MEMS reduces the size and cost and increases the level of system integration compared to the more conventional mechanical resonators, since the processes and materials being used are often CMOS compatible and use the CMOS manufacturing infrastructure. MEMS oscillators are powerful contenders to fill the gap between high-performance, non-CMOS compatible technologies on the one hand, and low-performance CMOS compatible technologies on the other hand. The replacement of a quartz resonator with a MEMS resonator and integrating the MEMS resonator with the CMOS in a single package or a single die will lead to a reduction in the form factor, board complexity and cost of electronic systems [7]. Simultaneously, a MEMS implementation will have an improved electrical performance compared to LC, RC or other types of oscillators based on electrical rather than mechanical resonance. These unique attributes could also potentially open up new application domains requiring extreme form factor such as wireless sensor nodes [8], SIM and smartcards, and cell phone base stations [9].

1.2.1 Micro-electro mechanical (MEMS) oscillator technology

MEMS-based realizations of timing and frequency control functions, including 0.09% bandwidth filters with less than 0.6-dB insertion loss, GSM-compliant low phase noise oscillators and miniature atomic clocks have been demonstrated, with competing power consumption and performance benefits afforded by scaling to micro dimensions [6, 8]. In particular, via scaling, vibrating RF MEMS devices have now reached frequencies commensurate with critical RF functions in wireless applications and have done so with previously unavailable on-chip quality factors.

MEMS oscillator technology is making its way into commercial markets through several companies (e.g., Discera, IDT, Silicon Labs and SiTime) which are now sampling low-end timekeeper products based on this technology [3]. Meanwhile, on the high-end front, the success of efforts to scale atomic clocks down to 10cm^3 volume package strongly encourages ongoing efforts bent on shrinking them even further, down to 1cm^3 volume, while still posting superior phase noise and power consumption numbers [5]. However, scaling MEMS technologies to higher frequencies in the range of 5-10GHz presents trememdous fundamental and practical challenges. Direct conversion radio architectures require oscillators operating at GHz rate frequencies with good phase noise performance. Oscillators based on electrostatically actuated MEMS resonators have been demonstrated in the few MHz-GHz frequency range [9, 10, 11]. As we describe in detail in section 4.5, at higher frequencies, the motional impedance of electrostatically transduced resonators is very large, and hence it is difficult to operate such a resonator in feedback as an oscillator. Piezoelectric transduction presents lower motional impedances at these frequencies, and piezoelectrically transduced Film Bulk Acoustic wave Resonator (FBAR) [12, 13, 14] and Contour Mode Resonator (CMR) [15, 16] based oscillators operating at few GHz frequencies have been demonstrated. Scaling these piezoelectric oscillators to even higher frequencies necessitates a thinner piezoelectric film, which leads to mass-loading of the resonator due to the metal electrodes atop used to drive motion. This reduces the $k_t^2 - Q$ (electromechanical coupling constant-quality factor product).

1.2.2 Hybrid MEMS oscillators

Recent research efforts in the MEMS community were focused on developing novel transduction schemes with reduced motional impedances at beyond GHz frequencies [17]. Building on initial pioneering work at UC Berkeley and Delft, solid-dielectric transduced thickness shear mode MEMS resonators with 807MHz center frequency, and motional impedance R_x <100Ω and Qs>7,000 [18] were developed. Recently, resonators with center frequency of 3.3GHz and with mechanical quality factor of 2,057 were shown using unreleased deep-trench capacitors [19]. A resonant body transistor, which integrates a sense transistor directly into the resonator body, was also developed with center frequencies at 11.7GHz [20] and 39GHz [21]. Junction field effect transistor (JFET) [22] and PN-diode [23] based sensing schemes also led to realization of silicon resonators with f-Q product values close to the theoretical material limit for Si. However, these resonators cannot be easily integrated into oscillators due to the large parasitics that hinder signal sense at these frequencies.

1.3 Cavity Opto-Mechanics

That light can be used to sense displacements on the order of few nano meters or lesser was well known in the MEMS community, via stroboscopic interferometry [24], homodyne Michelson interferometry [25] and heterodyne laser-Doppler interferometry [26]. In the past few years, the fields of optical microresonators and mechanical resonators have seen a lot of research activity independently for a variety of applications. While electromagnetic radiation pressure force was well understood earlier, the dynamic effect of light exciting a mechanical resonator mode

first demonstrated in ultra high quality factor silica micro toroids [27, 28] brought the two fields together to establish the field of cavity optomechanics. Progress made in this field with applications to displacement sensitivity at multi-GHz frequencies will be explored in subsequent chapters.

1.4 From Opto-Mechanics to Mechano-Optics

The interplay between acoustics and photonics in opto-mechanical systems goes beyond mere motion sensing based applications. Conventional research efforts in opto-mechanics have been directed towards pushing the state of the art in displacement and force sensitivity using light, and mechanical oscillations as well as light induced *cooling* or damping of mechanical motion [28, 29]. The mechanical back-action force, which denotes the force acting on the light due to mechanical motion can be used to realize applications of interest to the photonics community. The focus of this work is primarily directed towards realizing multi GHz mechanical oscillators using photonics, and constitutes part I of this thesis. In addition to this, the technology developed for designing these oscillators was leveraged to develop theoretical and experimental demonstrations of photonics applications using MEMS. This work culminated in the first ever reported acousto-optic frequency modulator and an electro-mechanical photodetector, which are covered in part II of this thesis.

CHAPTER 2

OPTO-MECHANICAL MODULATION

2.1 Opto-Mechanical Resonators

An opto-mechanical resonator is a resonating structure harboring co-existing mechanical and optical degrees of freedom, or 'resonance modes'. The interplay between the mechanical and optical resonances can lead to interesting applications for motion sensing using light. Strong coupling also opens up a path for energy transfer between the optics and the acoustics. One such interaction will be dealt with in significant detail in the next chapter. This chapter presents more understanding into the most commonly exploited feature of opto-mechanical systems, namely displacement sensing using photonics.

2.1.1 Dynamics in opto-mechanical systems

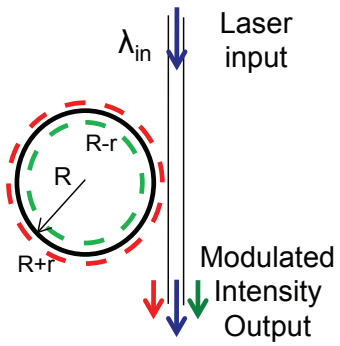

Figure 2.1: Illustration an opto-mechanical resonator interrogated with a waveguide.

Figure 2.1 shows a schematic of an opto-mechanical resonator interrogated with

a waveguide. The illustration shows the resonator vibrating in the fundamental radial expansion "breathing" mode. By carefully designing the waveguide and engineering the resonator-waveguide gap, the evanescent light field in the waveguide can couple to the opto-mechanical resonator, provided the wavelength of light lies in the full-width-at-half-maximum (FWHM) linewidth of the optical resonance of the cavity. The optical resonance wavelength for the resonator λ_{opt}, is specified by the equation $m\lambda_{opt} = 2\pi R n_{eff}$, where R is the radius of the ring resonator, n_{eff} is the effective refractive index for light circulating inside the resonator, and m is an integer. Intuitively, we can interpret the equation as a condition for constructive interference between the photons coupling from the waveguide to the resonator with photons previously coupled that execute a round trip inside the resonator. The RHS in the equation above is the optical path length traversed by the photons in one round-trip. For constructive interference, this path length must be an integer multiple of the wavelength of light. The FWHM linewidth is specified by the total loaded optical quality factor of the optical resonance, Q_{tot}.

The dynamics of the mechanical resonance can be specified by the conventional second order differential equation for a moving mass:

$$\frac{d^2r}{dt^2} + \frac{\Omega_{mech}}{Q_{mech}}\frac{dr}{dt} + \Omega_{mech}^2 r = \frac{F}{m_{eff}} \tag{2.1}$$

where r is the radial displacement of the resonator, Ω_{mech} and Q_{mech} are the mechanical resonance frequency and quality factor, F is the force acting on the mechanical resonator in the radial direction, and m_{eff} is the effective mass of the mechanical mode.

The equation describing the dynamics of the optical resonance can be specified by the following equation [28]:

$$\frac{da}{dt} = -\left(j\Delta + \Gamma_{ext} + \Gamma_{int}\right) a - js\sqrt{2\Gamma_{ext}} \tag{2.2}$$

Here, Γ_{ext} is the decay rate associated with coupling of photons to the optical cavity, and Γ_{int} is the intrinsic cavity photon decay rate. s is the input laser field normalized to power $\left(|s|^2 = P_{laser}\right)$ and Δ is the detuning of the laser frequency from the optical resonance frequency, $\Delta = \omega_{laser} - \omega_{opt}$. The two equations are coupled via the detuning term, since the radial motion amounts to changes in the optical path length, which affects the optical resonance frequency:

$$\omega_{opt} = \omega_{opt,0} + g_{OM} r \tag{2.3}$$

where $\omega_{opt,0}$ is the static optical resonance frequency in absence of motion, and g_{OM} is the opto-mechanical coupling constant, which is described in detail in the next section.

2.1.2 Opto-mechanical coupling constant

Consider the case of the ring resonator discussed above as shown in Figure 2.1. When the ring expands, the motion leads to a change in the circumference of the ring and thereby a change in the optical path length for light circulating around the resonator. Thus a shift in the radius by Δr amounts to a change in the optical resonance wavelength, $\Delta\lambda$:

$$m\left(\lambda_{opt} + \Delta\lambda\right) = 2\pi\left(R + r\right) n_{eff} \tag{2.4}$$

$$\Rightarrow \frac{\Delta\lambda}{\lambda_{opt}} = \frac{r}{R} \tag{2.5}$$

Expressing equation 2.5 in terms of frequency and taking the limit $r \to 0$:

$$\Rightarrow \frac{d\omega}{dr} = -\frac{\omega_{opt}}{R} = g_{OM} \tag{2.6}$$

The expression in equation 2.6 is a measure of the change of the optical resonance frequency in response to changes in the radius of the resonator, and is termed as the opto-mechanical coupling constant g_{OM} [13]. A larger g_{OM} translates to increased displacement sensitivity for an opto-mechanical resonator, thereby efficiently turning mechanical information into optical information and vice versa, and is hence beneficial to most applications in opto-mechanics. Equation 2.6 is valid for a radially symmetric resonator e.g. a ring or a disk resonator, exhibiting a radial mode of vibration. The general problem of how the eigenfrequency of the optical resonance (ω_{opt}) depends on the deformation of the resonator (x) can be solved by a perturbative treatment of Maxwell's equations [30]. A convenient approach is to represent the resonator deformation by the displacement, x, of a chosen point of the resonator having maximum displacement amplitude. If the normalized displacement profile is known, x suffices to represent the complete resonator deformation field. For e.g. the deformation profile for radial and wineglass modes in a disk resonator is completely determined in [31], and can be normalized to the displacement amplitude at the point of maximum motion. With this approach g_{OM} is expressed as the integral over the rigid resonator boundaries [30]:

$$g_{OM} = \frac{\omega_{opt,0}}{4} \int (\mathbf{q}.\mathbf{n}) \left[\Delta\epsilon \left| e_{||} \right|^2 - \Delta \left(\epsilon^{-1} \right) \left| d_{\perp} \right|^2 \right] dA \tag{2.7}$$

Here $\mathbf{q}$ is the normalized displacement profile vector such that $\max|\mathbf{q}(r)|=1$, and $\mathbf{n}$ is the normal unit vector on the boundary. The dielectric constant of the resonator is denoted by ϵ, $\Delta\epsilon = \epsilon - 1$ and $\Delta\left(\epsilon^{-1}\right) = \epsilon^{-1} - 1$, $\mathbf{e}$ is the electric complex field vector normalized such that $\frac{1}{2}\int \epsilon \left|\mathbf{e}\right|^2 dV = 1$, and $\mathbf{d} = \epsilon\mathbf{e}$ [9, good gom]. Equation 2.7 shows that g_{OM} depends both on the optical and mechanical mode of the resonator under consideration.

2.2 Analytical Treatment of Opto-Mechanical Modulation

As discussed in the previous section, an optomechanical cavity has coupled optical and mechanical degrees of freedom. This coupling mechanism is nonlinear [28] and the non-adiabatic response of the intra-cavity optical field to changes in the cavity size can lead to interesting opto-mechanical interactions. The opto-mechanical cavity can be treated as a Fabry-Perot cavity formed by two mirrors, one of which is fixed and the other is suspended with a mechanical spring. If the mechanical resonant mode of the cavity is actuated, the cavity executes oscillatory motion at this frequency which results in Doppler-shift of the circulating intra-cavity optical field, thus modulating its phase. Figure 2.2 shows an illustration of such a scheme. In the frequency domain, this frequency modulation manifests itself as sidebands centered about the input laser frequency line, at a frequency separation that is equal to the frequency of the actuated mechanical resonance. The cavity density of states shapes the resultant sidebands leading to enhancement of only those sidebands that are coupled to the optical cavity, thus causing an asymmetry in the intensity of the lower and higher frequency sidebands. This asymmetry leads to an effective amplitude modulation of the laser light, in addition to frequency modulation. This shall be dealt with in significant detail in chapter 5. For now,

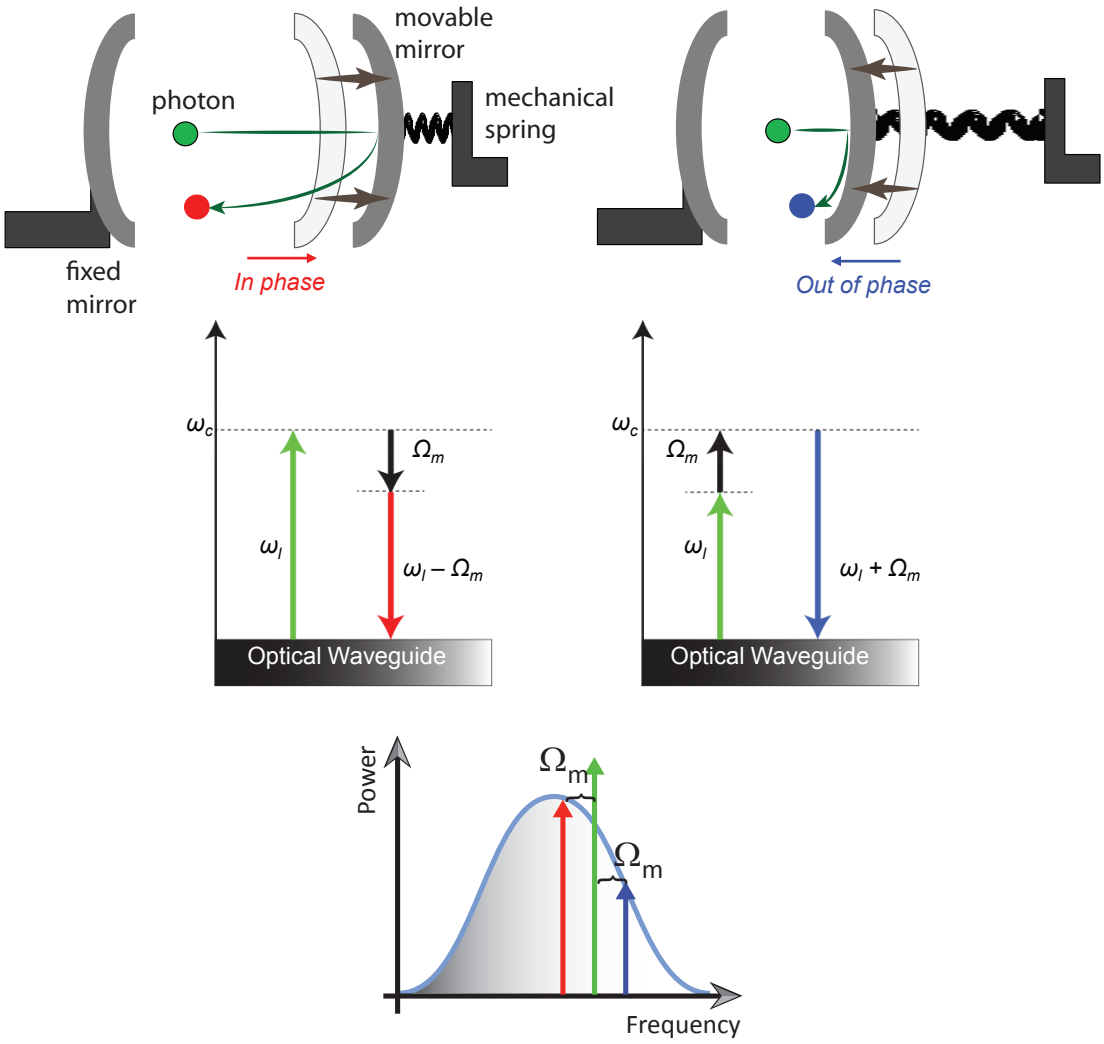

Figure 2.2: Illustration of Doppler shift of photon frequencies inside an opto-mechanical cavity. When a photon strikes the cavity in phase with its motion, the photon frequency is shifted down by the mechanical resonance frequency Ω_m and when the photon and the moving cavity interact out of phase with each other, the photon frequency increases by Ω_m. The cavity density of states shapes the intensities of the resultant sidebands.

it suffices to focus on the effect of motion of the resonator on the circulating light field amplitude.

Assume that the cavity is oscillating such that its radius is sinusoidally displaced as described in equation 2.8:

$$u(t) = U_0 sin(\Omega_{mech} t) \tag{2.8}$$

The intra-cavity field amplitude, $a_p(t)$, can be derived as in [3] by introducing a modulation index, $\beta = \frac{U_0}{R}\frac{\omega_{opt}}{\Omega_{mech}}$, where ω_{opt} is the frequency of the input pump laser [32]:

$$a_p(t) = \frac{s}{\sqrt{\tau_{ex}}} \sum_{n=-\infty}^{+\infty} \frac{(-j)^n J_n(\beta)}{\frac{\kappa}{2} + j\left(\Delta + n\Omega_{mech}\right)} e^{j[(\omega_{opt} + n\Omega_{mech})t + \beta cos(\Omega_{mech} t)]} \tag{2.9}$$

Here, s denotes the input pump laser field amplitude, τ_{ex} is the lifetime due to coupling between the cavity and the waveguide, κ is the full width at half maximum (FWHM) linewidth of the optical cavity resonance, and Δ denotes the detuning of the laser from the optical cavity resonance, specified in angular frequency. J_n is the Bessel function of the first kind. Thus, the modulation index determines the relative weights of the sidebands, whose width is governed by the optical cavity linewidth.

2.3 Displacement Sensitivity and Bandwidth

Periodic motion of the resonator thus leads to periodic modulation of the optical power transmitted at the output of the opto-mechanical system. A motion ampli-

tude of r translates to a shift in the optical resonance frequency by the amount $g_{OM}r$, which leads to a modulated power amplitude:

$$P_{mod} = g_{OM} S(\Delta) r \tag{2.10}$$

where $S(\Delta)$ is the slope of the optical power transmission spectrum at detuning Δ.

The analysis presented in the sections above, wherein we assume $g_{OM} = -\frac{\omega_{opt}}{R}$, is only valid in the case where light responds instantaneously to any changes in the resonator geometry on account of motion. In reality, the photons coupling to the resonator from the waveguide have a finite lifetime associated with the coupling. Also the photons have finite intrinsic and loaded decay rates in the optical resonator. The total cavity lifetime $\tau_{opt} = \frac{2Q_{tot}}{\omega_{opt}}$ is a measure of the time taken by the optical system to respond to changes in the mechanical system. For an optical resonator with loaded optical quality factor Q_{tot} = 100,000 at a wavelength of 1,550nm, the cavity lifetime is 0.52ns, which corresponds to a response bandwidth of 1/0.5ns = 1.9GHz. Thus an opto-mechanical resonator with these parameters will exhibit a response captured by the equations derived in this section for mechanical resonance frequencies $\ll$1.9GHz. At frequencies above 1.9GHz, the mechanical system dynamics occur at faster rates than the rate at which the optical system responds, thereby leading to incomplete modulation. Mani et al. capture this low-pass frequency response of the opto-mechanical system in the parameter Γ [33]:

$$P_{mod} = \Gamma g_{OM} S(\Delta) r \tag{2.11}$$

However, this parameter is not easily characterized, both analytically and experimentally [33, 34]. These high frequency mechanical modes are said to lie in the *resolved sideband regime*, since the modulation sidebands generated around the laser line lie outside the optical cavity linewidth, which also intuitively explains the incomplete modulation.

2.4 Modulation Non-Linearity

The optical resonance lineshape is a Lorentzian, with the optical transmission specified by the following equation:

$$T(\omega) = \left|\frac{s_{output}}{s}\right|^2 = \frac{4\left(\omega - \omega_{opt}\right)^2 + \omega_{opt}^2\left(\frac{1}{Q_{int}} - \frac{1}{Q_{ext}}\right)^2}{4\left(\omega - \omega_{opt}\right)^2 + \omega_{opt}^2\left(\frac{1}{Q_{int}} + \frac{1}{Q_{ext}}\right)^2} \tag{2.12}$$

The modulation of this lineshape due to motion of the cavity is inherently nonlinear. This is also evident from equation 2.9, which shows multiple sidebands spaced from the laser line by frequencies $n\Omega_{mech}$ $(n = 1, 2, 3, ...)$.

With the basics of opto-mechanical modulation thus established, we shall now look at two oscillator technologies centered around this basic principle, namely the opto-mechanical oscillator and the opto-acoustic oscillator in the next two topics. In part II, we shall view opto-mechanics in a different light, where light does not merely sense motion, and we explore a reversal of roles between the optics and mechanics in the context of two applications - acousto-optic frequency modulation and electromechanical photodetection.

Part I

Photonics Aided MEMS Applications

CHAPTER 3

OPTO-MECHANICAL OSCILLATOR

3.1 Overview of Opto-Mechanical Oscillators

Light can excite oscillations in mechanical resonators in several ways [29] - radiation pressure (RP) driven [28, 33], via the optical gradient force [35, 36] or through electrostriction [37, 38, 39] and other nonlinear opto-mechanical interactions [40]. RP driven oscillations have been extensively studied [28] and such oscillations have been observed by various teams [33, 41, 42]. All these demonstrations employ either a prism coupler [40] or a tapered fiber [28, 33, 41] to couple light into the microresonator, and are not integrated solutions. Chip-scale opto-mechanical resonators in silicon nitride with integrated waveguides have been shown [43], however these devices employ inverse fiber taper coupling and no self-oscillations have been reported. Some solutions also require a CO_2 laser reflow step [33] to microfabricate the resonator, which is a serial process step and is thus undesirable for a high-yield solution. The phase noise numbers reported for RP driven oscillations [33] are far worse than those reported for CMOS oscillators in similar frequency ranges. The phase noise also shows higher order slopes at close to carrier frequencies, that are unexplained but are often attributed to environmental noise. Theoretical analysis for opto-mechanical oscillators (OMOs) [33, 34] indicates that these problems can be overcome by having a high optical quality factor, a moderately high mechanical quality factor, large power handling capacity, and a robust device that is immune to environmental disturbances. As such, there is a need for a truly integrated, monolithic device that can deliver all of these requirements and be compatible with existing chip-scale laser technology to enable a truly chip-scale

opto-mechanical oscillator. This chapter presents an integrated OMO fabricated in silicon nitride that satisfies all of these requirements. The next section presents an analytical understanding of the radiation pressure force. We then look at the design and fabrication process flow for the opto-mechanical resonator. The later sections provide details on experimental characterization and a phase noise model for the OMO.

3.2 Analytical Treatment of Radiation Pressure Driven Oscillations

Consider a ring resonator coupled to an optical waveguide as shown in Figure 3.1. The laser wavelength is blue detuned from the cavity optical resonance wavelength. To understand how this interacts with the mechanical motion of the ring, we can treat the optical resonator as analogous to an optical cavity formed by two mirrors, one fixed and one moving. Some photons from the laser couple into the resonator and start circulating around the periphery of the resonator. The circulating photons exert a force on the boundaries of the ring resonator, known as the radiation pressure force. This force is linearly dependent on the circulating optical power. Larger the power inside the cavity, greater the force exerted.

Now suppose the ring expands. The optical resonance wavelength now increases, being proportional to the radius of the ring. If the laser wavelength is lower than the optical resonance wavelength, the circulating photons now leak out of the resonator back into the waveguide. Thus the radiation pressure force pushing the ring radially outwards reduces. This is equivalent to a spring effect, caused by the optical force, that pulls the ring inwards. As the ring contracts due to the me-

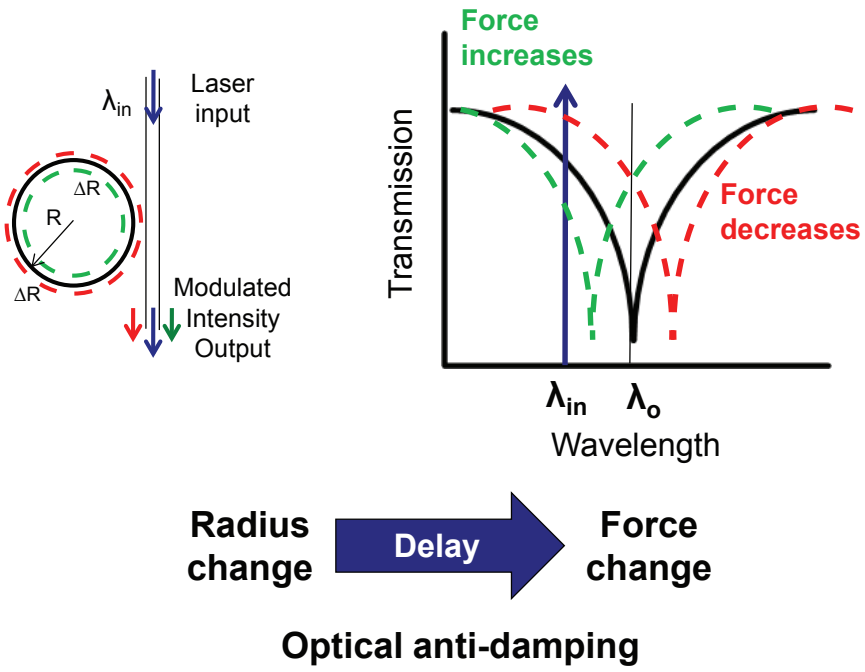

Figure 3.1: Intuitive picture of origin of radiation pressure induced oscillations. The adiabatic response of the mechanical cavity to the optical force results in an optical anti-damping force, proportional to the optical power circulating inside the cavity. Self sustained oscillations occur when the optical power exceeds the threshold required to generate an anti-damping force stronger than the intrinsic mechanical damping.

chanical restoring force, the optical resonance wavelength decreases. This causes more photons to couple into the cavity. The coupling and leakage of photons into and out of the cavity is not an instantaneous process. When the ring expands, the radiation pressure force does not reduce instantaneously, and the lingering photons exert an additional force on the resonator. The delay associated with this adiabatic behavior gives rise to anti-damping of the mechanical motion, shown here as negative damping. If the negative damping associated with the optomechanical interactions are strong enough to over come the intrinsic mechanical damping of the resonator, the circulating optical field sets off self sustained oscillations of the mechanical mode, which is sensed as intensity modulation at the output optical probe.

3.2.1 Mathematical formulation

As intuitively discussed above, the delineation of the response of variation in optical power to changes in the resonator motion into adiabatic and non-adiabatic contributions leads to two manifestations of the opto-mechanical *back action*. The adiabatic component for the back-action force, that is in phase with the displacement, leads to an *optical spring effect* that shifts the mechanical resonance frequency by [28]:

$$\Delta\Omega_{mech} = F^2 \frac{\Gamma_{ext}\Gamma_{tot}}{4\Delta^2 + \Gamma_{tot}^2} \frac{8n_{eff}^2\omega_{opt}}{\Omega_{mech} m_{eff} c^2} \left[\frac{2\Delta\Gamma_{tot}}{4\Delta^2 + \Gamma_{tot}^2}\right] P_{laser} \tag{3.1}$$

Here Γ_{tot} is the loaded cavity photon decay rate, c is the speed of light and $F = \frac{2\pi}{T_{rt}\Gamma_{tot}}$ is the cavity finesse, where T_{rt} is the photon round trip time in the optical cavity.

The non-adiabatic component of the force gives rise to an optical anti-damping rate given by [28]:

$$\Gamma_{ad} = -F^3 \frac{\Gamma_{ext}\Gamma_{tot}}{4\Delta^2 + \Gamma_{tot}^2} \frac{8n_{eff}^3 \omega_{opt} R}{m_{eff} c^3} \left[\frac{16\Delta\Gamma_{tot}^3}{\left(4\Delta^2 + \Gamma_{tot}^2\right)^2} \right] P_{laser} \tag{3.2}$$

This radiation pressure induced anti-damping rate modifies the intrinsic mechanical damping rate $\Gamma_{mech} = \frac{\Omega_{mech}}{Q_{mech}}$, yielding an effective damping rate $\Gamma_{eff} = \Gamma_{ad} + \Gamma_{mech}$. The negative sign in equation 3.2 for positive valued detuning (blue detuning) leads to a reduced damping rate. When the laser power is sufficiently large, the effective damping rate is negative, which implies self-sustained mechanical oscillations in the system.

3.3 A Silicon Nitride Opto-Mechanical Oscillator

3.3.1 Opto-mechanical resonator design

We choose Si_3N_4 as the material to micro-fabricate the opto-mechanical resonator, as it has been shown to demonstrate high optical [44] and high mechanical [45] quality factors. We chose a ring geometry for our resonator owing to its simplicity and the high optical Q it offers [44]. To design for high optical quality factors, we select a wide ring (6μm) with a large radius (40μm) and narrow spokes (0.5μm). This ensures that the Si_3N_4 ring resonator has a high optical Q as the optical mode is confined inside the ring and experiences low bending loss and scattering loss from the spokes.

3.3.2 Optical mode matching

To achieve significant coupling from the light inside the waveguide to the optical resonator, it is imperative to ensure a large spatial overlap and matching of the effective refractive index of the waveguide mode and the optical mode in the resonator. The waveguide-resonator gap is designed to be smaller than 100nm to ensure spatial overlap. Finite element method (FEM) simulations of the optical mode [46] in the resonator indicate an effective refractive index of 1.32. To achieve this index in a silicon nitride waveguide of thickness 300nm, we need a width of 800nm, as obtained from FEM simulations. Figure 3.2 shows screen-shots of the cross sections for the resonator and waveguide simulated using COMSOL FEM.

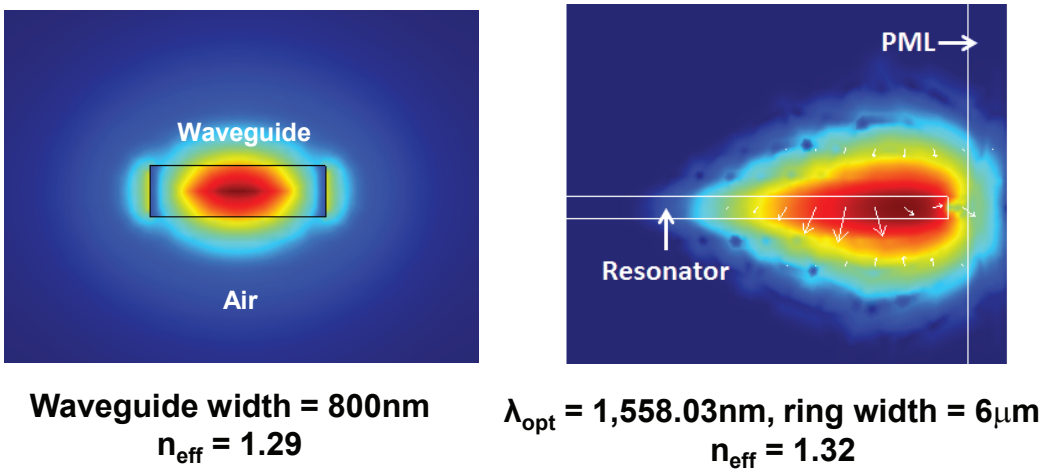

Figure 3.2: FEM simulations of cross sectional profiles of the waveguide and resonator to match the effective refractive indices.

3.3.3 Grating coupler design

Misalignment and mismatch of optical modes between two devices introduces significant coupling losses. As we scale down device sizes to the micro- and nanometer regime, the coupling problems are greatly exaggerated by the small dimensions, which makes alignment a critical and challenging task. It is very common to employ prism couplers and tapered fiber coupling to couple light to opto-mechanical resonators. Due to the lack of integration, these coupling media can introduce environmental noise into the system. Integrated coupling methods to on-chip waveguides using inverse taper couplers [43] and graded refractive index (GRIN) couplers [47] introduce very low coupling losses (<1dB), but require precision alignment of an optical fiber to the on-chip waveguide in case of inverse taper couplers, or complex fabrication processes to obtain a thin film stack in case of GRIN couplers. Grating couplers allow one to couple from a standard single-mode fiber (SSMF) to a high-index-contrast waveguide with high efficiency without the need for lenses. The grating coupler does away with the need for edge facets, allowing for easier on-wafer testing and simplifying processing [48].

Despite these advantages, reported grating couplers exhibit relatively narrow bandwidth, require partial etch and/or high resolution lithography, exhibit significant temperature dependence, and can exhibit significant back reflections in the bandwidth of interest. These disadvantages arise mainly because the grating couplers butt-coupled to SSMF that have been demonstrated so far have been in semiconductor material, such as Si and InP, with very high refractive indices. Because of the high index of semiconductors, the grating holes either must be only partially etched into the waveguide or must be significantly smaller than a wavelength if they are to be fully etched [49], otherwise the grating strength is too

strong. For Si_3N_4, etching grooves with a half-period width completely through a 300-nm waveguide gives an appropriate grating strength, as we see in subsequent paragraphs. This full etching simplifies the processing. The temperature dependence of semiconductors such as Si and InP is 0.1 nm/°C. If the grating coupler is used as an optical filter, this shift can cause problems when the PIC is not temperature controlled. The temperature dependence of Si_3N_4 is ≈0.02nm/°C [50], and thus its wavelength shift is ≈5 times lesser.

The bandwidth of semiconductor grating couplers is narrow because of the high refractive index of semiconductors. We can make an approximate calculation of the bandwidth of a grating coupler as follows: The phase matching condition for the grating is:

$$-\frac{n_0}{\lambda} sin\theta + \frac{n_{wg}}{\lambda} = \frac{1}{\Lambda} \tag{3.3}$$

where n_0 is the refractive index of the cladding/substrate material, n_{wg} is the effective refractive index of light inside the waveguide, λ is the free-space wavelength of light to be guided, Λ is the grating period, and θ is the fiber angle i.e. the angle to vertical at which light is incident on the grating coupler. By choosing appropriate values for the angle, the grating period can be estimated for a given wavelength of light and waveguide mode of interest in a given material medium.

To simulate the grating couplers, we set up a finite difference time domain (FDTD) simulation in Lumerical FDTD Solutions software. Figure 3.3 shows the simulation setup and Figure 3.4 shows the simulated insertion loss of the grating coupler. The simulated 3-dB bandwidth of the coupler exceeds 80nm.

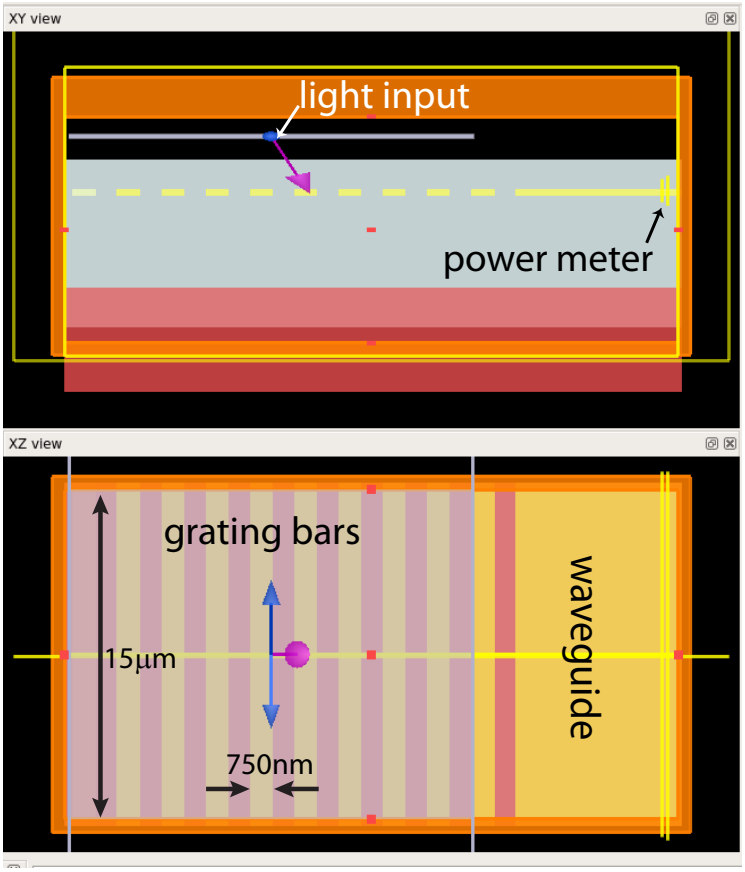

Figure 3.3: 3D FDTD simulation setup of the grating bars. A plane wave light source is used to provide the input light field incident at an angle of 20° to the vertical on to the grating bars. A power meter at the waveguide is used to simulate the optical insertion loss due to the grating coupler.

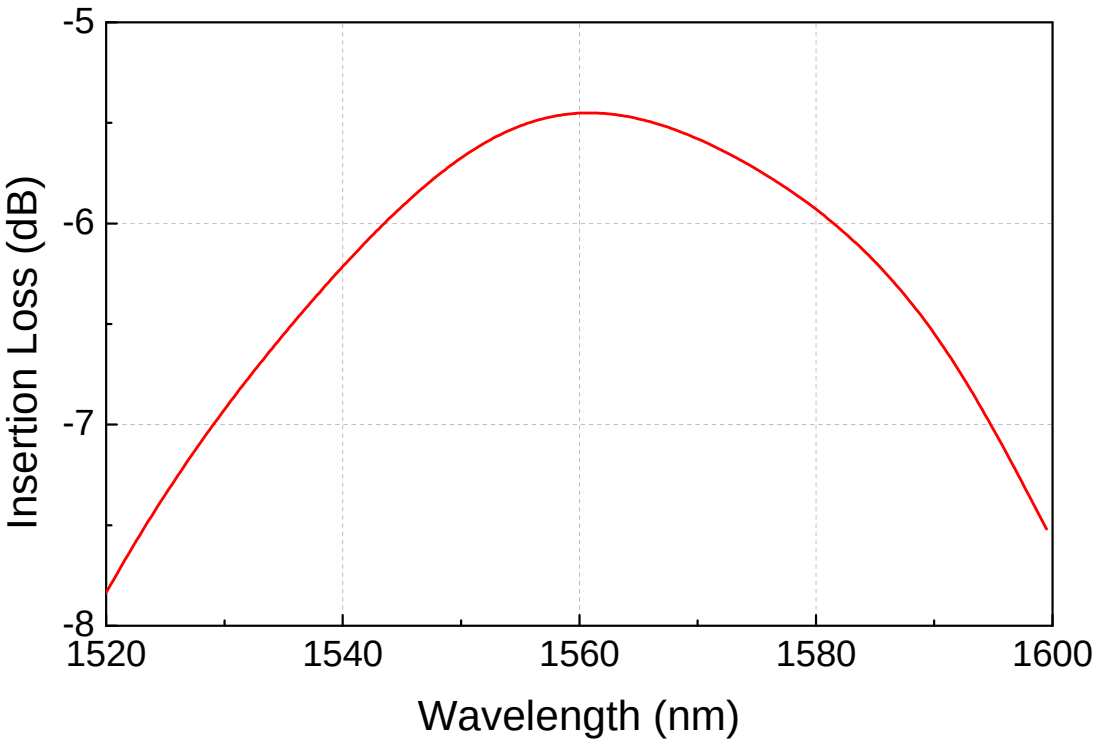

Figure 3.4: FDTD simulated value of the optical insertion loss for the silicon nitride gratings.

3.3.4 Fabrication

We start with silicon wafers that have 4μm SiO_2 thermally grown and deposit 300nm Si_3N_4 using low pressure chemical vapor deposition (LPCVD). To define the resonators, waveguides and grating couplers, ma-N 2403 electron beam resist is spun on top of the nitride and patterned using electron beam lithography. After developing the resist in AZ 726MIF, we etch the pattern into the nitride device layer using CHF_3/O_2 reactive ion etch (RIE). Then we strip the resist and deposit SiO_2 cladding using plasma enhanced chemical vapor deposition (PECVD) to clad the gratings and waveguide with oxide. This is done to reduce losses at the grating couplers. A second mask is then used to pattern release windows near the resonator using contact photolithography. This is followed by a partial etch into the cladding using CHF_3/O_2 RIE. This ensures that we can get away with a relatively shorter release time and thereby not have a large undercut for the waveguides. We then perform a timed release etch in buffered oxide etchant to undercut the devices, to enable opto-mechanics. The samples are then dried using a critical point dryer to prevent stiction. Figure 3.5 illustrates this process flow schematically.

The resulting devices have cladding over the gratings, and the tapered section of the waveguide. The resonator is completely released except for a pedestal in the middle that holds the structure in place. The waveguide is released in the region around the resonator. Figures 3.6 and 3.7 show an optical micrograph and SEM of the device respectively.

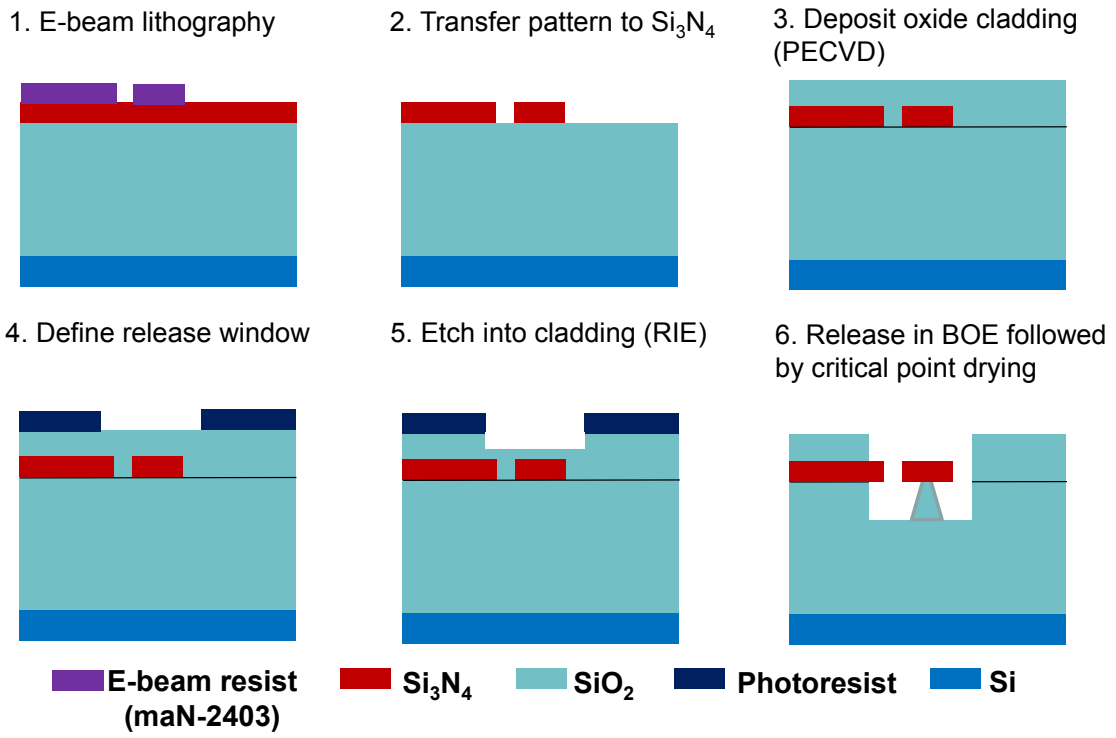

Figure 3.5: Illustration of the process flow to microfabricate grating couplers, waveguides, and opto-mechanical resonators in silicon nitride

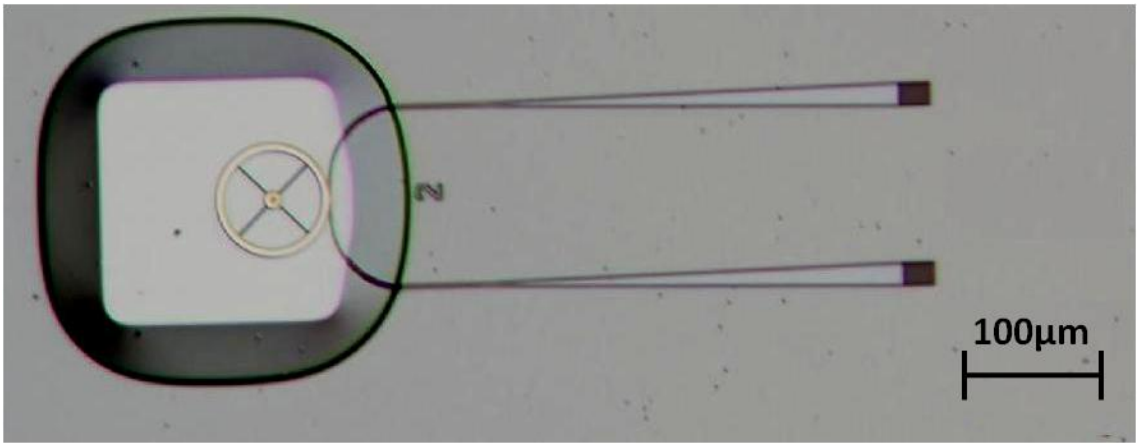

Figure 3.6: Optical micrograph of the integrated device showing the ring resonator, tapered waveguide and grating couplers

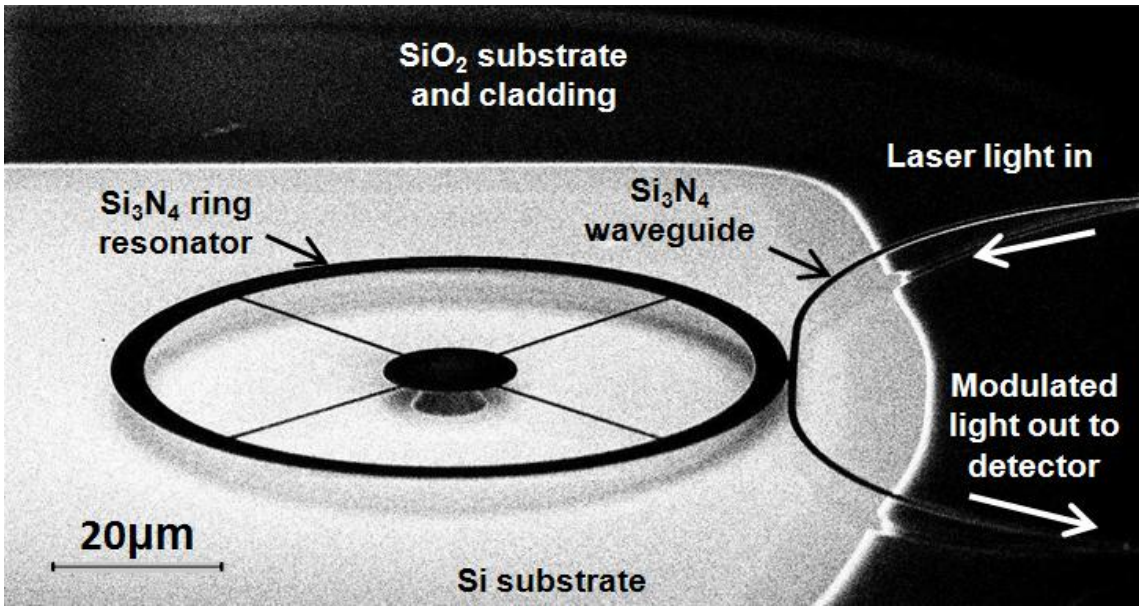

Figure 3.7: Scanning electron micrograph (SEM) of the ring resonator and released section of the waveguide

3.4 Experimental Characterization

3.4.1 Optical characterization

We use a tunable diode laser and a power meter to study the optical transmission spectrum for the silicon nitride opto-mechanical resonator. Light from a tunable diode laser (Santec TSL 510) is coupled into a polarization maintaining (PM) fiber. This is then incident on a glass fiber holder in which the PM fiber is held in a glass plate using V-grooves. The glass plate is polished at an angle of 20° at the face. This glass plate is then held vertically at an angle of 20° over the substrate containing the waveguides. The polish ensures that the face of the glass plate containing the polish fiber end is now flush in line with the substrate. The PM fibers are aligned such that the light coming out is polarized parallel to the

substrate, using manual polarization controllers. The input grating coupler couples this light into the waveguide. At the output grating coupler, the light is coupled into another fiber in the glass plate. The pitch between the two fibers is 127μm. The output from the fiber is sent to an optical power meter.

To obtain an optical transmission spectrum, we use an automated testbench developed using National Instruments (NI) NI Labview software running on a host computer. The output from the power meter is obtained in the form of analog voltage which is transmitted to a controlling computer using an NI digital acquisition card (DAC). The software controls the laser via a GPIB interface. The laser wavelength is swept via software, while the power meter output is collected at the computer. A trigger signal from the laser to the optical power meter ensures that the data from the power meter is recorded with the appropriate wavelength stamp.

Typical optical transmission spectra for the grating couplers are shown in Figure 3.8. The gratings were designed for a pitch of 1.5μm with 50% duty-cycling. The lowest insertion loss (-5.5dB per coupler) is observed for a grating pitch of 1.475μm. Figure 3.9 (a) shows optical transmission spectrum for an unreleased silicon nitride opto-mechanical resonator. The silica cladding results in very high intrinsic quality factors in excess of 1 million, as seen in Figure 3.9 (b). The waveguide-resonator gap for critical coupling to unreleased resonators is experimentally determined to be 1μm.

Releasing the resonator using BOE results in lowering of the optical quality factor, as the light field is now more tightly confined inside the silicon nitride device and is more prone to scattering losses at the air-silicon nitride interface. The mismatch in refractive index for light inside the waveguide at the point where the

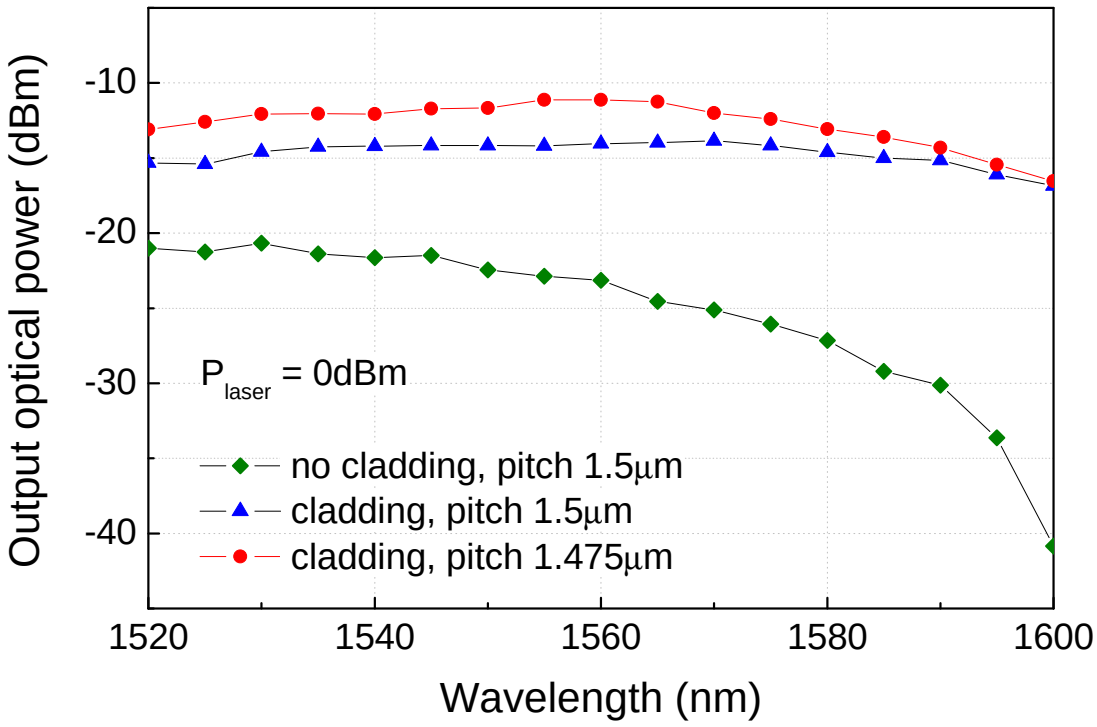

Figure 3.8: Transmission spectra for the grating couplers. Lowest insertion loss (-5.5dB per coupler) is recorded for a grating pitch of 1.475μm with 1μm SiO_2 cladding.

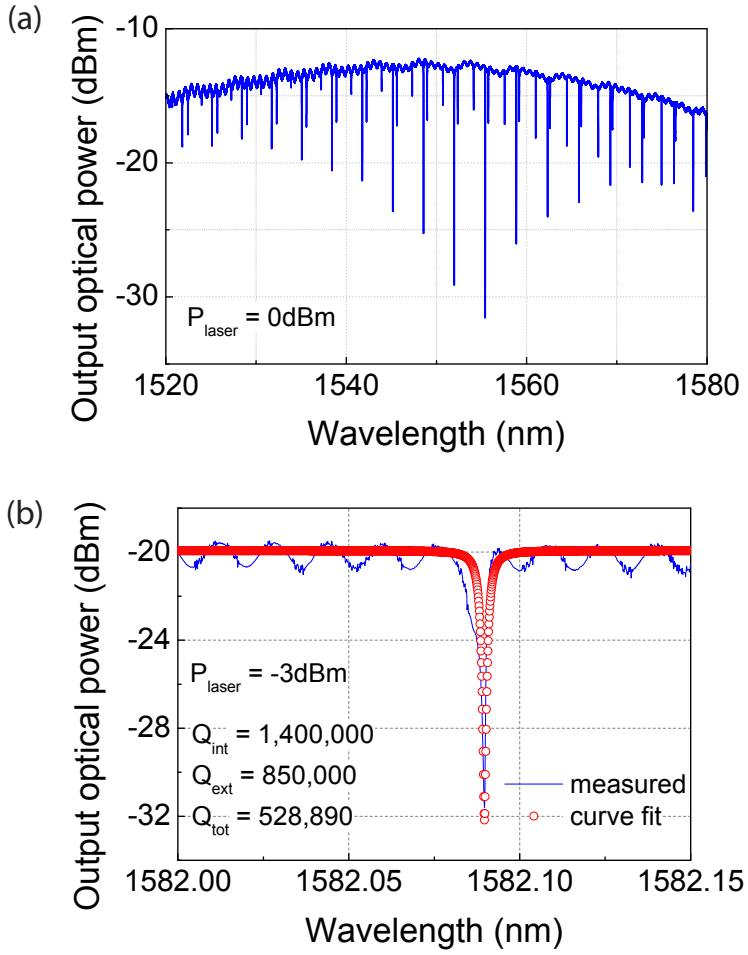

Figure 3.9: (a) Typical transmission spectrum for an unreleased silicon nitride resonator showing coupling to multiple optical modes. (b) A high Q resonance in a silicon nitride resonator with intrinsic quality factor in excess of 1 million.

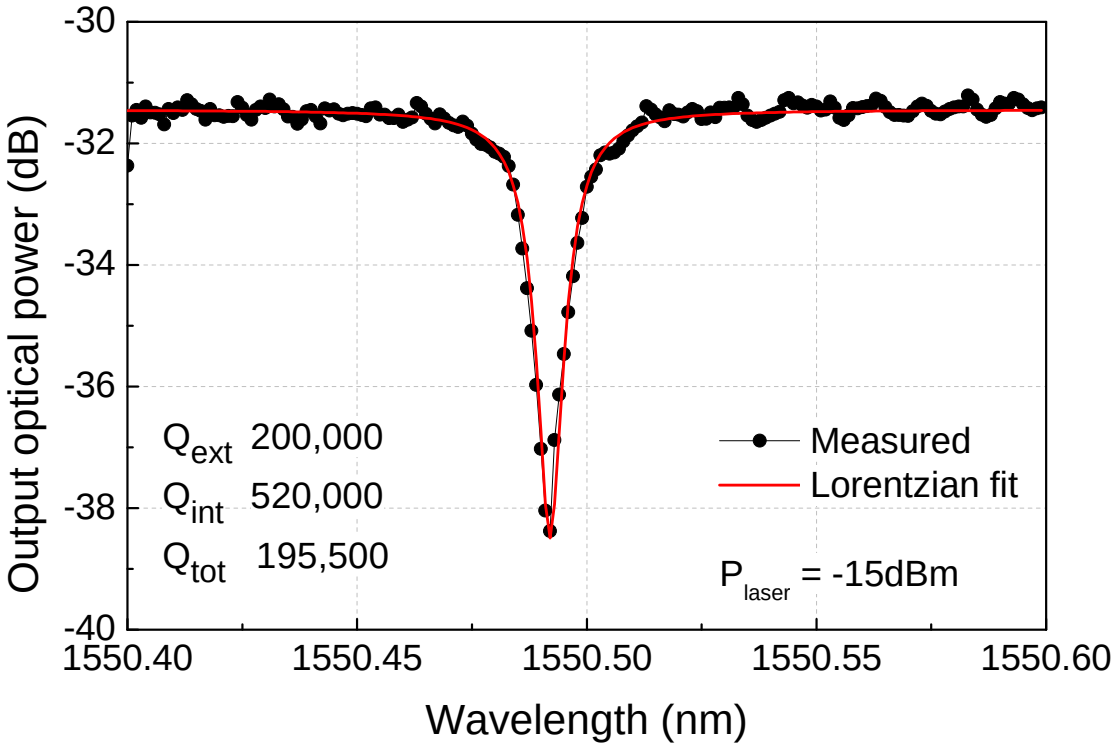

Figure 3.10: Insertion loss measured for -15dBm laser input power for a high loaded Q (≈200,000) optical resonance

waveguide cladding material transitions from silica to air also results in additional coupling losses. The optical loss at each facet is 8dB post release. Typical quality factors for released silicon nitride resonators are ≈100,000, which is significantly lower than the quality factors for unreleased resonators. Figure 3.10 shows a high Q optical resonance in a released resonator with a loaded optical quality factor of ≈200,000. The waveguide-resonator gap for released silicon nitride resonators is 100nm.

3.4.2 Optical metrology of mechanical modes

Once we identify a high Q optical resonance, we setup an experiment to measure the mechanical response of this resonator, as illustrated in figure 4. We use a New Focus 1647 avalanche photodiode (APD) as the photodetector. The gain of the APD is 6,000V/W. The laser wavelength is blue detuned with respect to an optical resonance with optical Q of 200,000. Brownian motion of the opto-mechanical resonator results in modulation of the light at the output fiber. The APD converts this modulation into an RF signal at the modulation frequency, which corresponds to the mechanical resonance frequencies of the device. Various mechanical modes are observed in the RF spectrum recorded on an Agilent E4445A spectrum analyzer.

The largest signal power is recorded for the radial expansion mode of the ring at 41MHz, which corresponds to larger optical path length change in comparison to a wineglass mode of the ring at 28MHz and azimuthal radial modes at 77 MHz and 79 MHz, shown in Figure 3.11. The mechanical Q for the radial expansion mode measured in air is 2,000.

3.4.3 Threshold of radiation pressure oscillations

The optical power threshold for onset of oscillations can be calculated by equating the anti-damping rate in equation 3.2 to the mechanical damping rate to obtain the following expression:

$$P_{thresh} = \frac{4\Delta^2 + \Gamma_{tot}^2}{\Gamma_{ext}\Gamma_{tot}} \frac{\Omega_{mech} m_{eff} c^3}{8 n_{eff}^3 \omega_{opt} R F^3 Q_{mech}} \left[\frac{\left(4\Delta^2 + \Gamma_{tot}^2\right)^2}{16\Delta\Gamma_{tot}^3} \right] \tag{3.4}$$

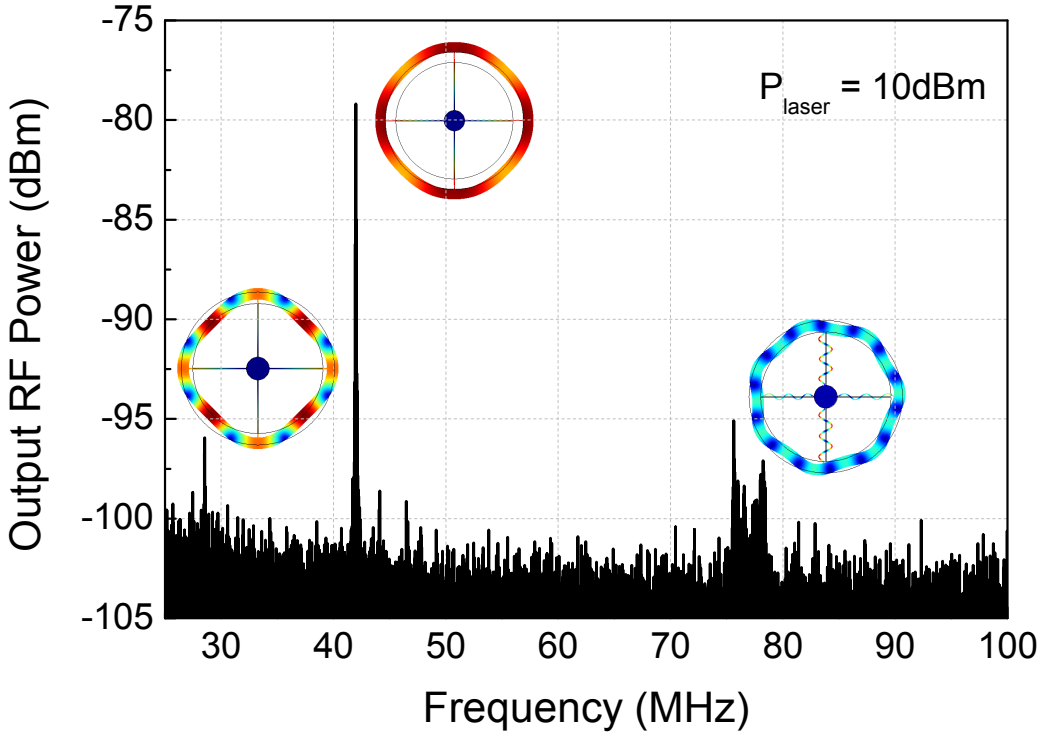

Figure 3.11: RF spectrum at the output of the avalanche photodetector. The peaks observed correspond to the Brownian noise mechanical motion of the micro-ring. The fundamental radial expansion mode of the micro-ring at a frequency of 41.97MHz causes strong intensity modulation of the laser light as compared to a a wineglass mode at 28MHz or a group of azimuthal composite mechanical modes around 77MHz. Insets: FEM simulated modeshapes of the corresponding mechanical modes.

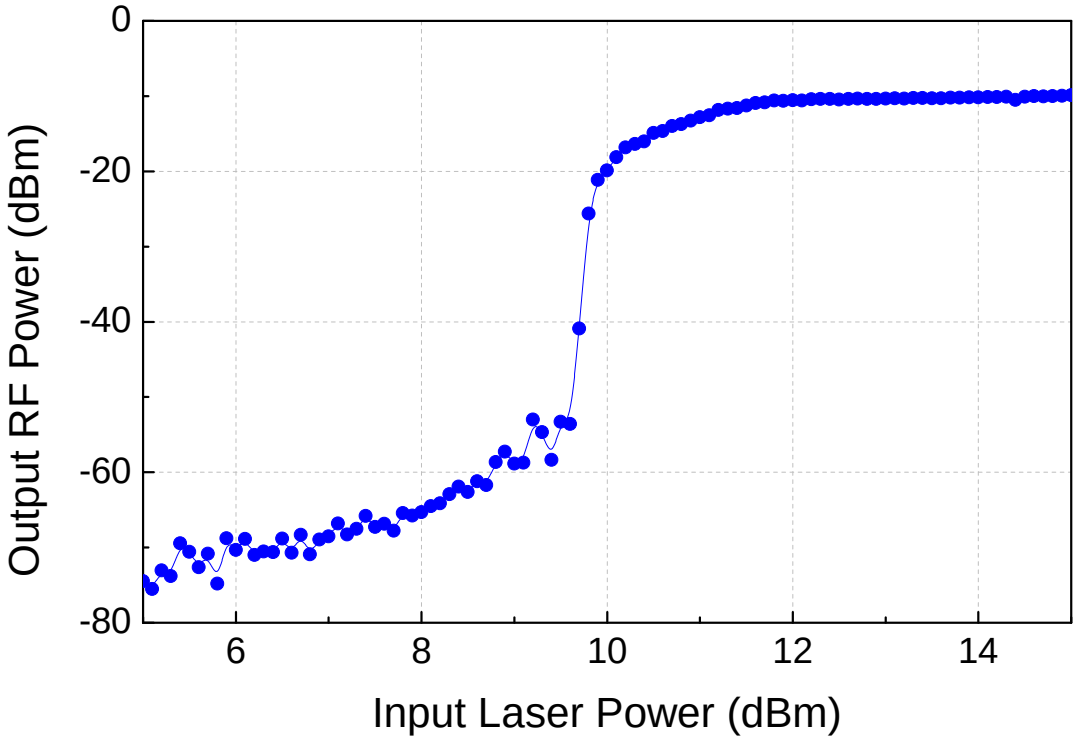

Figure 3.12: Variation of RF power at the output of the photodetector with the input laser power, for the fundamental radial expansion mode of the micro-ring at 41.97MHz. As the laser power is increased, self-sustained oscillations are observed for this mode. The sharp threshold behavior shown is characteristic of radiation pressure induced parametric instability.

Figure 3.12 shows the variation of RF output power at the photodetector with the input laser power. At low input laser powers, the input light coupled into the cavity is modulated by the Brownian noise motion of the fundamental radial expansion mode of the ring. As we increase the laser power, self-sustained oscillations are observed above the input threshold power. The sharp threshold behavior is characteristic of radiation pressure induced parametric instability. Figure 3.13 shows the RF output spectrum measured below and above the optical power threshold for onset of oscillations.

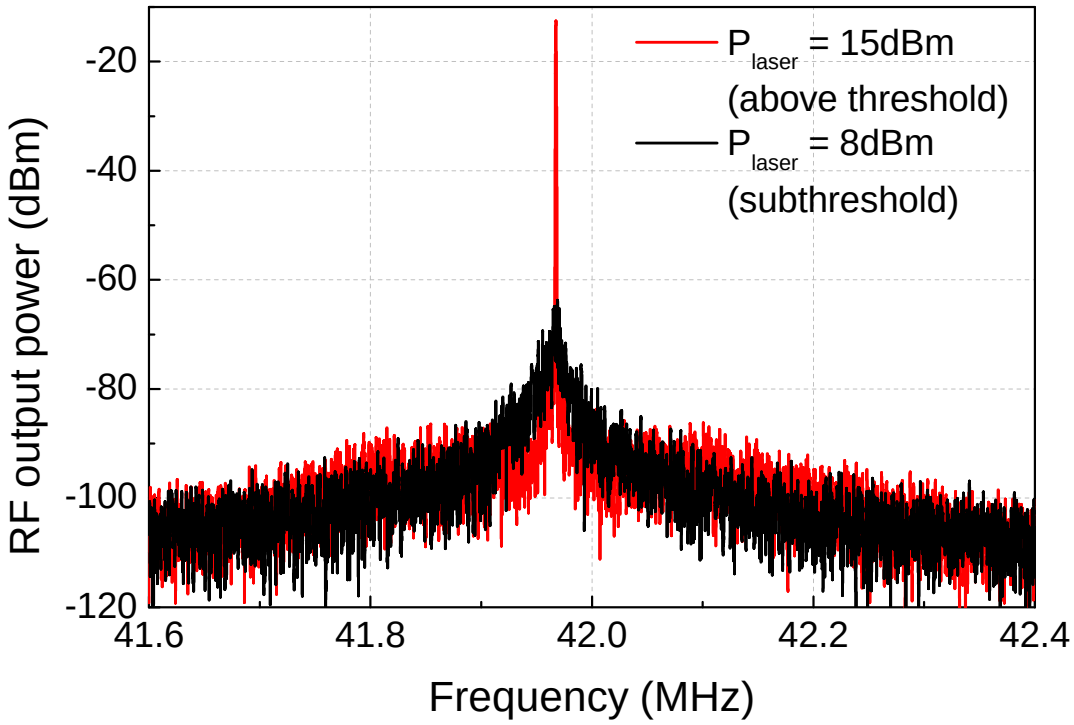

Figure 3.13: Variation of RF power at the output of the photodetector with the input laser power, for the fundamental radial expansion mode of the micro-ring at 41.97MHz. As the laser power is increased, self-sustained oscillations are observed for this mode. The sharp threshold behavior shown is characteristic of radiation pressure induced parametric instability.

3.4.4 Oscillation phase noise

Figure 3.14 shows the phase noise measured for the oscillation at 41MHz. The phase noise at 1kHz offset for the 41MHz OMO is -85dBc/Hz. This is better than the phase noise reported for radiation pressure driven self-oscillations of a microtoroid [33]. The phase noise varies as $1/f^2$ below 100kHz offsets as indicated by the dotted red trend-line implying that the OMO has no flicker noise. The corner frequency for $1/f^2$ region is around 20kHz which agrees with the measured mechanical Q of 2,000 at 41.947MHz. The phase noise is measured with an Agilent E5052B signal source analyzer.

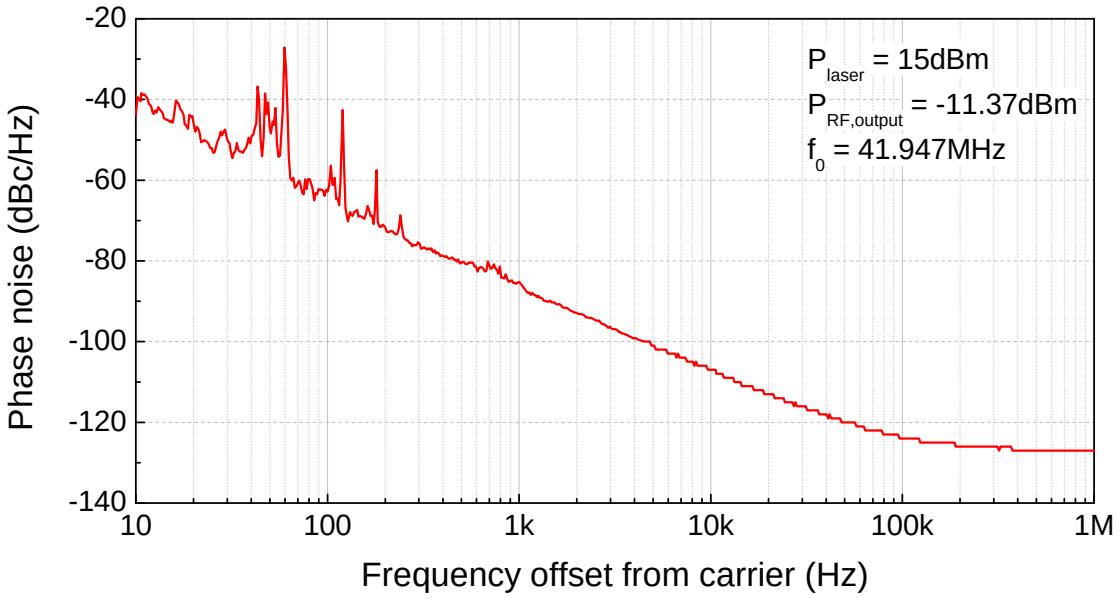

Figure 3.14: Phase noise for OMO operating at 41.947MHz with -11.37dBm output power. The laser input power is +15dBm. It varies as $1/f^2$ below an offset frequency of 100kHz as indicated by the dotted red trend-line, implying that the OMO has no flicker noise. The phase noise is measured with an Agilent E5052B signal source analyzer.

3.5 Phase Noise Modeling of Opto-Mechanical Oscillators

The classical Leeson model for electronic oscillators [51] relates the phase noise of an oscillator to its linewidth. We extend this well established theory to the case of opto-mechanical oscillators.

3.5.1 Oscillation linewidth

Mani et al. have characterized the mechanical oscillation linewidth as follows [33]:

$$\Delta\Omega = \frac{1}{2\pi}\left(\frac{4k_BTQ_{tot}^2}{m_{eff}\Omega_0^2R_0^2}\right)\left(\frac{\Gamma^2\Delta\Omega_0}{M^2}\right) \tag{3.5}$$

The linewidth is set by k_B (Boltzmann constant), T (absolute temperature), Q_{tot} (total optical Q), m_{eff} (effective resonator mass), Ω_0 (mechanical resonant frequency), R_0 (disc radius), Γ (optical modulation transfer function) [33], $\Delta\Omega_0$ (intrinsic mechanical oscillation linewidth) and M (modulation depth). Γ represents the finite response time taken by the resonator to respond to modulation of the optical path length. Intuitively, we can guess that Γ is a low pass filter function of oscillation frequency i.e. at higher mechanical oscillation frequencies its value is smaller. Γ and M are experimental parameters. However, for reasons we discuss later, we will write the expression for the linewidth in terms of more fundamental parameters describing the system:

$$\Delta\Omega = \frac{1}{2\pi}\left(\frac{4k_BT}{m_{eff}\Omega_0^2}\right)\left(\frac{\Delta\Omega_0}{r^2}\right) \tag{3.6}$$

where r is the amplitude of radial displacement.

3.5.2 Phase noise in opto-mechanical oscillators

Phase noise is frequency domain representation of random fluctuations in the phase of a waveform. An ideal oscillator generates a pure sine wave that can be represented as a pair of delta functions at the oscillation frequency in the frequency domain. This just highlights the fact that for an ideal oscillator, all the signal power is at a single frequency. However, due to presence of various noise sources within the oscillation loop, real oscillators demonstrate time domain instabilities i.e. the zero crossings of the waveform are not spaced perfectly at half the period of the waveform from each other, but exhibit random fluctuations.

Thus, the oscillator's energy is not located at a single frequency and it spreads to adjacent frequencies which can be characterized by the linewidth of the oscillator. Most oscillators have a Lorentzian spectral density distribution characterized by the following equation

$$S_v(f_0 + \Delta f) = \frac{A^2}{2\pi} \frac{f_\Delta}{f_\Delta^2 + (\Delta f)^2} \tag{3.7}$$

where $A^2/2$ is the signal power at the oscillation frequency and f_Δ is the linewidth. Δf specifies the offset from oscillation frequency f_0. This spread is typically characterized in terms of phase noise which is specified in dBc/Hz (decibels below carrier per hertz). This way of quantifying phase noise gives a measure of the spread of oscillation power to frequencies offset from the center (carrier) frequency.

Phase noise is one of the most important characteristics of a self-sustained oscillator. For applications such as a frequency reference in communication systems, the phase noise of the oscillator impacts the bit error rate and security. Also, oscillators do not have memory of phase of the waveform and as such are unable

to restore phase, which leads to accumulation of phase deviations caused by phase noise. Hence it is crucial to be able to predict phase noise of an oscillator before we design it.

We can use Leeson's model to model the phase noise of OMOs using the expression of linewidth from equation (x). The following equation gives an expression for phase noise in both $1/f^2$ and $1/f^3$ regimes. ω_{1/f^3} is the corner frequency for $1/f^3$ noise.

$$\begin{aligned} L(\Delta f) &= 10log_{10}\left(\frac{1}{2\pi}.\frac{\Delta\Omega}{\Delta f^2}\right)\ldots 1/f^2 \\ &= 10log_{10}\left(\frac{1}{2\pi}.\frac{\Delta\Omega}{\Delta f^2}.\frac{\omega_{1/f^3}}{\Delta f}\right)\ldots 1/f^3 \end{aligned} \tag{3.8}$$

Based on this model, we can draw some insights into designing oscillators with low phase noise. As can be seen from the equations for linewidth and phase noise, we see that if there could be a way to increase the effective mass of the system, m_{eff} while ensuring that the amplitude of radial displacement, r does not drop as much that $\frac{1}{m_{eff}r^2}$ increases, then we can improve the phase noise of the system i.e. increasing m_{eff} perhaps increases the signal power thereby improving far from carrier phase noise. However, the system becomes stiffer and hence we may need larger input power to overcome this. We propose a solution to this problem by using multiple disks mechanically coupled to each other. Also, we can actuate multiple disks thereby maintaining operating power.

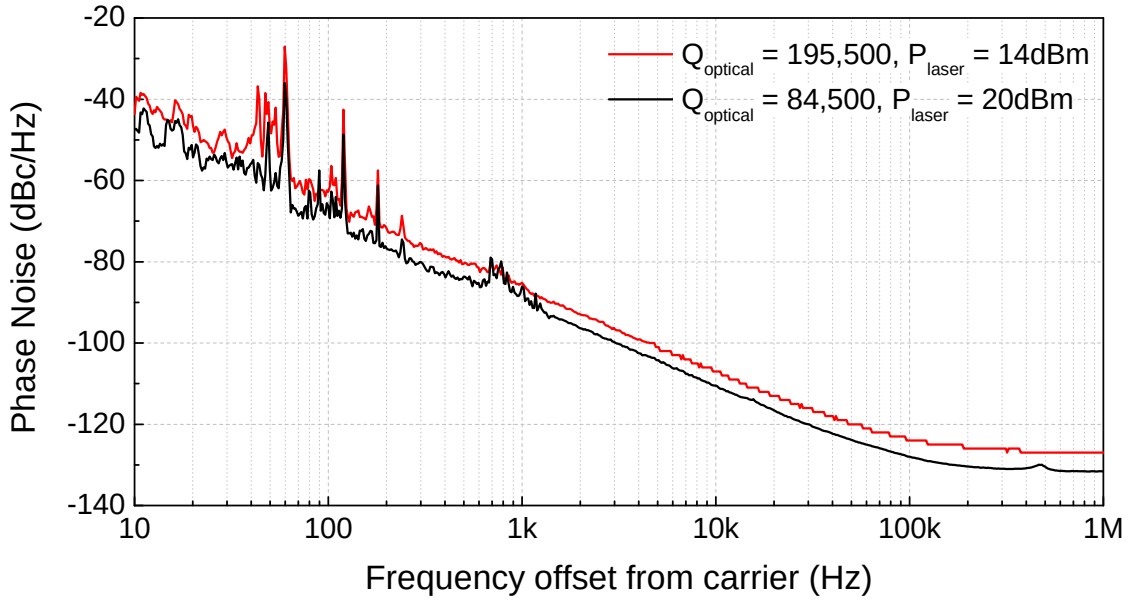

Figure 3.15: 6dB reduction in phase noise of the oscillator achieved by employing a lower optical quality factor (84,500) resonance.

3.5.3 Improving phase noise of the opto-mechanical oscillator

The analytical treatment of opto-mechanical oscillations highlighted the strong dependence of the phase noise on the optical quality factor. As seen in equation 3.4, choosing a lower optical Q $\left(\propto \frac{1}{\Gamma_{tot}}\right)$ resonance while achieving complete modulation can theoretically give better phase noise at a cost of higher threshold power. We employed an optical mode with a total optical Q of 84,500 (and an intrinsic Q of 200,000) and observed a reduction in phase noise by 6dB as shown in Figure 3.15.

3.6 Characterization of Opto-Mechanical Oscillations

This section presents characterization experimental data for the RP driven Si_3N_4 OMO. We perform a wide frequency sweep and observe multiple harmonics of the fundamental oscillation signal, as shown in Figure 3.16. These harmonics are a result of non-linear optical modulation as described in section 2.3.

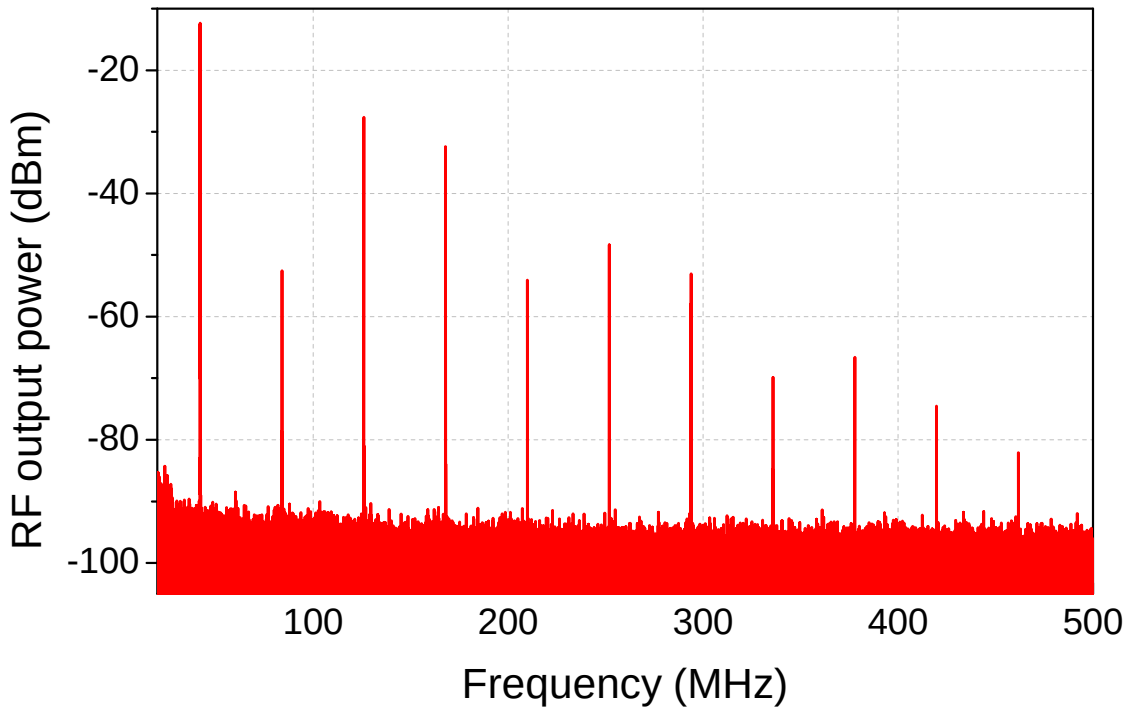

Figure 3.16: Wide frequency sweep showing various harmonics of the fundamental mode for +15dBm laser input power.

Figures 3.17 and 3.18 show the behavior of RF output power and phase noise for the 41MHz signal as we vary the input laser power, while keeping the relative laser detuning from the optical resonance fixed at 0.31.

As we see, the RF output power increases as we increase the input laser power and eventually the rate at which it rises tapers off. The phase noise improves as

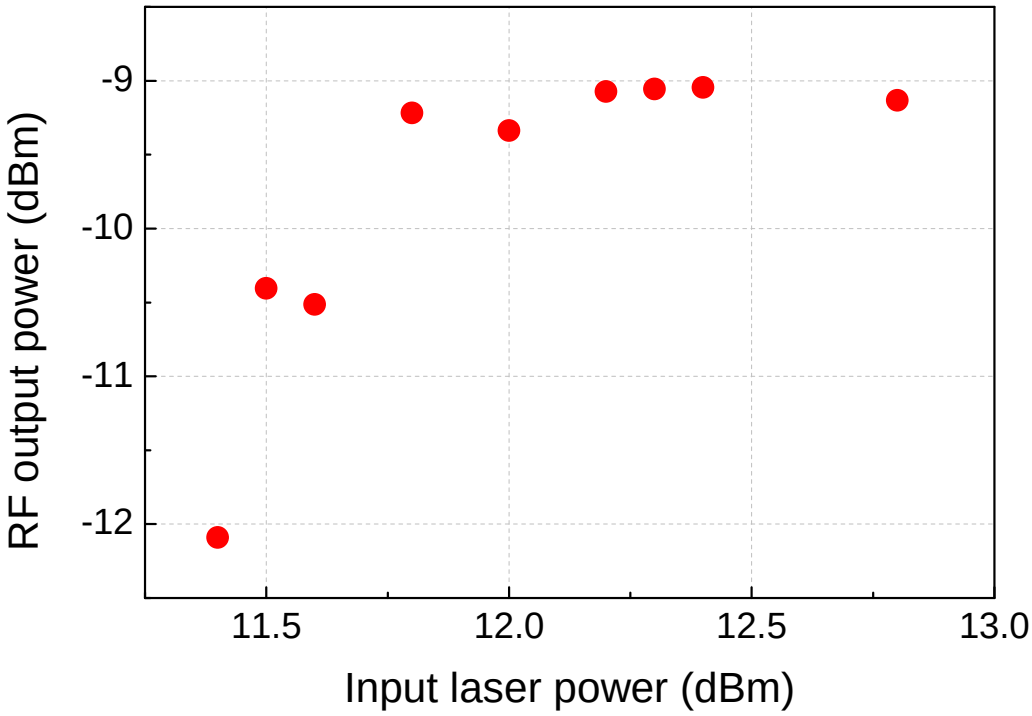

Figure 3.17: Variation of RF output power with input laser power

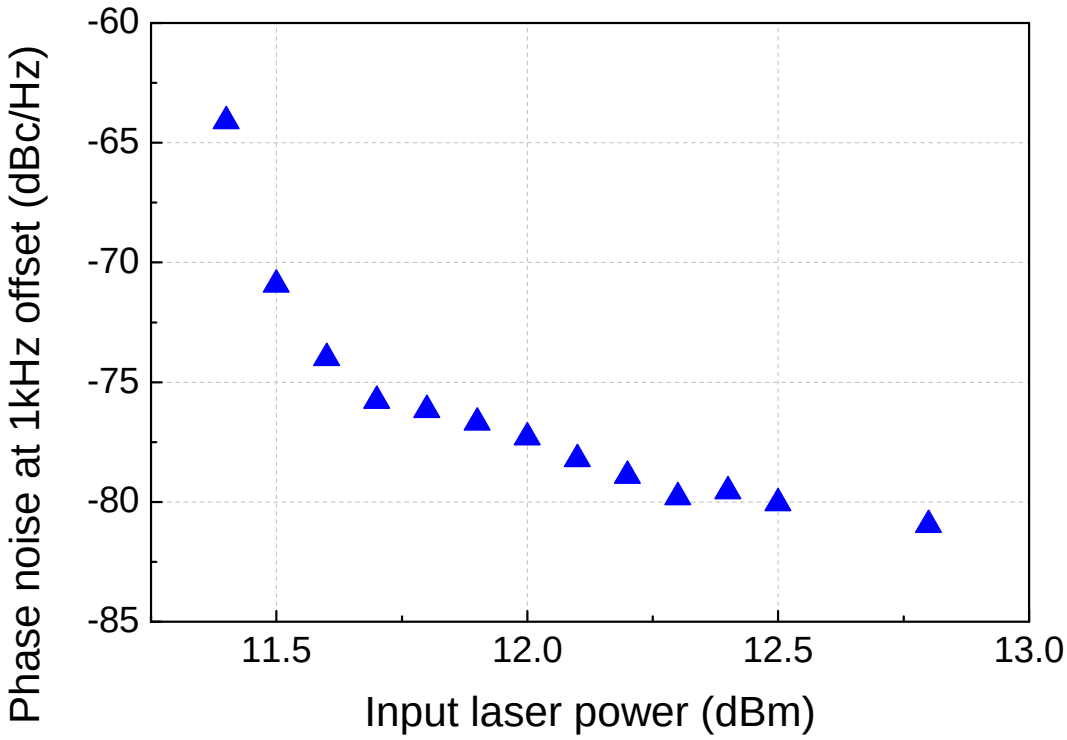

Figure 3.18: Variation of phase noise at 1kHz offset with input laser power

we increase input laser power, eventually following the saturation behavior demonstrated by the RF outputpower. This trend is in good agreement with predictions for radiation pressure driven oscillations in microtoroids [33].

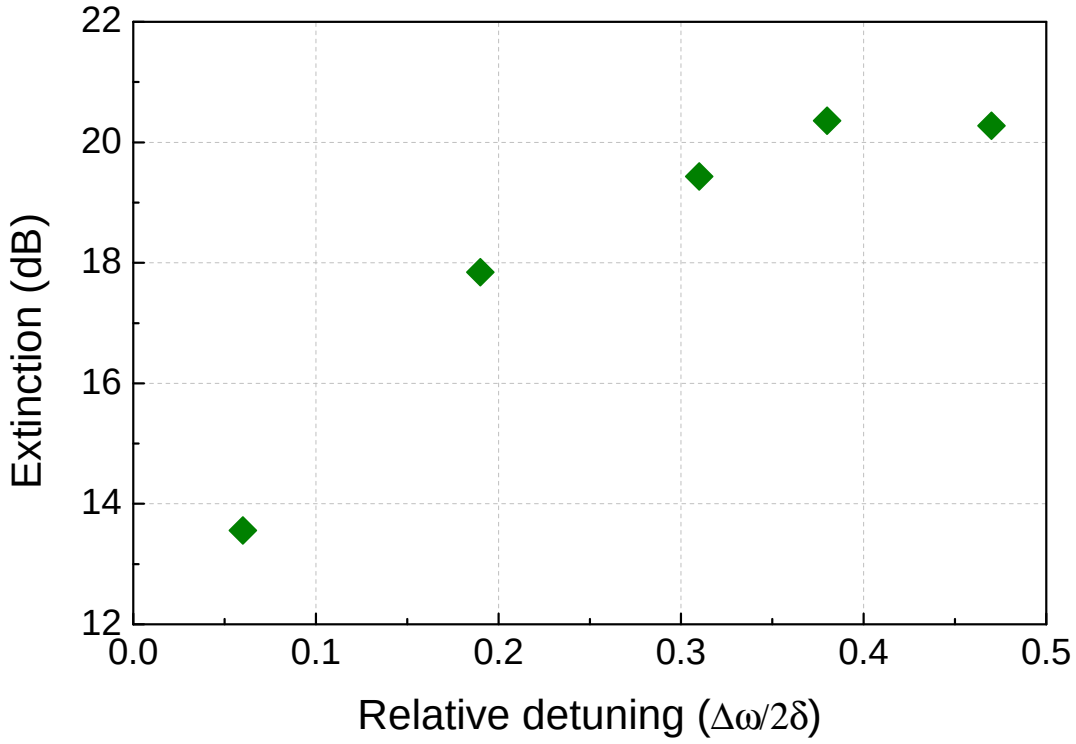

Figure 3.19: Extinction of oscillation waveform at output of the APD measured for various relative detuning values. As we can see, a relative detuning of 0.5 enables us to see maximum extinction of 20dB, which corresponds to extinction at resonance as in Figure 3.10.

Figure 3.19 shows how the extinction of the oscillator varies with relative detuning. Extinction is defined as $E = 10log_{10}\frac{V_{max}}{V_{min}}$, where V_{max} and V_{min} are respectively the maximum and minimum voltage levels at the output of the photodetector. As expected [33], we see a maximum extinction of 20dB for relative detuning of 0.5, which corresponds to extinction at resonance as in Figure 3.10. This implies that the radial displacement amplitude of the disk at 0.5 relative detuning is sufficient

for complete modulation of the laser light.

3.7 Challenges in Scaling Opto-Mechanical Oscillators

3.7.1 Oscillation threshold for GHz operation

Recall from equation 3.4 that the optical power threshold for onset of radiation pressure oscillations scales directly as the mechanical resonance frequency. The threshold power required for self-oscillation mechanical modes beyond GHz frequency accounting for grating losses is >30 dB. At larger frequencies, the required power will be even larger, which makes scaling of this oscillation phenomenon challenging from a pratical perspective.

3.7.2 Nano-opto-mechanical oscillators and phase noise

Following our published work on the integrated silicon nitride opto-mechanical oscillator, various other groups have pursued designing oscillators with smaller effective mass to counter the threshold dependence on frequency. Disk resonators fabricated in GaAs [30] and silicon [42] with oscillation frequencies beyond a GHz have been shown, with optical quality factors in excess of 350,000. However, the reduced effective mass and higher optical quality factor translates directly into larger phase noise numbers, which is undesirable in practically all oscillator applications. Opto-mechanical zipper cavities and opto-mechanical crystals [41] fabricated in silicon have been shown to demonstrate RP oscillations at 2.2GHz and 5.1GHz, making them the highest frequency opto-mechanical oscillators reported to date.

However, these nano-mechanical devices also suffer from very low effective masses on the order of few femto-grams.

Opto-mechanical transduction at frequencies well in excess of a GHz have been shown using optical excitation via optical gradient forces [41], electrostatic actuation [11] and piezo-electric actuation [52]. These methods can be employed to operate the resonator as an opto-mechanical delay element, and an oscillator can be realized in a delay-line oscillator topology. Careful mechanical and optical design can enable a beyond GHz opto-mechanical oscillator. The next chapter presents an oscillator designed using this topology, and rightly termed as the opto-acoustic oscillator.

CHAPTER 4

OPTO-ACOUSTIC OSCILLATOR

In previous work, the OxideMEMS Lab has presented a method for driving motion in an opto-mechanical resonator using the RF MEMS technique of electrostatic capacitive actuation and sensing of mechanical motion in the same resonator using optical intensity modulation. This was achieved in an opto-mechanical resonator all integrated into a monolithic system fabricated on silicon on insulator (SOI) platform [53]. These resonators were employed in an electrical feedback loop to realize micro-mechanical oscillators with frequencies in the GHz range. However, the device and the transduction scheme employed have limitations that prevent the scaling of this resonator design to realize multi-GHz oscillator implementations. This chapter presents modification to the mechanical design, and the drive and sense transduction schemes to realize micro-mechanical oscillation signals beyond GHz.

4.1 Coupled Silicon Opto-Mechanical Resonator

A coupled ring resonator design was employed in [11] to realize a GHz oscillator. The frequency of compound radial expansion mode of the ring is set mainly by the width of the ring with little dependence on its radius. Each ring resonator has an inner radius 5.7μm and width 3.8μm.

The anchoring scheme for the coupled resonator system follows a balanced anchor methodology [54], which moves the anchor over to the coupling beam instead of the resonator boundaries. The coupling beam length corresponds to half the acoustic wavelength, and the beam thus has a nodal point in the middle (see Fig-

ure 4.1). Connecting tethers to this point to mechanically anchor the device and to also route the electrical ground signal to the resonators leads to preservation of high mechanical Q factors while ensuring mechanical symmetry.

4.1.1 Curbing mechanical self-oscillations of waveguide

The optical gradient force acting on the waveguide due to interaction between the light in the resonator with light in the waveguide can launch mechanical self-oscillations in the waveguide. This leads to internal frequency mixing in the opto-mechanical resonator as also observed by Huang et al. [55]. To curb these mechanical oscillations in the waveguide, we intentionally tether the waveguide at the point of coupling to the optical resonator as shown in Figure 4.1 (b). The mechanical stub prevents motion at the coupling point thereby leading to a clean RF transmission comprising solely of the mechanical modes of the coupled ring resonator.

4.1.2 Fabrication Process

Fabricating the photodetector involves a four mask process flow on a custom silicon-on-insulator (SOI) wafer (undoped 250 nm device layer for low optical loss and 3μm thick buried oxide for isolation of the waveguides on device layer from the silicon substrate). The top silicon is thermally oxidized to obtain a thin oxide hard mask layer of thickness 60nm atop a 220nm thick silicon device layer. ma-N 2403 electron beam resist is spun on top of the oxide and patterned using electron beam lithography. The patterns are transferred into the silicon dioxide using a CHF_3/O_2 based reactive ion etcher and then into the silicon device layer using

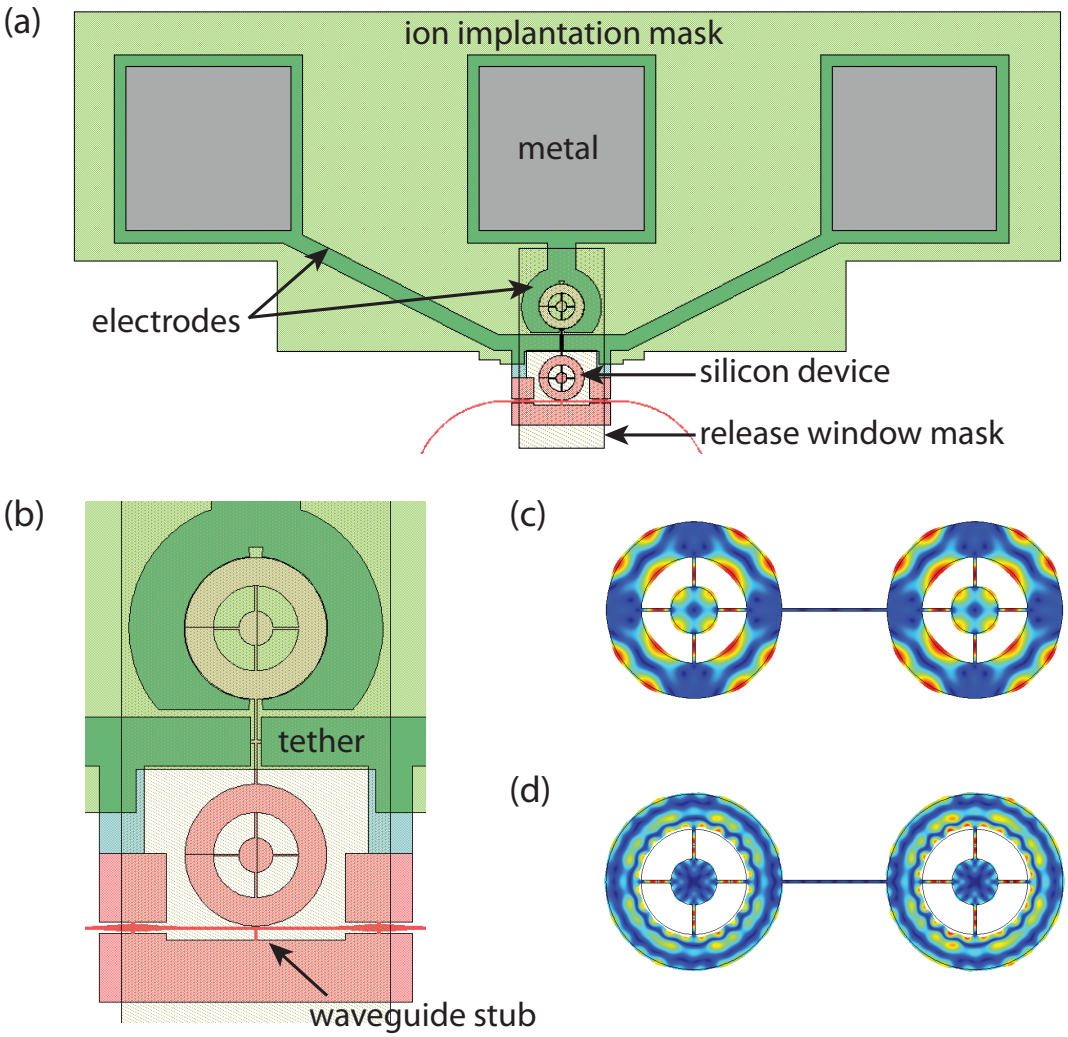

Figure 4.1: (a) Layout depicting the silicon coupled opto-mechanical resonator. (b) Zoomed in view of the tether balanced mechanical anchor and the mechanical stub anchor to curb waveguide motion. FEM simulated mode-shapes of the optimized (c) first order and (d) second order radial expansion modes of the coupled ring-resonator at 1.1GHz and 2.2GHz.

a chlorine based reactive ion etch. A layer of SPR-220 3.0 photoresist is spun and a second mask is used to pattern windows above the mechanical resonator, the electrical routing beams and the bond-pads. This is followed by a boron ion implantation and nitrogen annealing to reduce the resistivity of these structures. A third mask is then used to deposit metal over the bond pads for improved electrical contact. A layer of LOR-5A followed by a layer of SPR-220 3.0 is spun and the bond pads are exposed via contact alignment photolithography. This is followed by evaporation of 25nm nickel on the sample. Nickel forms a good ohmic contact with silicon, and is hence chosen as the bottommost metal. After evaporating nickel, we evaporate 25nm titanium and 50nm platinum. Platinum is used as the top metal as it makes good electrical contact with the Cascade Air Coplanar Probe (ACP) RF probe used to interrogate these devices. However platinum does not adhere well to nickel, and hence titanium is used as an adhesion layer. The photoresist is dissolved in Microposit remover solvent 1165 to leave metal only atop bond-pads. A fourth mask is used to pattern release windows near the resonator using SPR-220 3.0 photoresist, followed by a timed release etch in buffered oxide etchant to undercut the devices. The samples are then dried using a critical point dryer to prevent stiction. Figure 4.2 shows an illustration of the fabrication process. Figure 4.3 (a) and (b) show scanning electron micrographs (SEMs) of the fabricated devices and the resonator-waveguide gap respectively. The gap is chosen to be 100nm to ensure critical coupling to multiple optical modes.

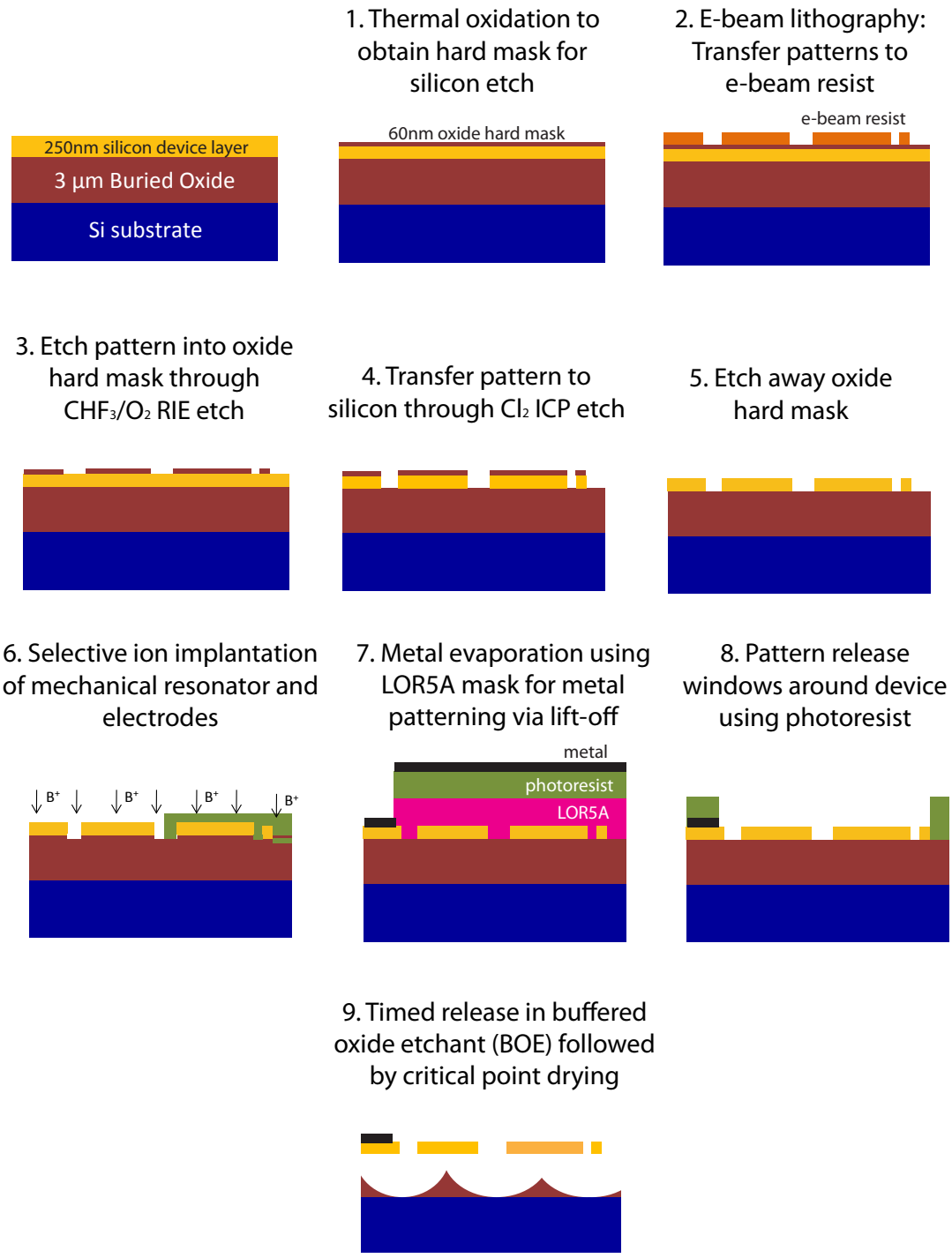

Figure 4.2: Illustration of fabrication process flow for designing coupled silicon opto-mechanical resonators in a silicon-on-insulator (SOI) platform

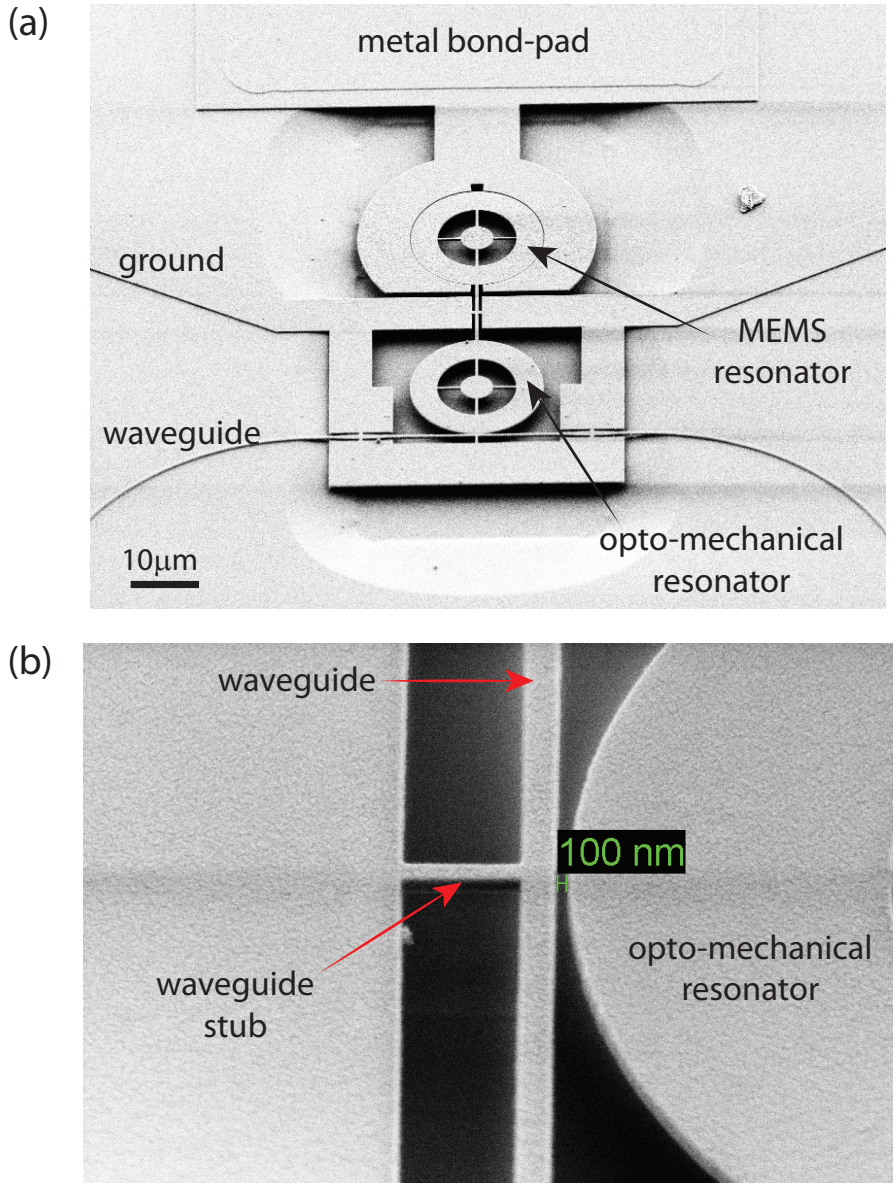

Figure 4.3: (a) SEM of the fabricated coupled silicon opto-mechanical resonator. (b) The waveguide-resonator gap is chosen to be 100nm to ensure critical coupling to multiple optical modes.

4.2 Resonator Characterization

4.2.1 Optical characterization

The scheme for optical characterization of the silicon opto-mechanical resonator is identical to that for the silicon nitride opto-mechanical resonator, as detailed in section 3.4. Figure 4.4 (a) shows a typical optical spectrum recorded for this resonator. The waveguide couples to various optical resonances. Figure 4.4 (b) shows a high Q optical resonance centered at 1557.84nm with a total optical quality factor of 31,000. The grating couplers introduce a loss of 6dB at each facet, and have a full width at half maximum (FWHM) bandwidth of 40nm.

4.2.2 Electro-mechanical characterization

To identify the mechanical modes of the resonator, we characterise the RF transmission of the resonator using a network analyzer. Figure 4.5 shows a schematic of the experimental setup. A bias-tee is used to apply a combination of DC bias voltage along with AC power from port 1 of an Agilent N5230A network analyzer at the probe-pads of the electrode with a Cascade GSG RF probe. The tunable laser is blue detuned to the half maximum point of the optical cavity. Mechanical motion of the device induced by the applied input voltage translates into intensity modulation of the laser light, which is picked off and converted into electrical RF signal by a Newport 1544-A near-IR photoreceiver connected to the optical fiber output. The output of the photoreceiver is connected to port 2 of the network analyzer. The RF frequency is swept from 100MHz to 10GHz and the transmission spectrum for the modulator is recorded. Figure 4.6 shows a typical transmission

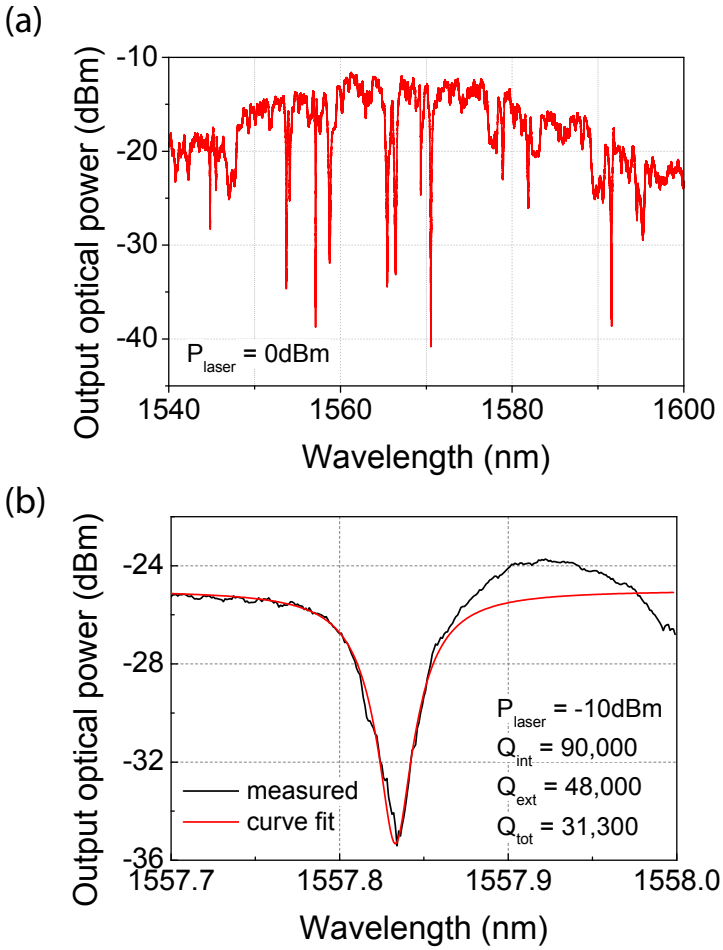

Figure 4.4: (a) SEM of the fabricated coupled silicon opto-mechanical resonator. (b) The waveguide-resonator gap is chosen to be 100nm to ensure critical coupling to multiple optical modes.

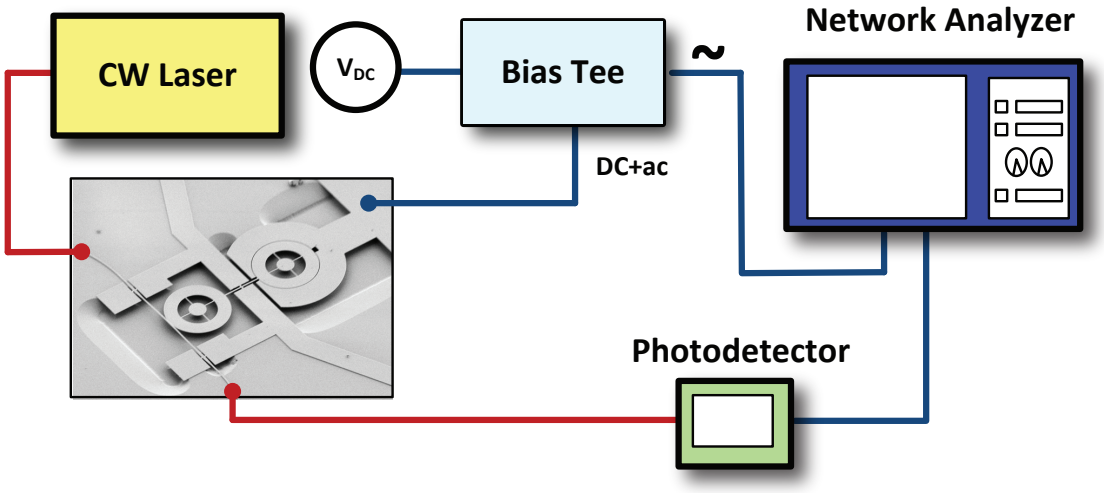

Figure 4.5: Experimental setup for characterization of the RF transmission of the modulator.

spectrum obtained for such a two coupled-ring resonator. These spectra can be obtained at a variety of DC voltage and laser power combinations.

4.3 f-Q Scaling in Micro-Ring Resonators

MEMS resonators designed for oscillator applications to date have quality factors lower than the TED limit [56, 57]. For designing high performance oscillators, two figures of merit that one should maximize are $f-Q$ (mechanical frequency-quality factor product) and k_t^2-Q (electromechanical coupling constant-mechanical quality factor product), which dictate the close to carrier phase noise and mechanical energy stored in the resonator respectively. While progress has been made towards optimizing the latter [58, 59], resonators demonstrating high f-Q products close to the TED limit have managed to do so at expense of feed-through, thus necessitating indirect measurement techniques such as local oscillator (LO) mixing [60] or FET-

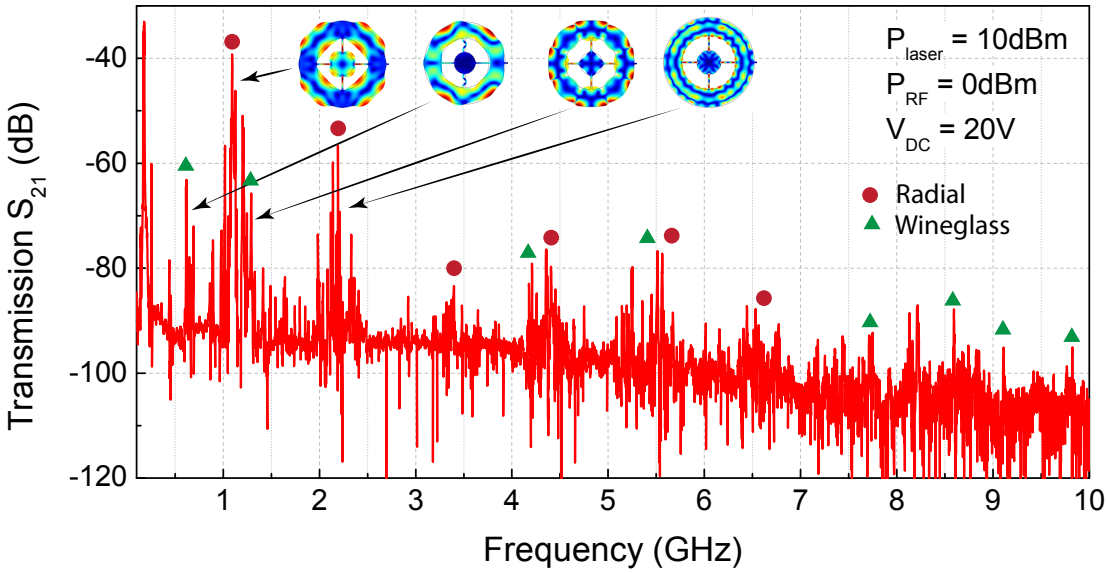

Figure 4.6: Wide RF transmission spectrum of the resonator. Various mechanical modes of the device are sensed via optical intensity modulation at the photo receiver. A combination of 0dBm RF power and 20V DC bias was applied at the electrodes. Insets: COMSOL simulations of mode-shapes for fundamental and second order wineglass mode and radial mode. Key modes are indicated using circles (radial) and triangles (wineglass).

based sense [22].

The quest for designing a low phase noise opto-acoustic oscillator requires identifying mechanical modes with high $f - Q$ products. For our integrated silicon opto-mechanical resonator, we choose a ring geometry over a disk as the former combines the ability to achieve high mechanical frequencies and high capacitive actuation area. Wineglass modes of such resonators have been studied previously from theoretical [31] and experimental [60] standpoints. In case of 4-spoke supported released ring resonators, wineglass modes have less stress distribution along the inner perimeter of the ring in the two orthogonal 0°-180° and 90°-270° directions. In comparison, radial mechanical modes can never have zero stress distribution at the ring perimeter and thus are expected to have lower mechanical Qs. Moreover higher harmonics of wineglass modes have lesser stress near the spokes and thus should be more immune to anchor loss [61]. An illustration of this is shown in Figure 4.7, which compares the stress distribution for two compound wineglass modes. The stress in the orthogonal axes at points on the inner periphery of the ring resonator is smaller for the higher harmonic as compared to the fundamental mode. Lower anchor losses at higher frequencies augur well for designing low phase noise oscillators employing these higher order mechanical modes.

The integrated electro-mechanical drive and opto-mechanical sense scheme we have developed offers a direct measurement platform to probe the mechanical modes of MEMS resonators. Indeed, the high sensitivity provided by this scheme makes it possible to detect thermal Brownian motion of these resonators. This chapter uses this scheme to study frequency scaling of quality factors of wineglass modes and radial modes in ring resonators. The next section provides details on a

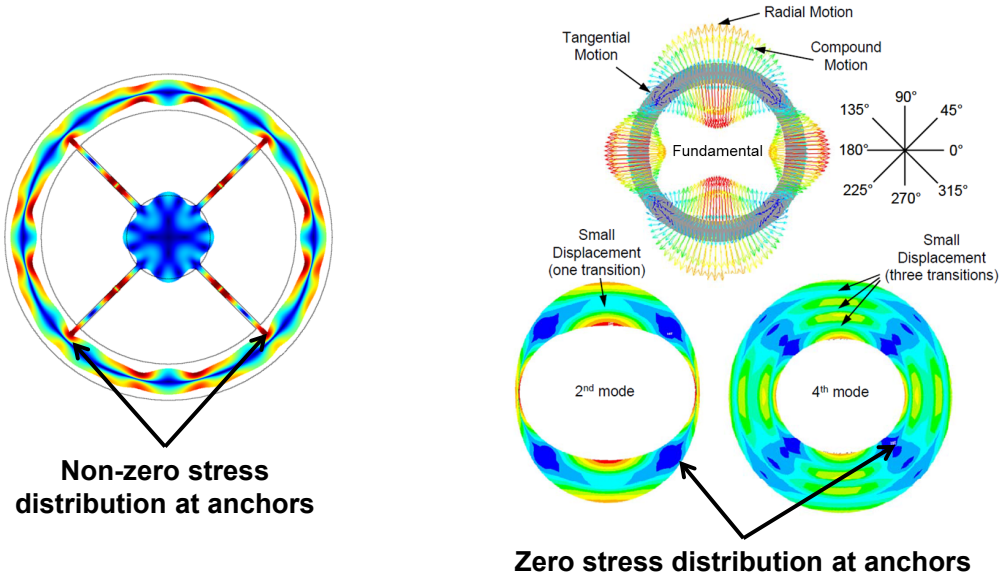

Figure 4.7: Illustration comparing immunity of wineglass mechanical modes (right) to anchor losses unlike radial modes (left).

qualitative comparison of wineglass and radial modes and trends to expect. Then we present experimental results to study these trends and derive insights based on our findings to design higher performance oscillators.

4.3.1 Anchor loss limited quality factor

The measured f-Q product for the mechanical resonance at 1.1GHz is 2.7x10^{12}Hz, which is far lower than the f-Q product of silicon due to material losses [62]. Demonstrations of quality factors of 18,000 at 3.72GHz in silicon [22] have been realized, which approaches values very close to the material limit. To investigate the anchor losses in the coupled silicon opto-mechanical resonator, we turn to COMSOL finite element method (FEM) simulations. The technique for estimating anchor losses uses a perfectly matched layer in COMSOL was explained by Steeneken et al. [63].

The simulation treats acoustic energy transfered into the substrate through the anchors as loss using a matched layer. Figure 4.8 shows the trend in anchor losses estimated for radial and wineglass modes for the coupled ring resonator. Higher order radial modes exhibit a saturation of the f-Q product in sharp contrast to increasing trend observed in higher order wineglass modes. This behaviour is attributable to the increased immunity to anchor losses in higher order wineglass modes.

4.3.2 Thermo-elastic damping (TED) limited quality factor

In order to improve the resonator, the designer needs to consider all aspects that produce damping and noise in the system. For example, resonators are usually run in vacuum to minimize effects of air and squeeze-film damping.

Thermo-elastic damping (TED) [64, 65] is an important factor that the resonator designer needs to address. It is a result of a phenomenon called thermoelastic friction, which takes place when you subject any material to cyclic stress. The stress results in deformation, and the required energy is mostly stored as internal potential energy. However, materials heat under compressive stress and cool under tensile stress. Thus, due to the heat flow from warmer to cooler regions energy is also lost as nonrecoverable thermal energy. The amount of thermo-elastic friction and damping depends on the rate of this energy loss. The magnitude of the energy loss depends on the vibrational frequency and on the structures thermal relaxation time constant, which is the effective time the material requires to relax after an applied constant stress or strain. Therefore, the effect of thermo-elastic

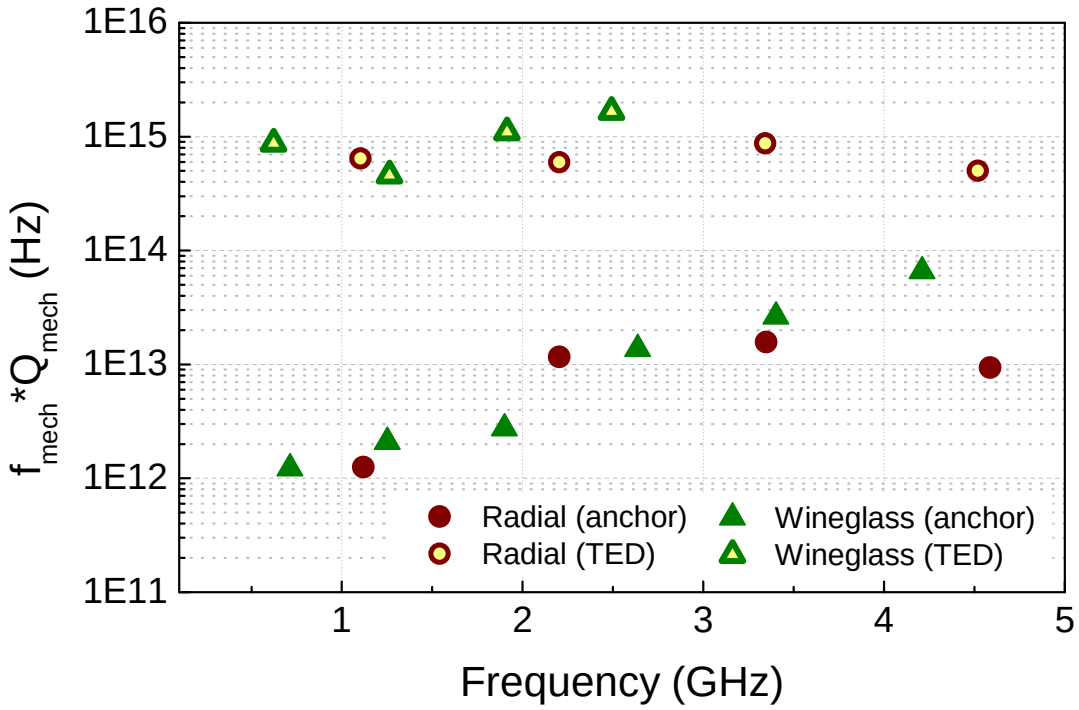

Figure 4.8: Comparison of FEM simulated f-Q products for TED and anchor loss mechanisms. The TED limited f-Q values are two orders of magnitude larger than the anchor loss limited f-Q products, which indicates that anchor loss mechanisms determine the quality factor in the resonator.

dissipation, and consequently the damping, is most pronounced when the vibration frequency is close to the thermal relaxation frequency. Analytical expressions for the TED limited quality factor are possible to be obtained for simple structures such as uniform beam resonators [66]. However, for complicated structures such as a coupled ring resonator system, it is preferrable to use finite element method simulation (FEM) with an eigenfrequency analysis that combines heat transfer and structural mechanics in one equation system. The eigenmodes thus obtained are thermo-elastic.

Figure 4.8 shows the FEM simulated TED limited Q values for the device com-

pared to the anchor loss limited Q values also obtained from FEM simulations. The net quality factor, Q_{net}, depends on Qs from all loss mechanisms in the resonator, Q_i as $\frac{1}{Q_{net}} = \sum \frac{1}{Q_i}$. In other words, the loss mechanism with the largest loss determines the ultimate quality factor of the resonator. The plot clearly shows that the coupled ring-resonator system is dominated by anchor losses.

4.3.3 Comparison of f-Q product in radial and wineglass modes

Using the direct acousto-optic characterization scheme, we measure the quality factor for the different modes belonging to the radial and wineglass mode families. Figure 4.9 shows the variation of f-Q for these modes. The Q for radial mode decreases for higher order modes in such a way that the measured f-Q saturates to a value close to $9x10^{12}$Hz. In contrast to the radial mode, the f-Q for the wineglass mode family increases for higher harmonics. This measured trends are similar to those obtained via FEM simulations. The highest f-Q is measured to be $5.11x10^{13}$Hz at 9.82GHz. These measurements were performed in air and at room temperature.

4.3.4 Temperature scaling of f-Q product in radial and wineglass modes

Based on the measurements we perform at room temperature, we believe the quality factors for the radial modes are limited by anchor losses. To corroborate this hypothesis, we investigated the variation of quality factors for the wineglass and

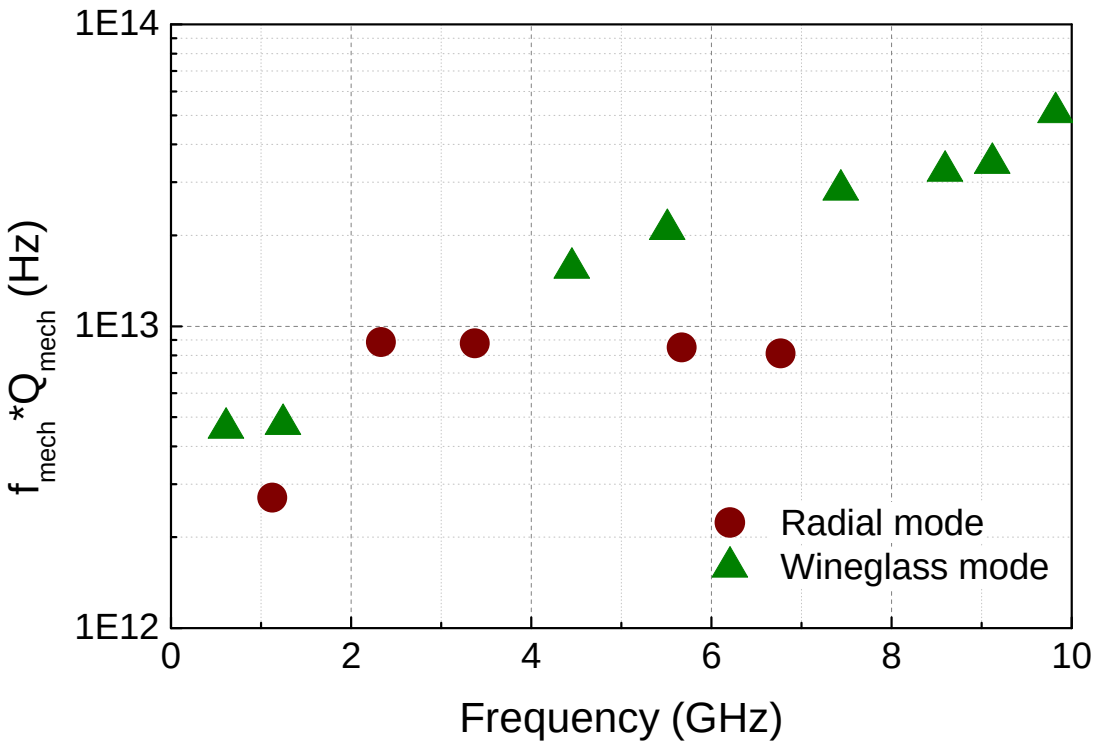

Figure 4.9: f-Q vs f plotted for harmonics of the radial mode and the wineglass mode. Unlike the radial mode, the f-Q for the wineglass mode does not saturate and the value for higher harmonics keeps increasing. Measurements were carried out at room temperature and atmospheric pressure.

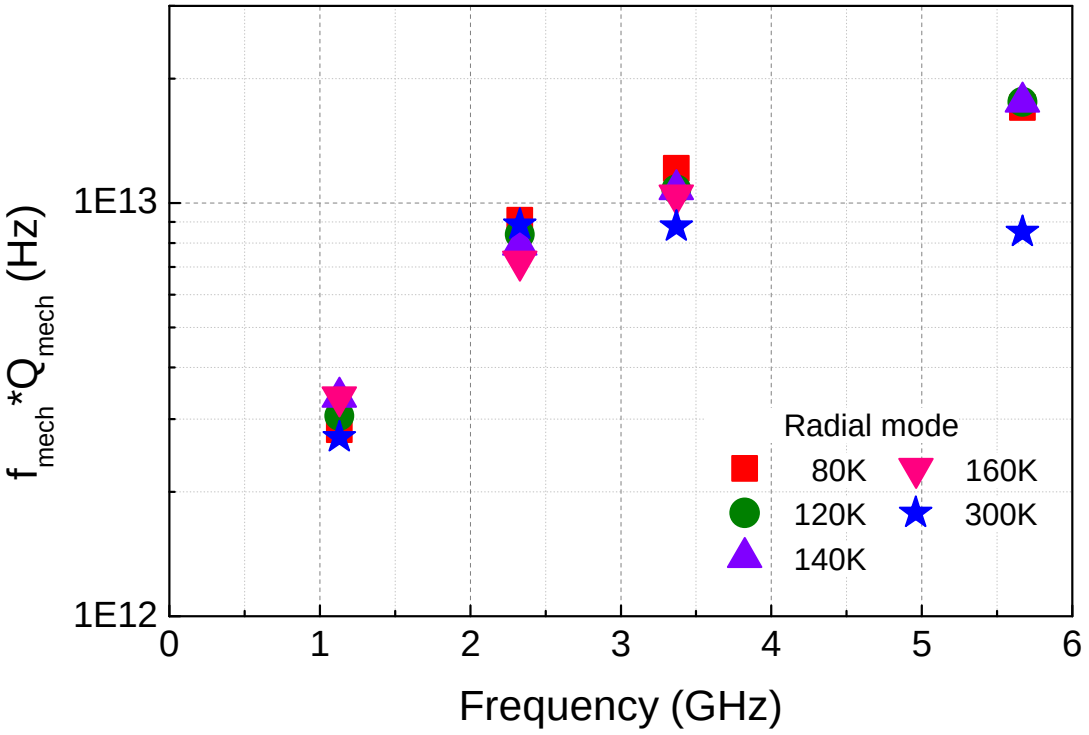

Figure 4.10: f-Q vs f plotted for harmonics of the radial mode at various temperatures. At room temperature the f-Q for higher harmonics of the radial mode saturates at a value close to 9x10^{12}Hz. At lower temperatures the value of f-Q shows an increasing trend.

radial mode families with temperature. The device was tested in a Lakeshore TTP4 probe station under 9μTorr pressure, and liquid nitrogen was used to cool the chamber. A modified optical probe arm was introduced in the probe station to couple laser light to the devices via grating couplers.

We measured the performance of this modulator at various temperatures down from room temperature to 80K. The TTP4 optical probe arm connectors introduce further losses in addition to the losses due to grating couplers. This limits the highest observable signal frequency to roughly 6GHz, and displacement sensitivity at frequencies beyond this value is limited by noise.

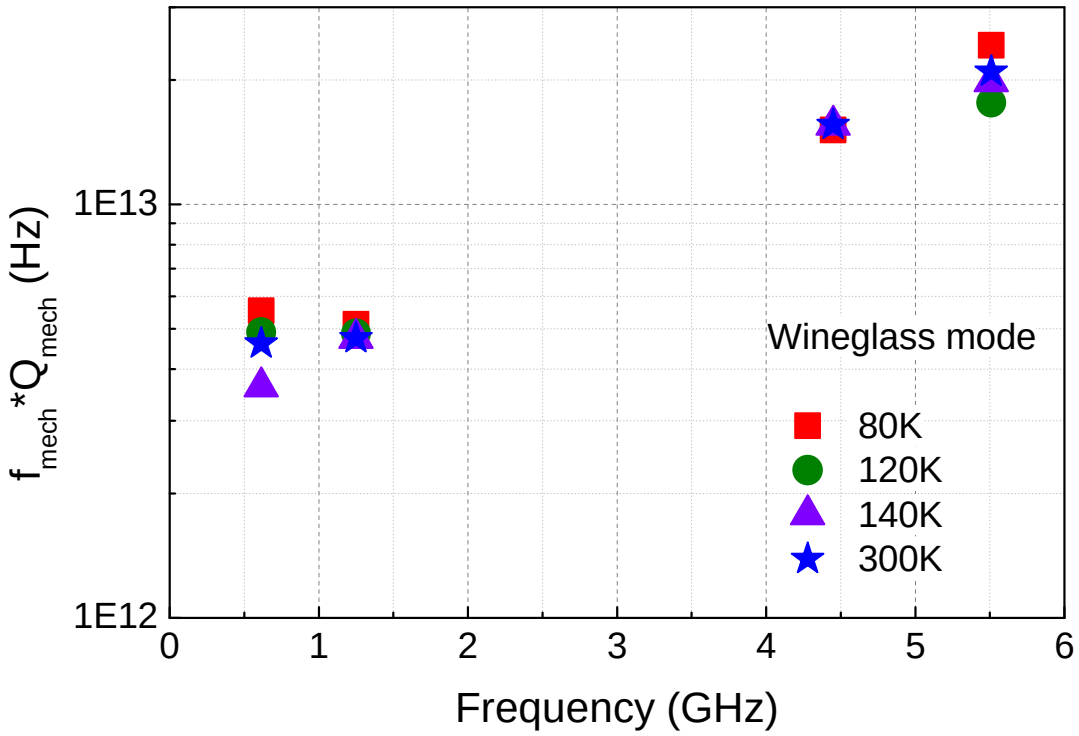

Figure 4.11: f-Q vs f plotted for harmonics of the wineglass mode at various temperatures. The f-Q for higher harmonics shows a rising trend at all temperatures.

Figure 4.10 shows the variation of f-Q as a function of temperature for the radial mode family. The saturation in the value of f-Q for higher order modes seen at room temperature no longer holds and the variation shows a rising trend. It would be misleading to interpret this as transition from anchor-loss dominated regime to phonon-phonon dissipation limit. The measured value of f-Q at 5.67GHz at 80K is 10X lower than the maximum calculated limits for <100> silicon [62]. The wineglass mode family on the other hand, shows an increasing trend in the f-Q product for higher order modes at all temperatures as seen in Figure 4.11. As in the case of radial modes, the values measured are far lesser than the theoretical limit [62]. This implies that higher harmonics of the wineglass mode are more resilient to anchor losses.

4.4 Limitations of Two Coupled-Ring Resonator Architecture

Careful design of the coupling spring for a compound radial mode at 1.1GHz ensures a low insertion loss (<30dB) for the coupled opto-mechanical resonator, which allows us to operate the resonator as an oscillator in a closed feedback loop [11]. The insertion loss for higher order radial modes at 2.2GHz (>60dB), 3.3GHz (>80dB) however are significantly higher which makes it difficult to design oscillators using these mechanical modes (see Figure 4.6). Scaling the design to a compound radial mode of 2GHz, by resizing the ring width to 2μm and inner ring radius to 7μm results in significant insertion loss (>40dB) at the frequency of interest, as shown in Figure 4.12. for the original coupled ring design.

The primary reason for increased insertion loss are 1) inefficient acoustic transduction at higher mechanical frequencies and 2) lesser displacement sensitivity of the optics due to reduced overlap of the motional sidebands with the optical cavity resonance lineshape. We first present two solutions to overcome the inefficiency of the acoustic transduction scheme, elaborated in the next section. The last section of this chapter presents a solution to boost the efficiency of the optical sense scheme.

4.5 Micro-Resonator Arrays

The silicon opto-mechanical resonator system presented in the sections above exhibits very large RF insertion losses at frequencies beyond 1GHz. The transduction efficiency of electrostatic capacitive actuation at higher frequencies is strongly

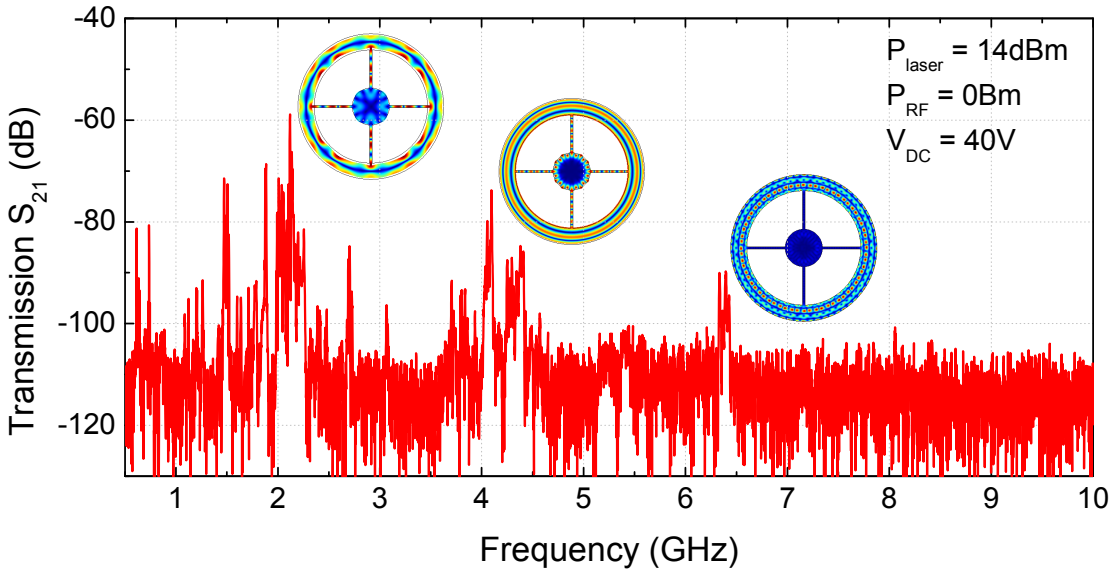

Figure 4.12: RF transmission spectrum for a 2μm wide ring measured using a network analyzer. The insertion loss for the fundamental, second order and third order radial expansion modes at 2.1GHz, 4.2GHz and 6.3GHz respectively are too large to operate the mechanical resonator as an oscillator in a closed feedback loop. Insets show the corresponding FEM simulated mode shapes for the three radial modes of vibration.

determined by the electrode-resonator gap, and consequently higher frequency mechanical modes have a large motional impedance due to reduced electrostatic force, higher stiffness and smaller motion amplitudes. A thorough mathematical treatment is presented in the next section. The smaller motion amplitude also results in incomplete optical modulation, and thereby the sense scheme displacement sensitivity is also limited.

Among the most direct methods for lowering the motional resistance of capacitively transduced micromechanical resonators are: 1) scaling down the electrode-to-resonator gap, and 2) raising the dc-bias voltage. However, both these methods come at a cost of reduced linearity of the transduction scheme. It has been shown in the past that implementing an array of identical mechanical resonators coupled mechanically helps lower the motional resistance R_x [67] and also achieves larger displacement [68]. These two schemes are elaborated in the follwoing sub-sections:

4.5.1 Lowering resonator motional impedance

Consider an array of N mechanical resonators coupled mechanically using half-wavelength coupling beams as shown in Figure x. This system is analogous to N R-L-C resonators connected in parallel to each other. The composite array has an effective mass $M'_{eff} = NM_{eff}$ and an effective stiffness $K'_{eff} = NK_{eff}$, where M_{eff} and K_{eff} are the effective mass and stiffness for each individual resonator. By driving all the resoantors in the array, the transducer area A is also increased to $A' = NA$. This results in an N-fold increase in the transduction coefficient $\eta = V_{dc}\epsilon_0\frac{A}{g^2}$, where V_{dc}, ϵ_0 and g are the applied DC voltage, permitivitty of air and the resonator-electrode gap respectively. Ideally, this leads to an N-fold reduction in the motional resistance R_x:

$$R'_x = \frac{\sqrt{K'_{eff}M'_{eff}}}{Q_{mech}\eta'^2} = \frac{1}{N}\frac{\sqrt{K_{eff}M_{eff}}}{Q_{mech}\eta^2} = \frac{R_x}{N} \tag{4.1}$$

The above equation assumes perfect matching between the resonator frequencies and quality factors. Even a tiny deviation in frequency from a matched case leads to spurious modes around the mechanical mode of interest and lead to lesser than N-fold reduction in the motional resistance [67]. This problem can be overcome by controlling the phase of the AC voltage drive on each resonator individually. However, practical implementation of this scheme presents routing challenges and additional experimental complexity, and hence we choose to use a single phase drive for subsequent experimental demonstrations.

4.5.2 Displacement amplification

As derived in equation 2.9, if the laser frequency is detuned to the full-width-half-maximum (FWHM) point of the optical resonance, ω_{opt}, the modulation depth depends linearly on the motion induced frequency shift. The opto-mechanical coupling coefficient for a micro-ring resonator is given by $g_{om} = \frac{d\omega_{opt}}{dR} = -\frac{\omega_{opt}}{R}$, where R is the radius of the micro-ring. Thus, larger mechanical displacement translates to greater shift in the resonance frequency, thereby enhancing the modulation depth. Hence it is desirable to get large mechanical displacements in addition to operating in the resolved sideband regime, to achieve efficient modulation.

The acousto-optic modulator presented in section 4.2 is extended to an array of mechanically coupled ring resonators for large electrostatic driving force. We also use a mechanical lever system [68] to realize displacement amplification. An array composite of rings on the input electrostatic side feeds via an acoustic quarter-

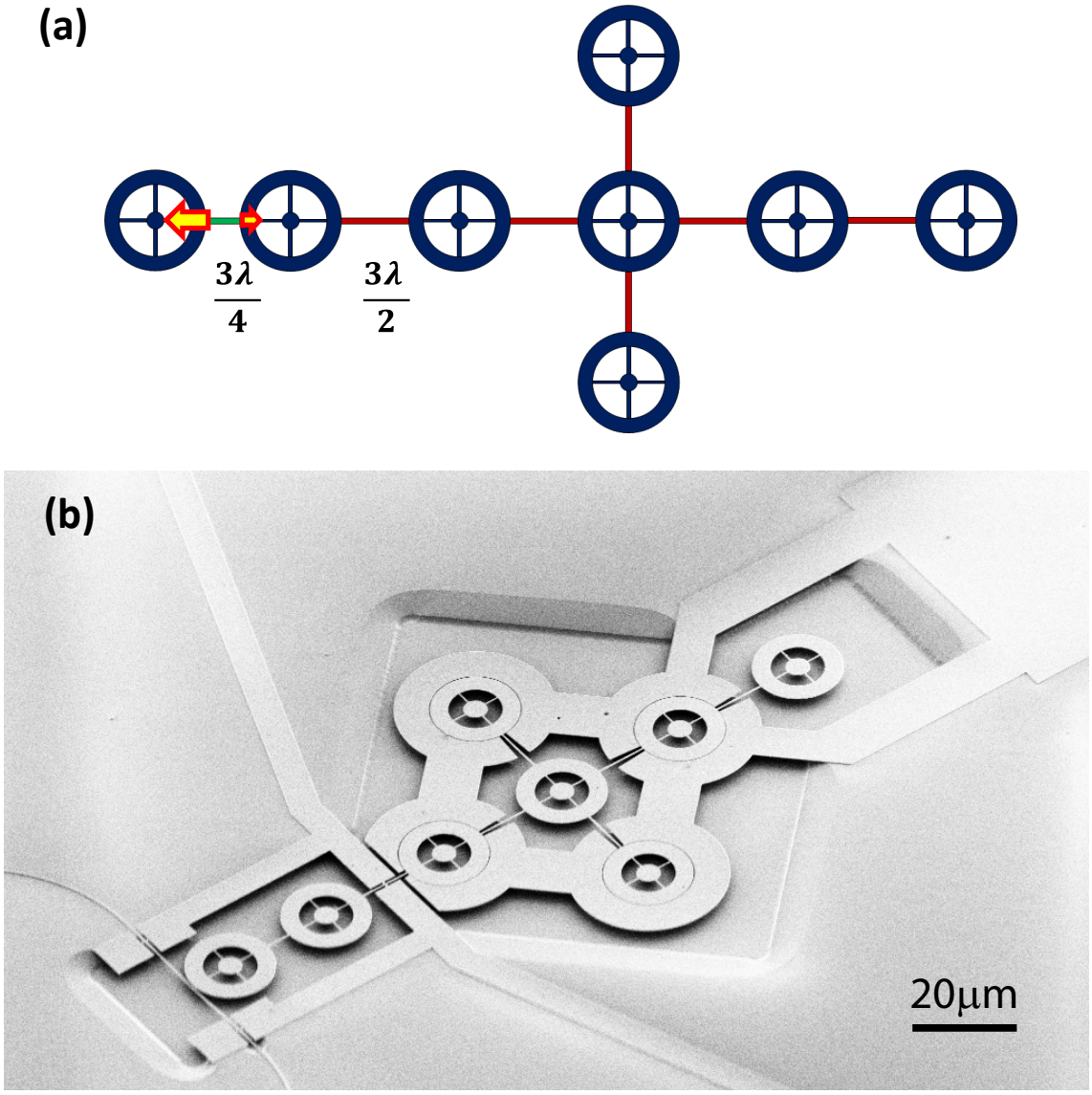

Figure 4.13: (a) Illustration of the micromechanical displacement amplifier. The three-quarter wavelength coupling beam connecting the output opto-mechanical resonator on the left to the array composite of drive micro-mechanical resonators on the right ensures mechanical displacement amplification. (b) Scanning electron micrograph (SEM) of the fabricated acousto-optic frequency modulator (AOFM). Insets: Finite element simulation (FEM) of the mechanical mode shape of the ring at 176MHz (left - fundamental radial expansion mode) and 1.09GHz (right - compound radial expansion mode).

wavelength coupling beam into a single output opto-mechanical ring resonator, as illustrated in Figure 4.13 (a).

Consider a strongly coupled array of N ring resonators strongly coupled to each other using half-wavelength coupling beams. The effective stiffness of the composite resonator defined by the array is $K_{eff} = NK_r$, where K_r is the stiffness of each individual ring. Coupling this array to another ring resonator using a quarter-wavelength coupling beam results in a mismatch of the stiffnesses on either side of this coupling beam. A quarter-wavelength coupling beam, by definition, forces the velocity at both ends of the beam to be the the same. Thus, the kinetic energy of the moving ends of the coupling beam, and hence the stored potential energy in the resonators on either end of the beam is the same. Thus, if x_o is the radial displacement of the output opto-mechanical ring resonator, and x_{array} is the radial displacement of each ring resonator in the array, the energy constraint ensures:

$$\frac{1}{2}K_r x_o^2 = \frac{1}{2}K_{eff} x_{array}^2 \Rightarrow \frac{x_o}{x_{array}} = \sqrt{N} \tag{4.2}$$

Thus, the difference in stiffnesses of the input array and output ring results in an enhancement of the displacement at the output. Figure 4.13 (b) shows an SEM of an array of such resonators employing displacement amplification.

4.6 Partial Air Gap Transduction via Atomic Layer Deposition (ALD)

Conventional air gap capacitively-transduced RF MEMS resonators typically have high motional impedances on the order of a few kΩ [69, 70, 56]. Sub-GHz partial gap resonators with 10 nanometer air gaps achieving impedances <1kΩ have been shown [71]. Extending the frequency of these resonators entails scaling of resonator dimensions, leading to increased motional impedance at higher frequencies. Dielectric electrostatic transduction has several benefits over conventional capacitive air gap transduction schemes for higher frequencies and smaller dimensions [72]. However, there is no clear understanding on which of these transduction schemes is better for a given design frequency and desired mode shape of the resonator. The following sections discuss integrating a partial air gap transduction scheme into the fabrication of the coupled silicon opto-mechanical resonator.

Motional impedance models for air gap transducers [73] and internal dielectric transduced resonators [72] are available in literature. However, partial air gap transduction lacks a good analytical BVD model in literature that can accurately predict resonator performance for varied applications. Designers often feel the need for a complete model for dielectric transduction that can help them determine the motional impedance for various schemes for their design of choice, thereby enabling them to pick a scheme that works best. An earlier attempt to model partial gap beam resonators [71] was limited by distortions of the beam geometry at the resonator-electrode interface, resulting in significant deviation from measured results. Appendix D presents a model that is built on the methodology presented in [73].

4.6.1 Choosing the right ALD material

Deriving insights from equation D.10, we note that to achieve significant reduction in R_x, it is desirable to use a material with large dielectric constant (ϵ_2). Intuitively, this amounts to a net resonator-electrode capacitance comprised of the reduced air gap capacitor connected in series with the capacitors formed by the dielectric on the resonator and the electrode. For reduced R_x, it is necessary that the net capacitance be dominated by the air gap capacitance, since the modulation of this capacitance with displacement is the prime determinant of the motional current.

Atomic Layer Deposition (ALD) provides a uniform and conformal film deposition with sub nanometer thickness accuracy controlled by the number of reaction half cycles used. When working with thin film resonators, such as those employed here for opto-mechanics, it is important to keep in mind the mass loading on the resonator and coupling beams due to the ALD material, which leads to a degradation in the mechanical quality factor due to sub-optimal coupling post ALD. For this reason, it is important to choose an ALD material that is closely matched in acoustic velocity to the resonator material (Si). Also, it is beneficial to identify an ALD material that is easy to etch/pattern, in order to get rid of ALD material over areas of the chip where ALD coating is undesirable e.g. on the bond-pads used to establish electrical contact with the resonator and electrodes. Keeping these reasons in mind, the prime ALD candidates for s Si resonator are aluminum nitride (AlN) and alumina (Al_2O_3), which lead to significantly lower distortions in mechanical Q compared to conventionally employed materials with higher dielectric constants such as hafnia (HfO_2) and titania (TiO_2) [74].

4.6.2 Fabrication process incorporating ALD alumina

We transfer the released devices as fabricated in section 4.1 into an ALD chamber and blanket coat the entire chip with 30nm alumina (Al_2O_3). We then need to remove the alumina deposited on the bond pad to be able to make electrical contact to our device. Also we cannot spin coat photoresist on our sample as the released devices would then break off due to shear force. Instead we spray coat the sample with 6μm thick diluted photoresist (1:10 S1805:Acetone) and pattern the resist via contact photolithography to expose the bond pads. We develop the resist using tetramethylammonium hydroxide (TMAH) based developer. This developer also simultaneously etches the exposed alumina without damaging the bond pads. We then strip the resist in acetone and finally dry the devices using a critical point dryer. Figure 4.14 shows an illustration of the fabrication process flow. SEM images show clear reduction in the resonator-electrode gap from 130nm to 70nm post ALD (see Figure 4.15).

4.6.3 Post-release photolithography on a MEMS structure

Ultrasonic photoresist spray equipment is used in photolithography wafer processing, often as an alternative to spin coating or vapor deposition for thin film processing of MEMS or other semiconductor wafers needing uniform conformal coating of areas with high aspect ratios. These processes often require ultra precise uniform thin film coatings of photoresist into difficult areas such a V-grooves and deep vertical trenches. This same spray-coating technique can be adopted to obtain photoresist coating on a suspended MEMS structure. Conventional resist spin coating will damage the suspended structure due to shearing forces encoun-

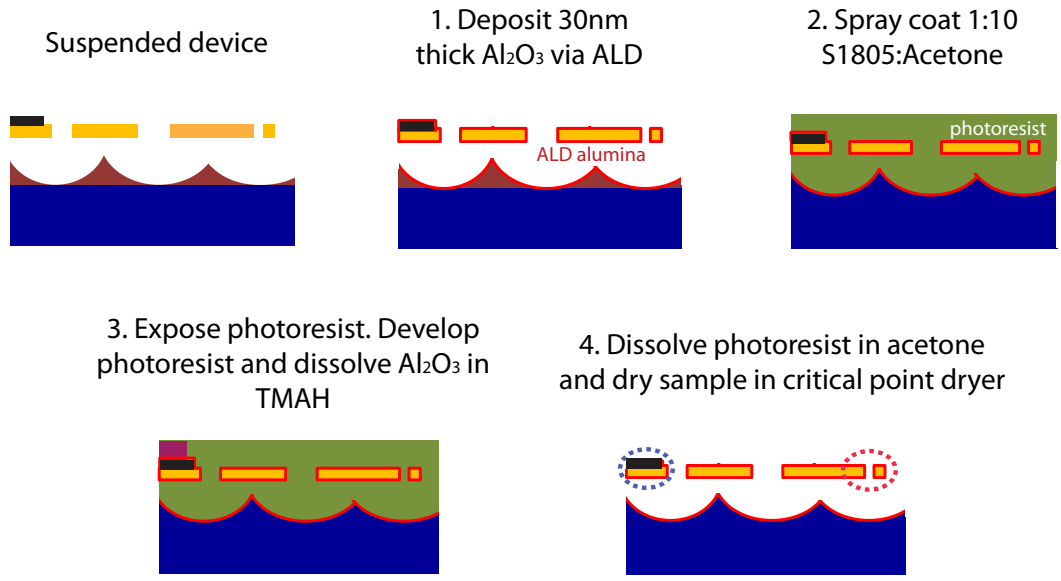

Figure 4.14: Illustration of fabrication process flow on suspended silicon resonators to incorporate ALD for reducing the resonator-electrode gap. The blue ellipse in step 4 highlights the removal of ALD material from the bond pads, and the red ellipse highlights the reduced air gap.

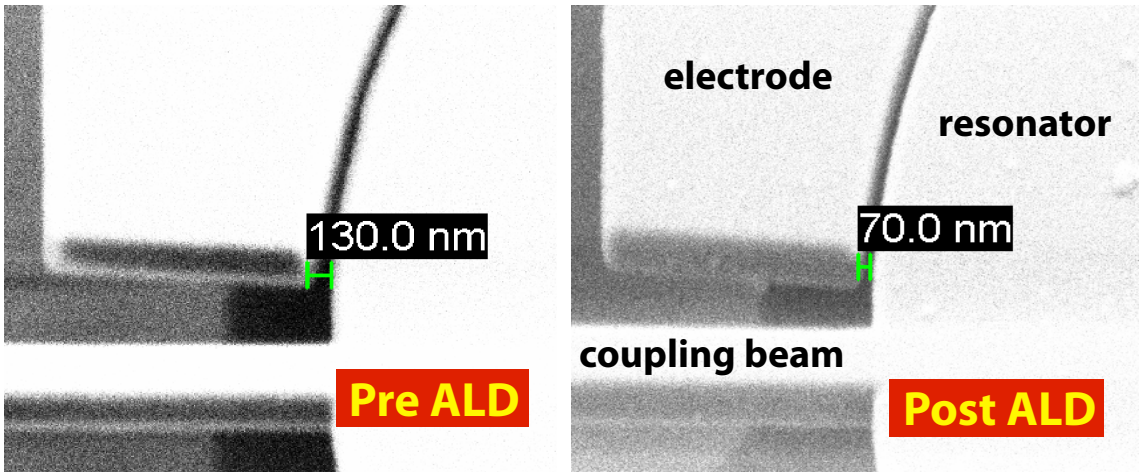

Figure 4.15: SEM highlighting reduction of the resonator-electrode gap from 130nm to 70nm after depositing alumina. Particles seen on the resonator are on account of ALD non-uniformity.

tered at large rotation speeds on the order of thousands of rotations per minute (RPM). By precisely controlling the amount of photoresist sprayed on to the structure, repeated spray steps can be employed to obtain a uniform, thick photoresist coating to protect the device for further photolithography steps.

Spray coating involves the formation of a resist film via millions of μm-sized resist droplets moving towards the substrate. Each technology for droplet generation requires a certain low resist viscosity of usually a few cSt. To put this number in perspective, it is helpful to note that water at 20°C has a kinematic viscosity of 1cSt. Varying the resist viscosity impacts the droplet generation rate as well as the droplet diameter distribution. When diluting resists with a solvent, one has to consider possible incompatibilities of certain solvents with the resist, as well as the fact that highly diluted photoresists generally reveal an accelerated ageing of the resist in the diluted state with particle formation as a consequence. Moreover, the solvent also evaporates during flight and it affects the resist viscosity landing on the sample. Thus, there are many parameters that need to be optimized while developing a recipe for resist spray coating. A common procedure employed to reduce the size of the variable space to be optimized is to modify an existing well-developed spray coating recipe to suit the requirements of the problem at hand. Since the released structures we wish to cover with photoresist have an undercut of $\approx 2\mu$m, the resist film thickness deposited in a single spray coating step should be much smaller than a micron to prevent stiction and damage to the suspended structures. Repeated spray coating should be performed to obtain a thick resist film with thickness $>3\mu$m to obtain a robust film that can withstand contact stresses experienced during contact photo-lithography. Figures 4.16 (a) and (b) show photographs of a chip with released devices, and one such coupled-resonator array respectively spray coated with photoresist.

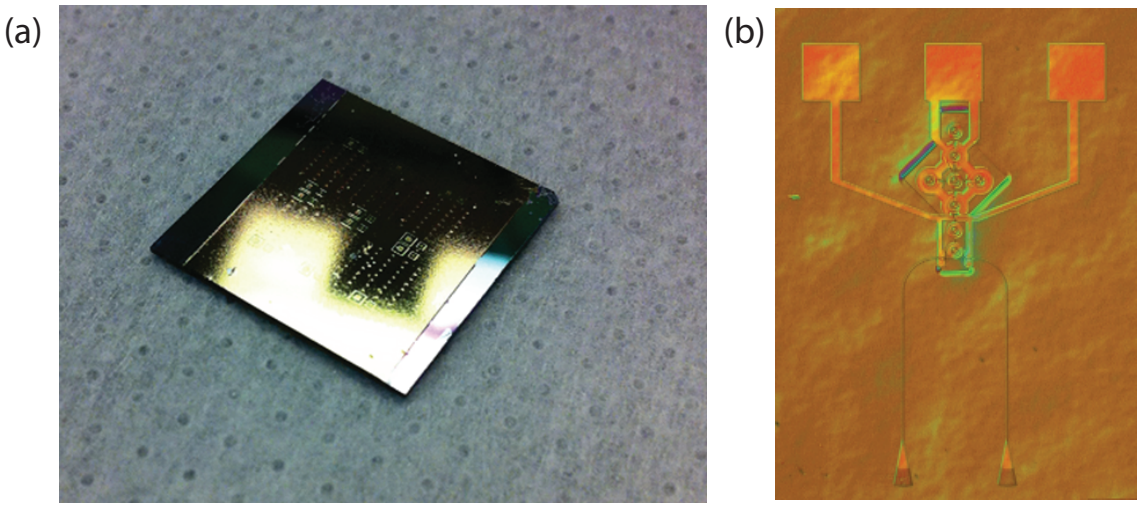

Figure 4.16: (a) Photograph of a 2cm x 2cm chip spray coated with photoresist. The rough texture seen in the photograph results from the resist being sprayed as a colloidal mixture. (b) Optical micrograph of the released opto-mechanical resonator array spray-coated with photoresist.

4.7 2GHz Opto-Acoustic Oscillator

This section explores two innovations to the two coupled-ring resonator design to realize a high frequency opto-acoustic oscillator. The first innovation is to use the micro-mechanical displacement amplifier design to achieve larger optical modulation. The second innovation is to use the partial air gap capacitive transduction scheme via ALD alumina to enhance the electromechanical transduction efficiency at higher frequencies. We incorporate both these ideas into the resonator design to demonstrate an electrostatically actuated silicon OAO operating at 2.05GHz. The following sections provide details on the experimental setup and characterization of the oscillation signal, along with comprehensive understanding of the noise mechanism in this oscillator.

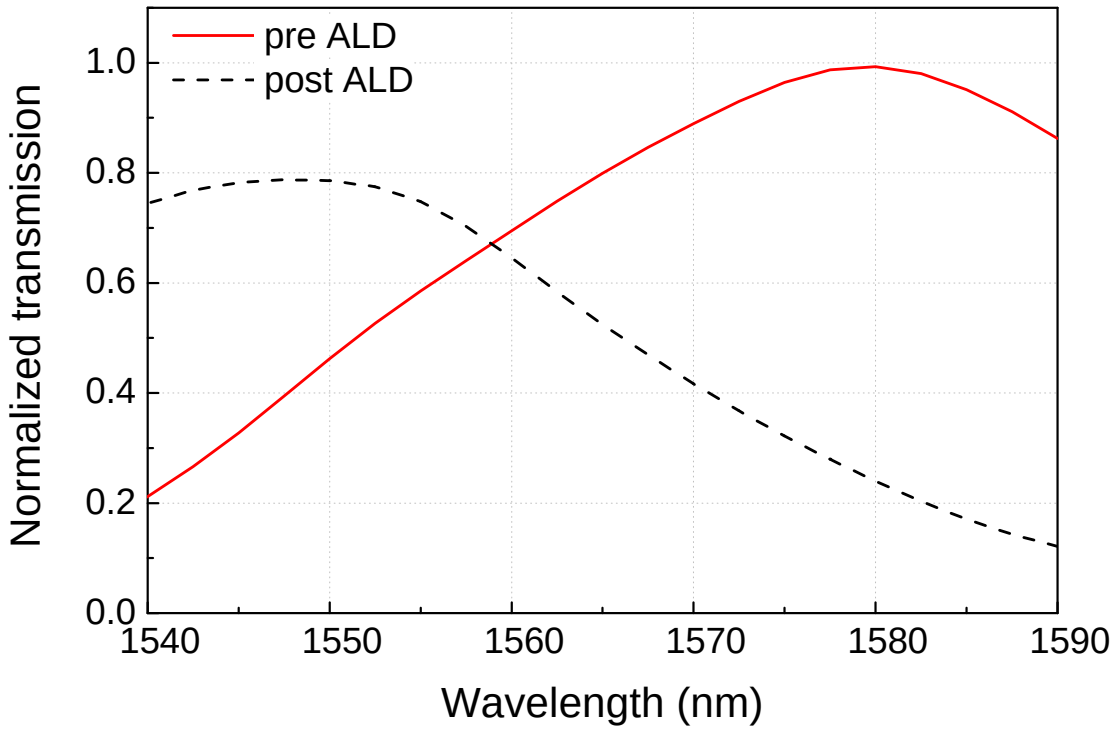

Figure 4.17: FDTD simulated comparison of grating coupler performance prior to and post the ALD deposition step. The intensities are normalized to the highest transmitted optical power post ALD at 1580nm.

4.7.1 Post ALD electro-mechanical characterization

The performance of the grating couplers is simulated with the ALD coating atop the device. Figure 4.17 shows a boost in the grating transmission simulated using Lumerical FDTD (see section 3.3 for details).

Figure 4.18 shows the measured enhancment in the optical performance for the modulator post ALD. The grating transmission is boosted by 3dB, and the half-width-at-half-maximum bandwidth of the gratings increases from 15nm to 20nm. We choose a high optical loaded quality factor (Q_{tot}) resonance at 1574nm shown in Figure 4.19.

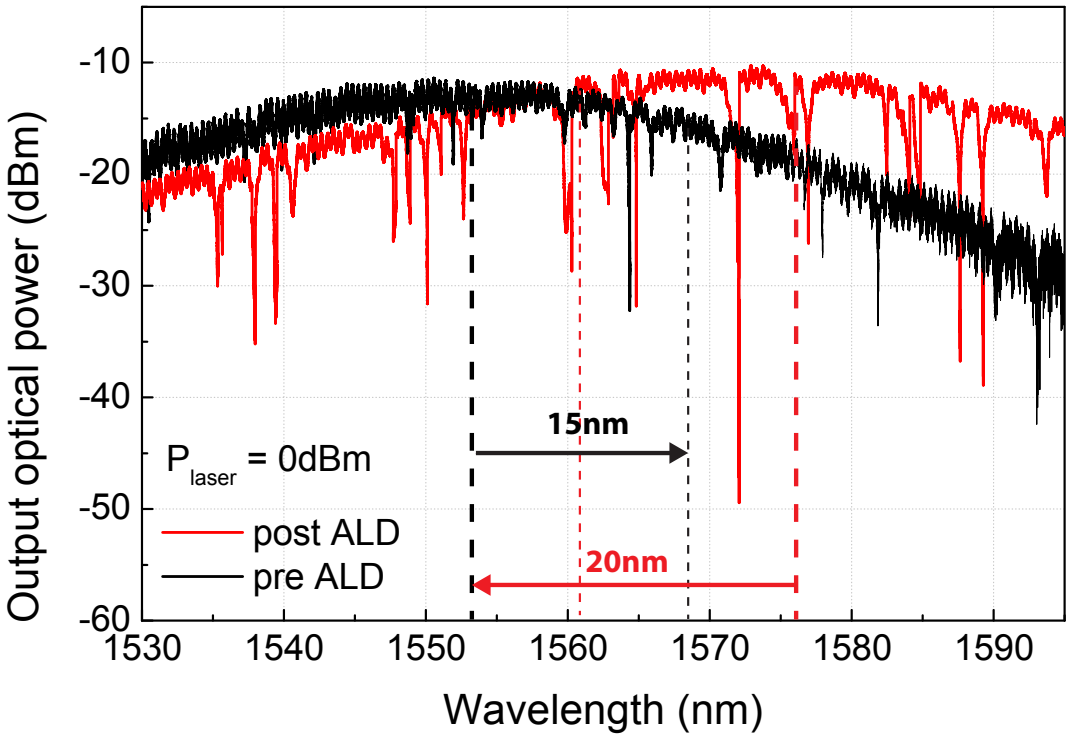

Figure 4.18: Optical transmission spectrum highlighting increase in grating transmission and bandwidth post ALD. The half-width-at-half-maximum bandwidth for the grating couplers increases from 15nm to 20nm.

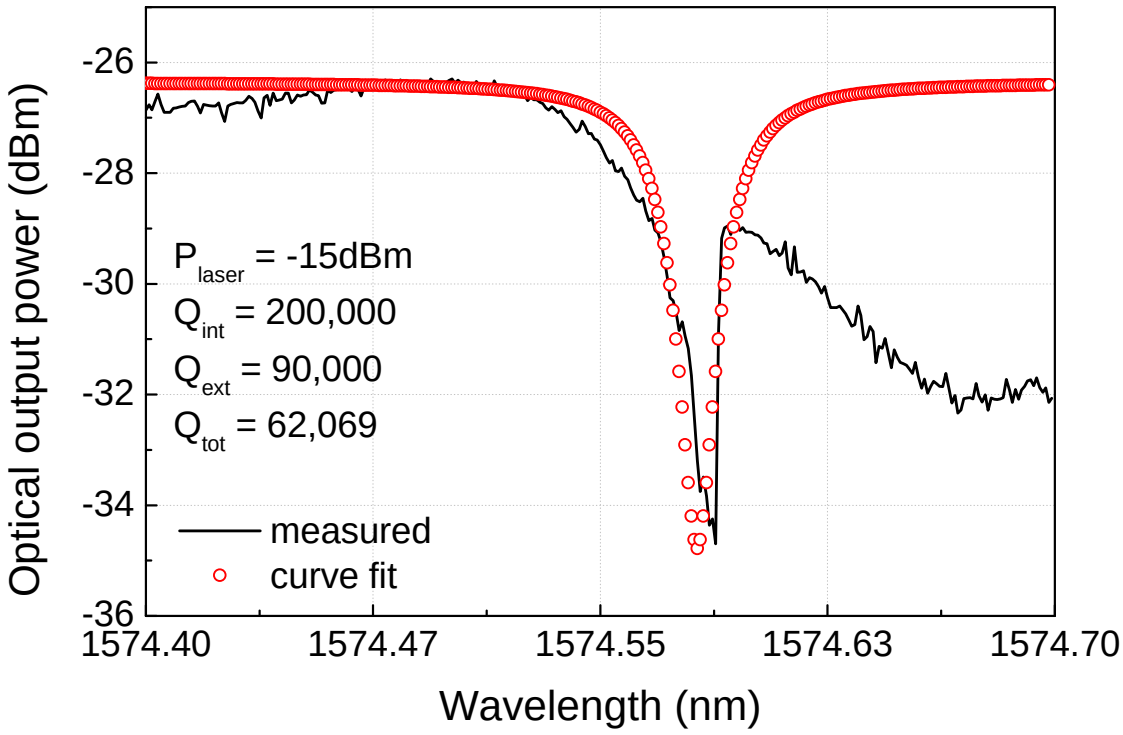

Figure 4.19: High optical Q resonance for the device coated with 30nm alumina. The total (loaded) optical quality factor of the cavity is ≈62,000. The laser power is set to -15dBm.

Figure 4.20 shows a comparison for the transmission of the modulator measured prior to and post the ALD fabrication step. The signal boost at higher frequencies is clear and the enhancement is most prominent for the mechanical mode with frequency 2.1GHz, which shows 5 orders of magnitude improvement in insertion loss (-88dB pre ALD; -41dB post ALD).

Mass loading of the resonator and the coupling beams due to ALD, in addition to acoustic velocity mismatch between silicon and alumina results in degradation of the mechanical Q from 2,300 prior to ALD to 800 post ALD. The large boost in signal power is attributable to 5dB boost in optical power (see Figures 4.4 (b) and 4.19) and reduction in the motional resistance from 1.1MΩ pre ALD to 307kΩ post ALD (see equation D.23 (11dB reduction). Figure 4.21 shows typical improvements in insertion loss at 2GHz recorded for 5 devices. The average improvement for devices in these measurements is obtained to be 30dB.

The large improvement for device 3 is explained by the impact of the ALD on the resonator radius and the beam length. The coupling beam length is designed to be $3\lambda_a/2$, where λ_a denotes the acoustic wavelength for the radial expansion mode at 1.1GHz. Fabrication variations across the chip could result in deviations on the order of the electron beam spot size used in the e-beam lithography step (≈20-30nm at 5nA beam current) from this ideal value. A half-wavelength coupler has infinite stiffness and causes no mass loading on the resonator. Deviation from this length results in the coupler introducing mechanical dissipation in addition to frequency splitting in the modes of vibrations of the rings [75], as shown in Figure 4.22. With multiple rings coupled in a strongly coupled array, the mismatch is more pronounced, as different rings experience dissimilar loading from the springs. Depositing ALD alumina on the device results in increasing the radius of the rings,

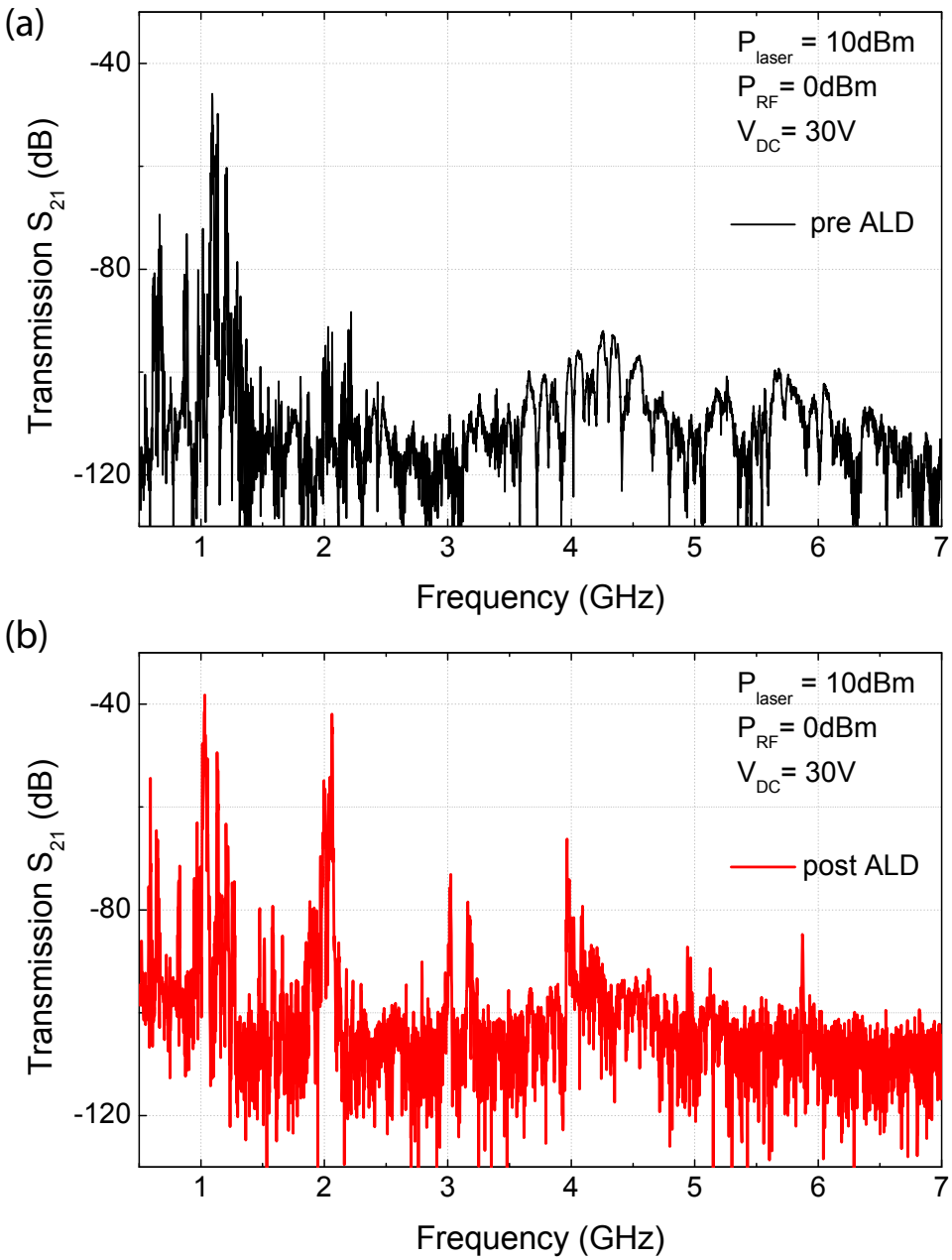

Figure 4.20: Comparison of the modulator transmission spectrum (a) pre ALD and (b) post ALD. The most pronounced transduction enhancement is recorded at 2.05GHz (47dB improvement).

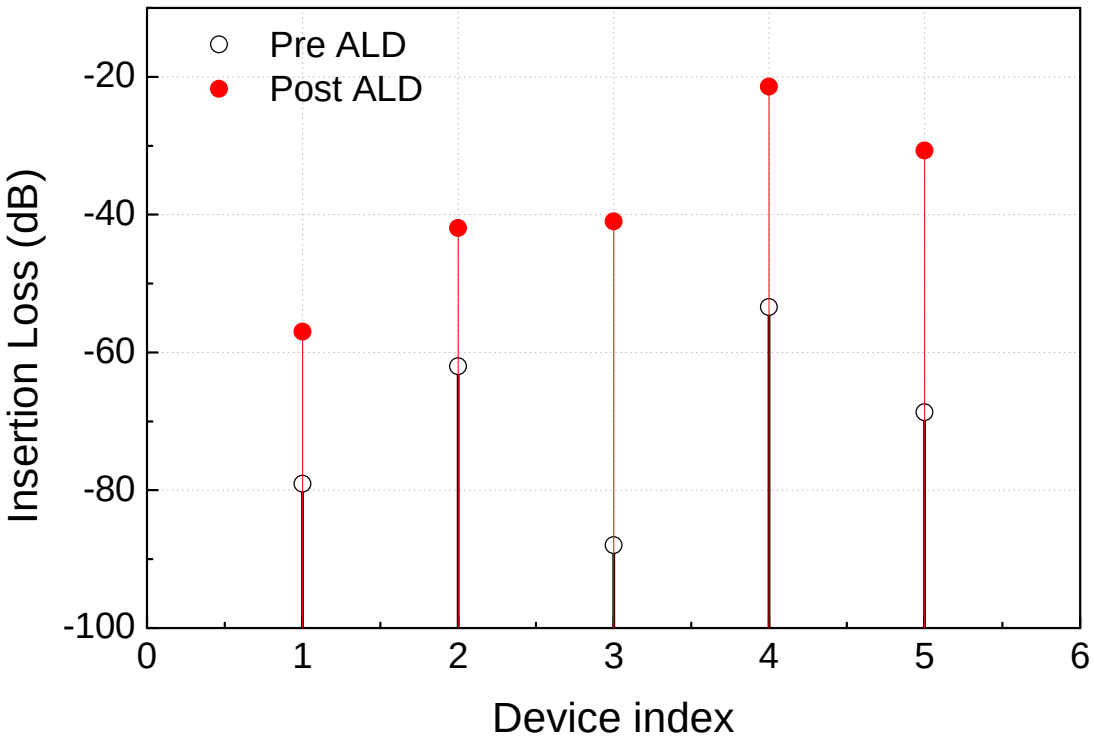

Figure 4.21: Typical improvement in insertion loss at 2GHz recorded for 5 devices pre and post ALD. The average improvement in these measurements is obtained to be 30dB. Pre and post ALD measurements on each were performed using comparable optical quality factors. The laser power in each measurement was set to 15dBm, and a combination of 30V DC and 0dBm RF power was applied at the electrode.

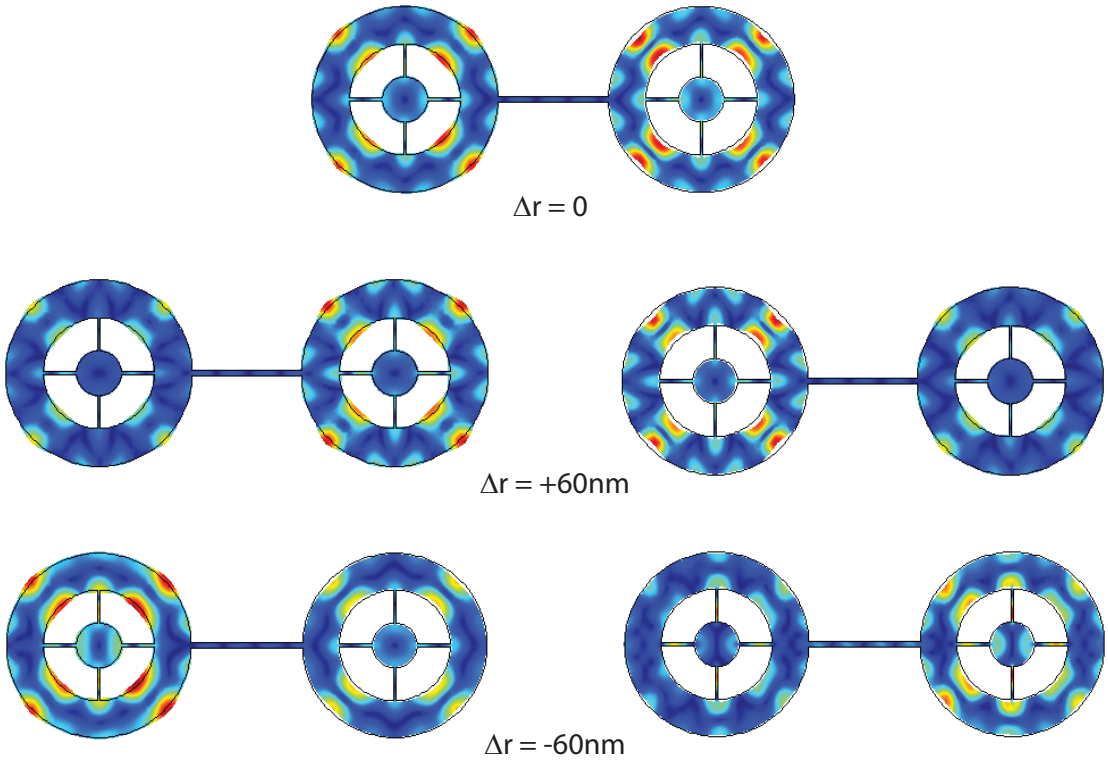

Figure 4.22: FEM simulations highlighting the frequency splitting introduced by changing the resonator radius by ±60nm.The rings have identical displacement amplitudes when the beam length is an odd multiple of $\lambda_a/2$. When the beam length deviates from the ideal value, the displacement amplitudes in both ring resonators are dissimilar, which translates to impaired transduction and lower quality factor.

thereby reducing the mechanical resonance frequency. Simultaneously the beam length reduces as the ring radius increases, which increases the resonance frequency of the coupling beam. Thus, designs with initially unmatched ring and coupling spring resonance frequencies could be tuned to ideal dimensions via ALD alumina deposition. This results in the large enhancement in insertion loss recorded for device 3.

To select the second order compound radial expansion mode at 2.05GHz and

suppress the other mechanical modes of the device, we use a band-pass filter (Mini-circuits VBFZ-2000-S+). Figure 4.23 shows the RF transmission spectrum measured by introducing the filter at frequencies near 2.05GHz. The spectrum shows 8 prominent peaks that arise from the 8-fold symmetry of the mutually coupled rings in the device vibrating in the second order compound radial expansion mode (Figure 4.23 inset). The other spurious peaks are attributed to imperfections in the beam lengths due to fabrication variations. The tallest peak at 2.047GHz corresponds to the mechanical mode with best momentum balance. The second tallest peak at 2.067GHz has a frequency separation of 20MHz from this mode and has 8dB larger insertion loss. Since the oscillator loop locks to a single mechanical mode, an oscillator operating at 2.047GHz will not be affected by the other mechanical modes.

4.7.2 Delay line oscillator design

The mechanical resonator can be operated as an oscillator in a closed feedback loop. The condition required for oscillation is set by the Barkhausen criterion, that requires an overall loop gain of unity, and the phase around the loop an integral multiple of 2π at the oscillation frequency. To overcome transmission losses in the opto-mechanical resonator, an amplifier is required that provides unity gain for the open loop. The other condition is ensured by either choosing an appropriate feedback circuit or using a phase shifting circuit. A typical electronic circuit to obtain oscillators using mechanical resonators is the Pierce oscillator circuit which consists of a transistor to provide the gain and a combination of capacitors in feedback for the phase. We operate the 2.05GHz mechanical resonance in a feedback loop using an amplifier (Mini-circuits ZQL-2700MLNW+) and a phase shifter us-

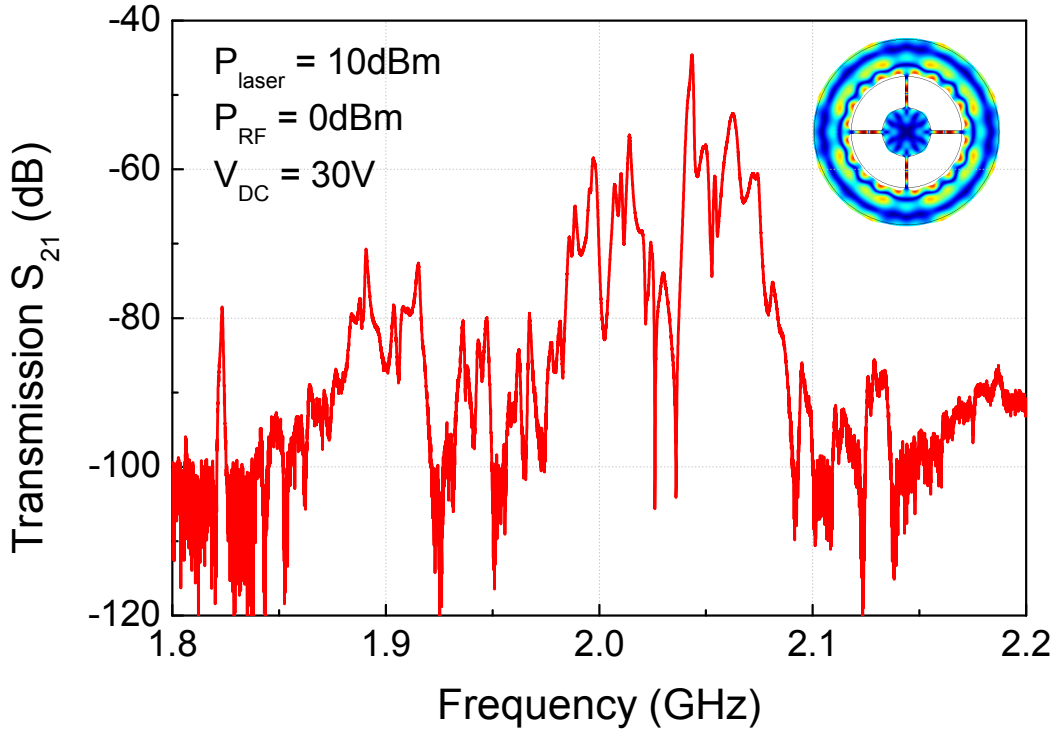

Figure 4.23: Transmission spectrum of the device measured with the introduction of a band-pass filter to select mechanical modes around 2GHz. Inset: Finite Element Method (FEM) simulated mechanical resonance mode shape at 2.047GHz.

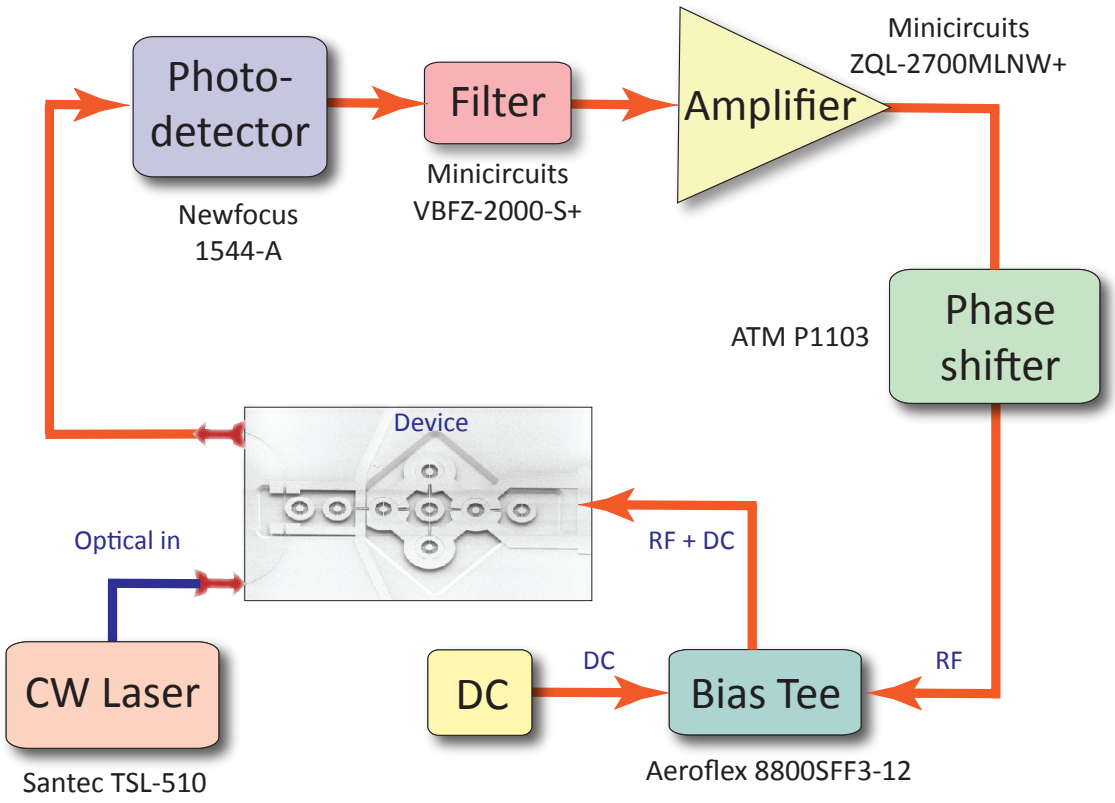

Figure 4.24: Schematic of the delay line oscillation loop.

ing the oscillator topology outlined in [11]. Figure 4.24 shows a schematic of the oscillator feedback loop.

4.7.3 Oscillation phase noise

Figure 4.25 shows the RF spectrum and phase noise of the oscillations at 2.05GHz. The oscillation signal phase noise at 10kHz offset from carrier is -80dBc/Hz. We measure the phase noise using an Agilent 5052B signal source analyzer. Using a low noise amplifier results in lack of $1/f^3$ slopes down to 5kHz offset from carrier in the phase noise plot unlike [11].

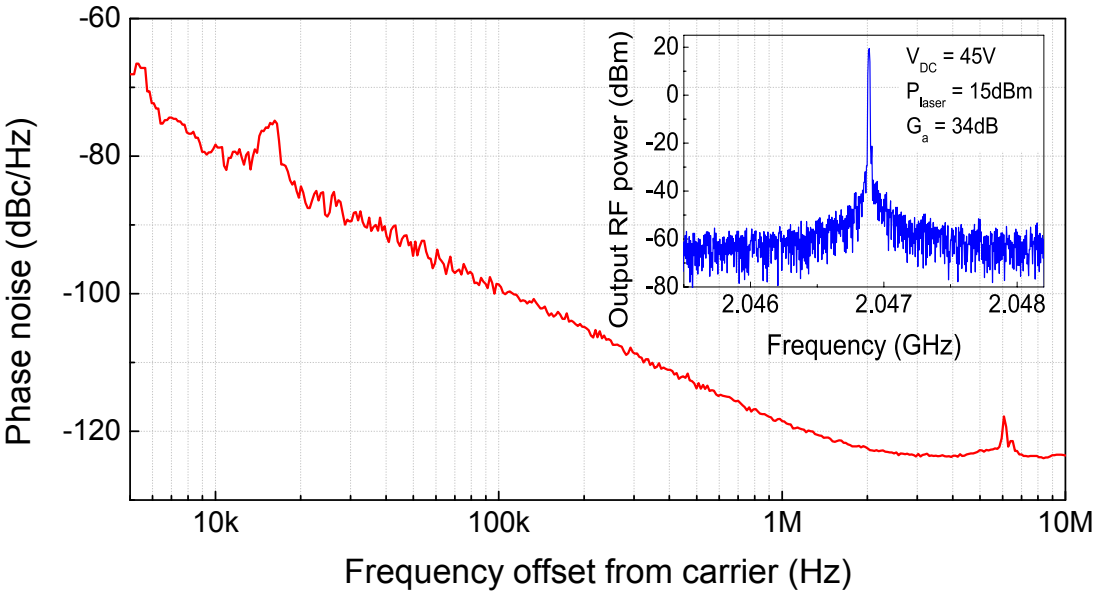

Figure 4.25: Phase noise of the oscillations at 2.05GHz, with 80dBc/Hz noise at 10kHz offset from carrier. Inset: RF spectrum of oscillations at 2.05GHz. The phase noise is measured using an Agilent 5052B signal source analyzer.

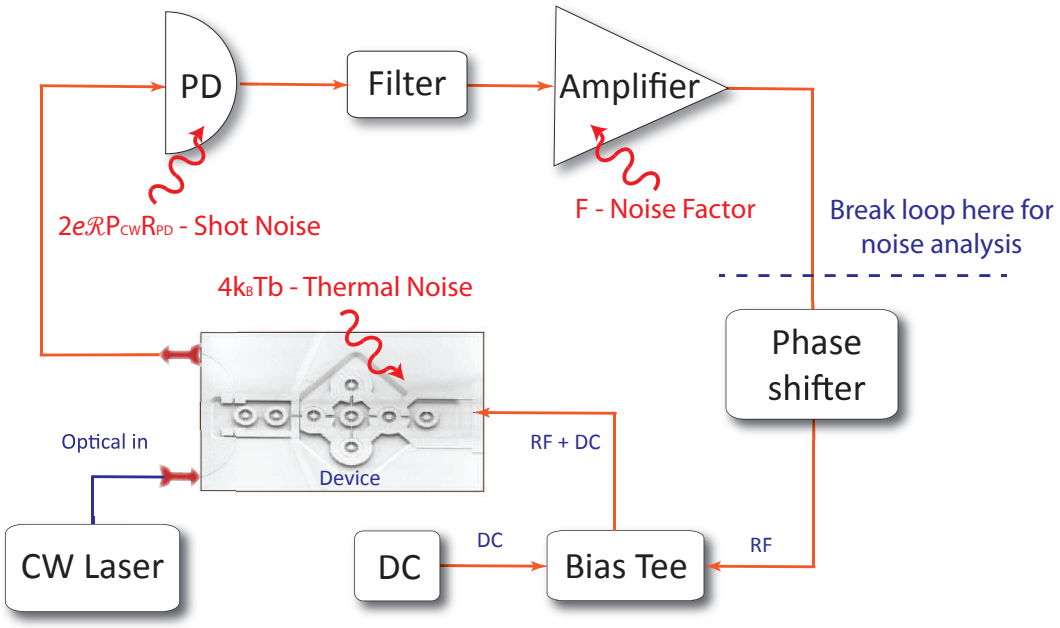

Figure 4.26: Schematic of the OAO loop highlighting the primary noise sources.

4.7.4 Phase noise model for opto-acoustic oscillators

To model the phase noise of the OAO, we follow a methodology similar to conventional noise analysis in PLL systems [76] and optoelectronic oscillators [77]. The fundamental noise contributions in the OAO arise primarily from the thermal noise, the photodetector shot noise, noise contributed by the amplifier, and the laser's intensity noise. Consider the noise loop shown in Figure 4.26. For the sake of noise analysis, we can break the loop and write down an expression for the noise-to-signal ratio at the output of the amplifier.

The power spectral density of the Brownian motion can be written as in equation 4.3 as follows:

$$S_x\left(\Omega_{mech}\right) = \sqrt{\frac{4k_BTQ_{mech}}{m_{eff}\Omega_{mech}^3}} \tag{4.3}$$

where k_B is the Boltzman constant, T is the ambient temperature, and Q_{mech}, m_{eff} and Ω_{mech} are the quality factor, effective mass and frequency of the mechanical resonance respectively.

The motion of the cavity leads to modulation of the transmitted optical power at the output of the device, $\sqrt{\langle P_{mod}^2 \rangle} = \frac{dT}{dr} P_{CW} S_x\left(\Omega_{mech}\right)$. The scale factor, $\frac{dT}{dr}$, denotes the change in optical transmission (T) with radial displacement (r). Note that we can express $\frac{dT}{dr}$ in terms of the opto-mechanical coupling coefficient, g_{OM} as $\frac{dT}{dr} = \frac{dT}{d\omega_0}\frac{d\omega_0}{dr} = H_{opt} g_{OM}$. H_{opt} is the cavity transfer function expressed as in equation 4.4[32]:

$$H_{opt} = \sqrt{\frac{4\Gamma_{ext}^2\Gamma_{int}^2\Delta_0^2}{\left[\Delta_0^2 + \left(\frac{\Gamma_{tot}}{2}\right)^2\right]^4}} \tag{4.4}$$

where $\Delta_0 = \omega_0 - \omega_p$ is the static detuning of the laser frequency (ω_p) with respect to the optical cavity resonance frequency (ω_0), Γ_{ext} is the decay rate associated with coupling of photons to the optical cavity, and Γ_{int} and Γ_{tot} are the intrinsic and loaded cavity photon decay rates respectively.

The power noise spectral density at the output of the photodetector can then be expressed as follows:

$$\sqrt{\left\langle P_{n,PD_{out}}^2 \right\rangle} = \sqrt{\langle P_{mod}^2 \rangle} G_{PD}^2 = H_{opt} g_{OM} P_{CW} S_x\left(\Omega_{mech}\right) G_{PD}^2 \tag{4.5}$$

The noise spectral density at the input terminal of the amplifier can then be written down as (in units of $V^2/\sqrt{Hz}$):

$$\rho_{n,in} = S_x\left(\Omega_{mech}\right) H_{opt} P_{CW} g_{OM} G_{PD}^2 + 2e\Psi P_{CW} R_{PD} + N_{RIN} I_{ph}^2 R_{PD} \tag{4.6}$$

The first term in the RHS is the thermal Brownian noise amplified by the photodetector gain (G_{PD}). The second and third terms are the detector shot noise and the laser's intensity noise respectively. For benchtop tunable lasers, the intensity noise is negligibly small compared to the thermal noise and the shot noise and can be safely ignored. The optical power at the input of the photodetector is denoted by P_{CW}, Ψ is the responsivity of the photodetector, $I_{ph} = \Psi P_{CW}$ is the photocurrent across the load resistor of the photodetector, R_{PD}, and N_{RIN} is the relative intensity noise (RIN) of the input laser. The noise at the output of the amplifier can then be expressed in terms of the noise factor (F) and the gain (G_A) as $\rho_{n,out} = F\rho_{n,out} G_A^2$. This gives the following expression for noise-to-signal ratio at the output of the amplifier:

$$\delta = \frac{\rho_{n,out}}{P_{sig}} \tag{4.7}$$

Following the derivation in [77], the full width at half maximum (FWHM) linewidth of the oscillation signal is then obtained as:

$$\Delta f_{FWHM} = \frac{\delta}{2\pi\tau^2} \tag{4.8}$$

where $\tau = \frac{2Q_{mech}}{\Omega_{mech}} + \frac{2Q_{opt}}{\omega_p}$ is the delay in the oscillation loop, due to circulation of photons inside the optical cavity $\left(\frac{2Q_{opt}}{\omega_p}\right)$ and the filter response of the mechanical resonance $\left(\frac{2Q_{mech}}{\Omega_{mech}}\right)$. With an expression for the oscillation linewidth in place, we can model the phase noise [34] for the OAO as below:

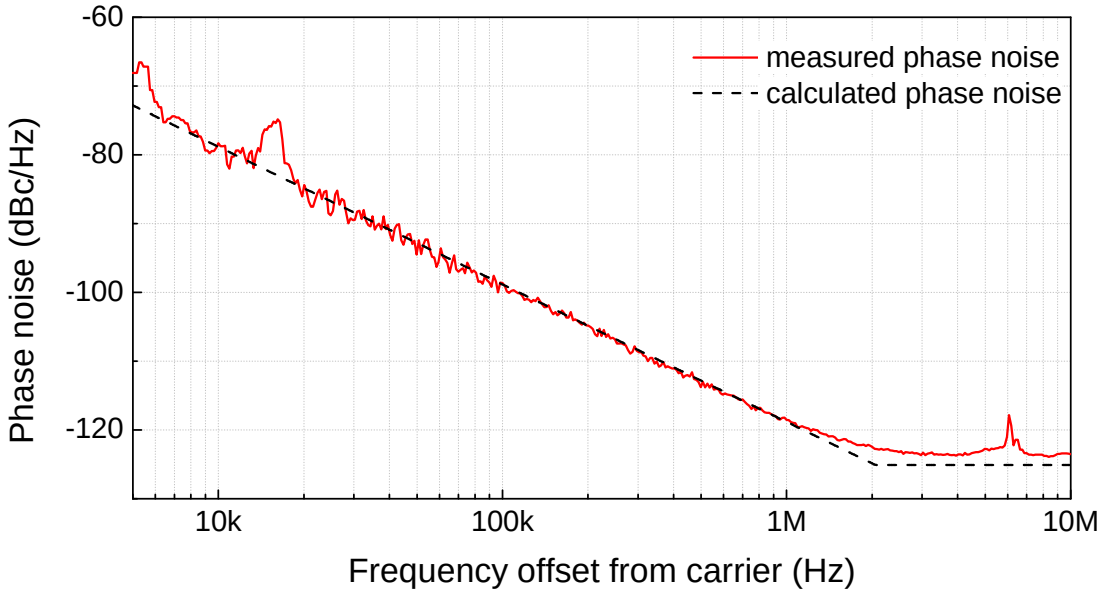

Figure 4.27: Comparison of measured phase noise for oscillation signal at 2.05GHz to phase noise calculated using the model presented here.

$$
\begin{aligned}
L(\Delta f) &= 10log_{10}\left(\frac{1}{\pi}\frac{\Delta f_{FWHM}}{(\Delta f_{FWHM})^2+(\Delta f)^2}\frac{f_3}{\Delta f}\right)\ldots\frac{1}{f^3}regime \\
&= 10log_{10}\left(\frac{1}{\pi}\frac{\Delta f_{FWHM}}{(\Delta f_{FWHM})^2+(\Delta f)^2}\right)\ldots\frac{1}{f^2}regime \\
&= 10log_{10}\left(\frac{1}{\pi}\frac{\Delta f_{FWHM}}{(\Delta f_{FWHM})^2+(f_0)^2}\right)\ldots noisefloor \quad (4.9)
\end{aligned}
$$

where f_3 is the corner frequency for $\frac{1}{f^3}$ noise in the phase noise spectrum, and $f_0 = f_{mech}/2Q_{mech}$ is the Leeson corner frequency for the oscillator. The comparison of the phase noise calculated using this model to measured phase noise is shown in Figure 4.27.

The Newfocus 1544-A photoreceiver used in the experiments reported in earlier sections has a Noise Equivalent Power (NEP) of 24pW/$\sqrt{Hz}$. The dominant contribution to the noise spectral density in equation 4.6 comes from the shot noise in the photodetector. To design an oscillator with lower phase noise, we need to use a

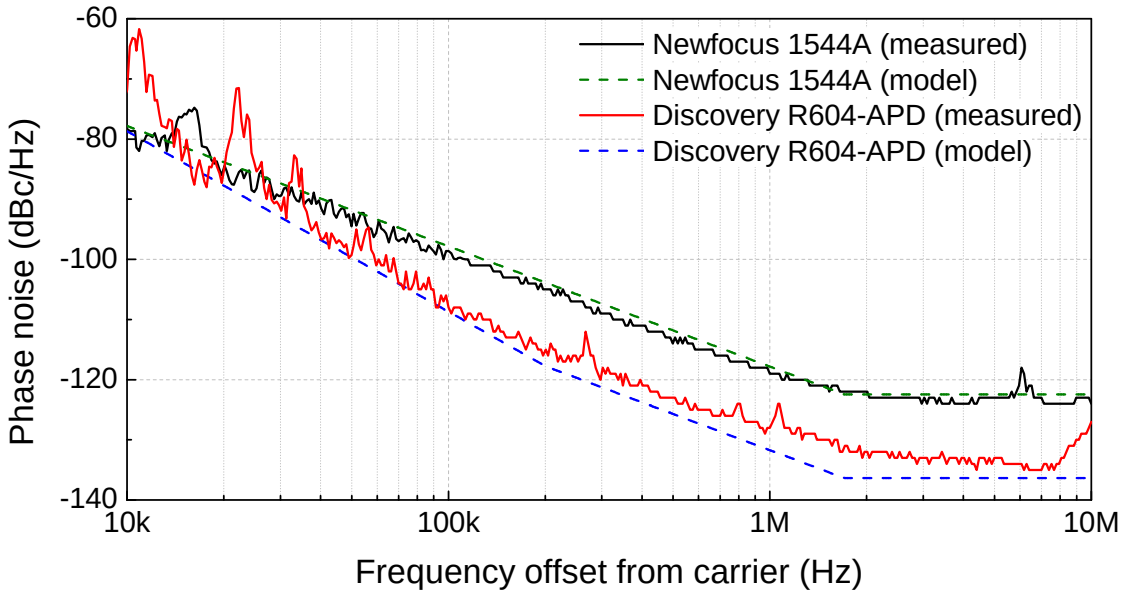

Figure 4.28: Comparison of measured phase noise for oscillation signal at 2.05GHz to phase noise calculated using the model presented here. The black curve is the phase noise recorded using a New-Focus 1544A photoreceiver and the red curve is obtained using a Discovery Semiconductors R604-APD avalanche photodetector. The green and blue dashed curves are the calculated phase noise performance using the phase noise model. The model clearly fits well to the measured phase noise numbers.

photoreceiver with a lower NEP. Also, it is desirable to have a large gain and an RF bandwidth >2GHz for the photoreceiver. The R604-APD avalanche photodetector manufactured by Discovery Semiconductors provides a single ended conversion gain of 12,000V/W and a 3-dB bandwidth of 7GHz, with an NEP <2.4pW/$\sqrt{Hz}$. Using this photoreceiver, we obtain a phase noise floor of -137dBc/Hz as seen in Figure 4.28. However, to provide sufficient gain in the feedback loop, we have to use an additional amplifier (Minicircuits ZRL-2400LN, alongwith a 20dB attenuator to avoid gain saturation in the amplifier chain), which shifts the $1/f^3$ corner frequency to ≈200kHz.

The RF signal generated by the photodetector depends on the detuning of the

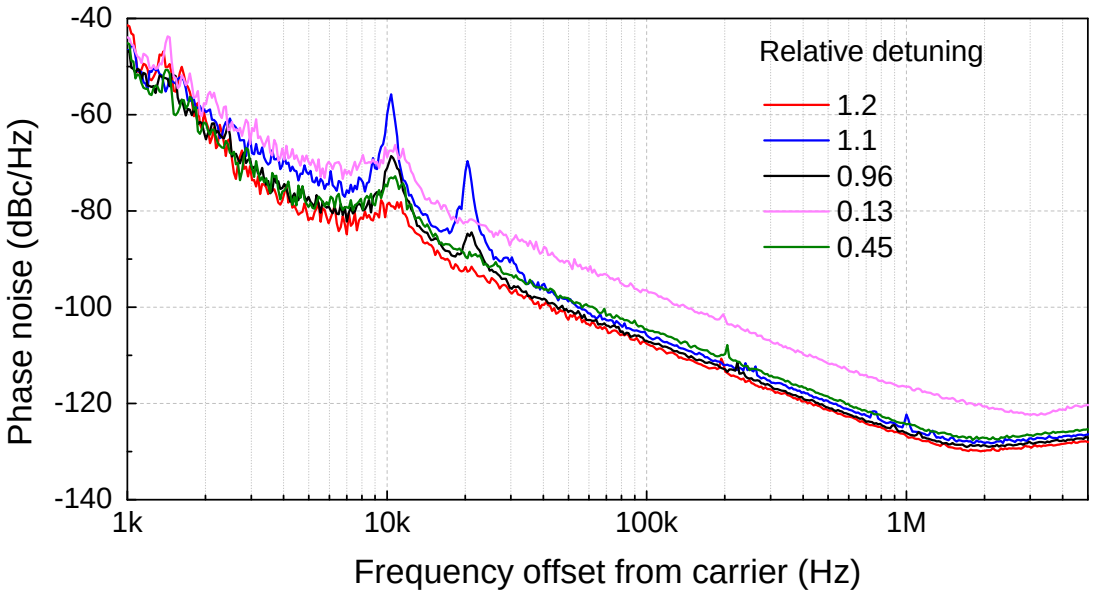

Figure 4.29: Variation of phase noise for the oscillation signal at 2.05GHz for various relative detuning values. A DC voltage of 35V was used to operate the oscillator.

laser wavelength from the cavity optical resonance wavelength. As a result, the phase noise of the oscillation signal also varies with the detuning, as captured in equation 4.4. Figure 4.29 shows phase noise spectra for the oscillator recorded at various relative detuning values measured using the R604-APD photoreceiver. Relative detuning is defined as $\frac{\Delta_0}{2\delta}$, where $\Delta_0 = \omega_0 - \omega_p$ is the detuning of the pump laser frequency ω_p from the cavity optical resonance frequency ω_0, and δ is the full-width-at-half-maximum (FWHM) linewidth of the cavity optical resonance. Figure 4.30 compares the measured phase noise at 100kHz offset from the carrier with the calculated value of phase noise based on the model presented here. The measured trend in phase noise agrees well with the calculated trend, and we conclude that it is desirable to choose a relative detuning value $\approx$1 for the best phase noise performance.

Another interesting observation from equation 4.8 is that increasing the total

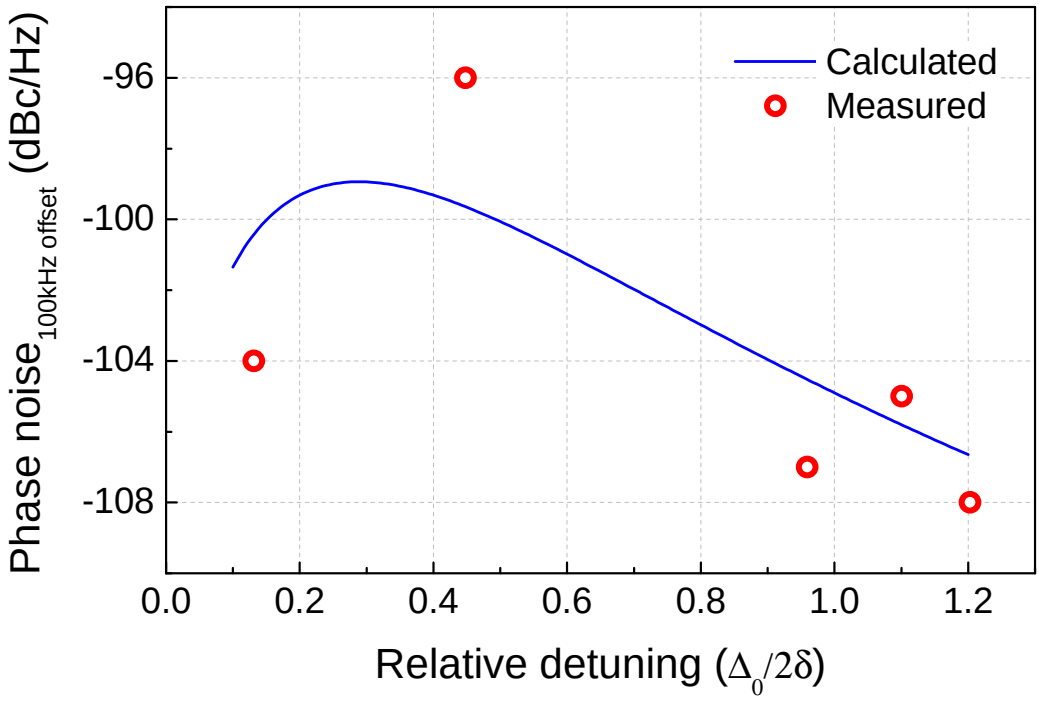

Figure 4.30: Phase noise at 100kHz offset from carrier measured for various relative detuning values. The measured trend in the phase noise variation agrees with the calculated trend based on the phase noise model.

delay in the loop will lead to reduced linewidth and hence lower phase noise. Improving the mechanical Q is akin to adding more acoustic delay in the loop. Optical delay can be introduced by increasing the optical Q. However, a mechanical Q of 1,000 at 1GHz translates to a mechanical delay of 2μs. An optical Q of 100,000 at 1,550nm (193.5THz) corresponds to an optical delay of 0.5ns. To get an optical delay comparable to the mechanical delay, the optical Q has to be on the order of 1 billion, which is not easy to achieve in chip scale silicon photonic resonators. Off-chip delay can be introduced by integrating an optical fiber spool in the loop. A 5km long fiber corresponds to an optical delay of $\frac{5km}{3e8m/s} = 16.6\mu$s. Figure 4.31 shows 35dB reduction in the close-to-carrier phase noise of the opto-acoustic oscillator achieved by introducing this fiber spool. However, this increases the cavity length of the oscillator, making the cavity mode spacing smaller than the bandwidth of the intracavity mechanical RF filter. This results in generation of spurs in the output of the oscillation signals [78] as seen in the phase noise plot in Figure 4.31.

4.7.5 Phase noise of oscillation harmonics

The optical resonance shape is Lorentzian, and therefore opto-mechanical modulation is inherently non-linear as described earlier in section 2.4. When the motion of the opto-mechanical resonator exhibits oscillations at 2.05GHz, the non-linear modulation results in generation of multiple harmonics of the fundamental oscillation frequency, as seen in Figure 4.32. The signals at these frequencies are expected to have the same noise signature as the fundamental harmonic at 2.05GHz. The non-linear shape of the optical resonance serves as an ideal frequency multiplier in this case, and hence the noise of all the higher oscillation harmonics of order n are

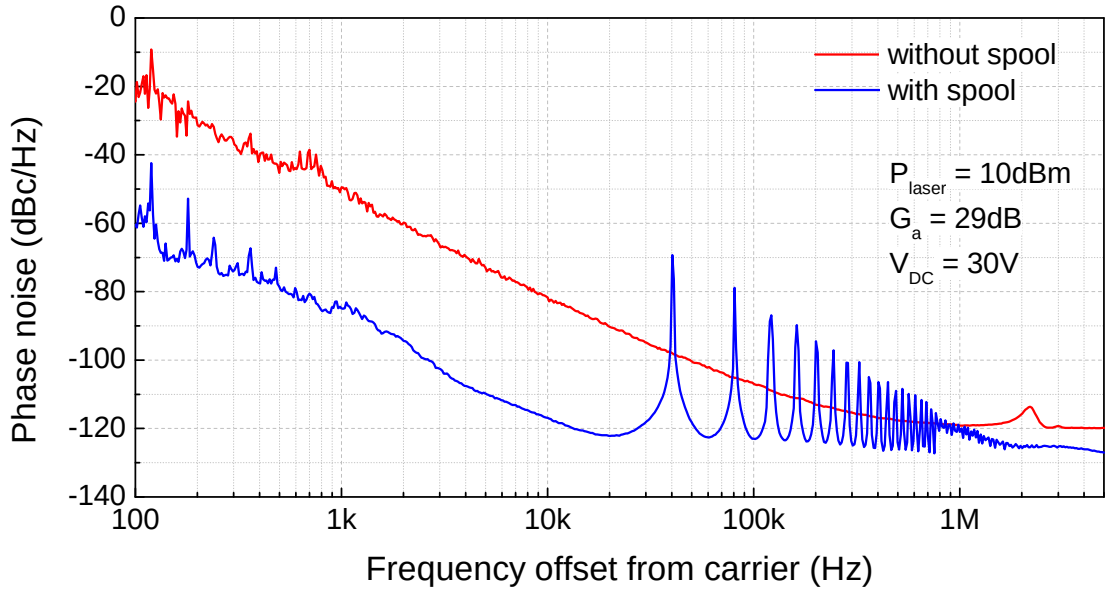

Figure 4.31: Comparison of measured phase noise for oscillation signal at 2.05GHz to phase noise calculated using the model presented here.

expected to be worse than the phase noise of the 2.05GHz signal by $20log_{10}(n)dB$. The phase noise for the 4.1GHz and 6.15GHz signals follows this trend as seen in Figure 4.33. We use band-pass filters to select the oscillation harmonics at 4.1GHz (VBFZ-4000+) and 6.15GHz (VBFZ-6260+) at the input of the Agilent 5052B signal source analyzer.

4.7.6 Comparison to state-of-the-art

A popular figure of merit (FOM) for oscillators summarizes the important performance parameters – phase noise $L(\Delta f)$, oscillator frequency f_{osc} and DC power consumption P_{DC} – to make a fair comparison:

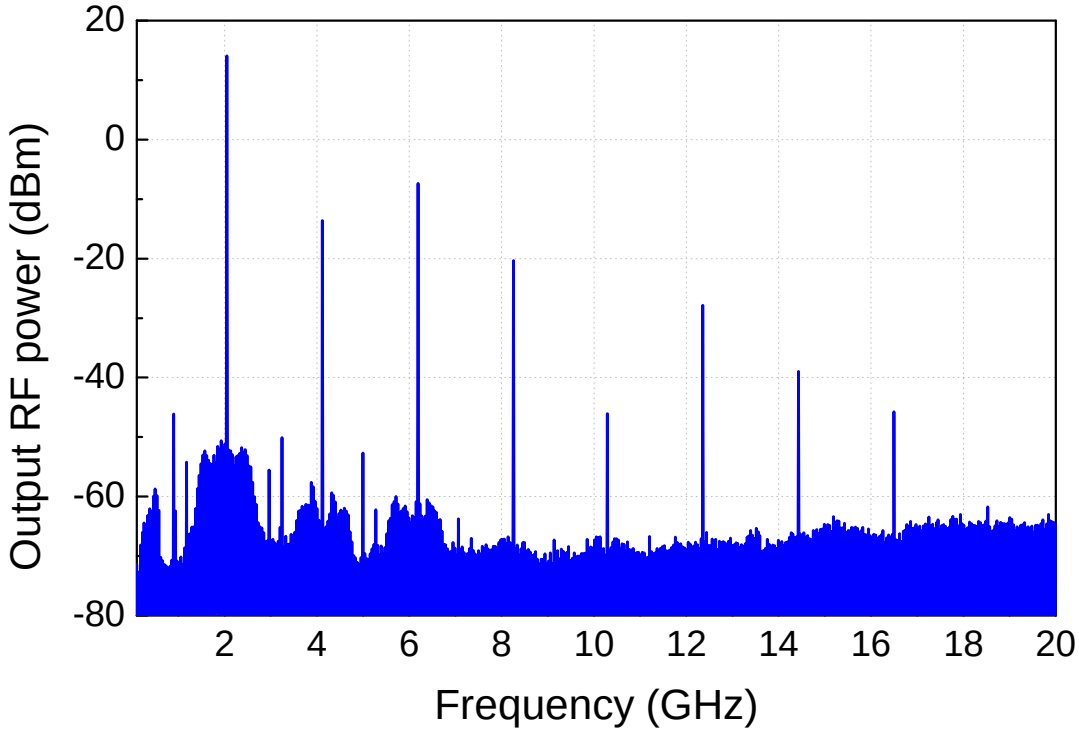

Figure 4.32: Plot showing various harmonics of the fundamental oscillations at 2.05GHz. The signal power at 16.4GHz is measured to be -45dBm.

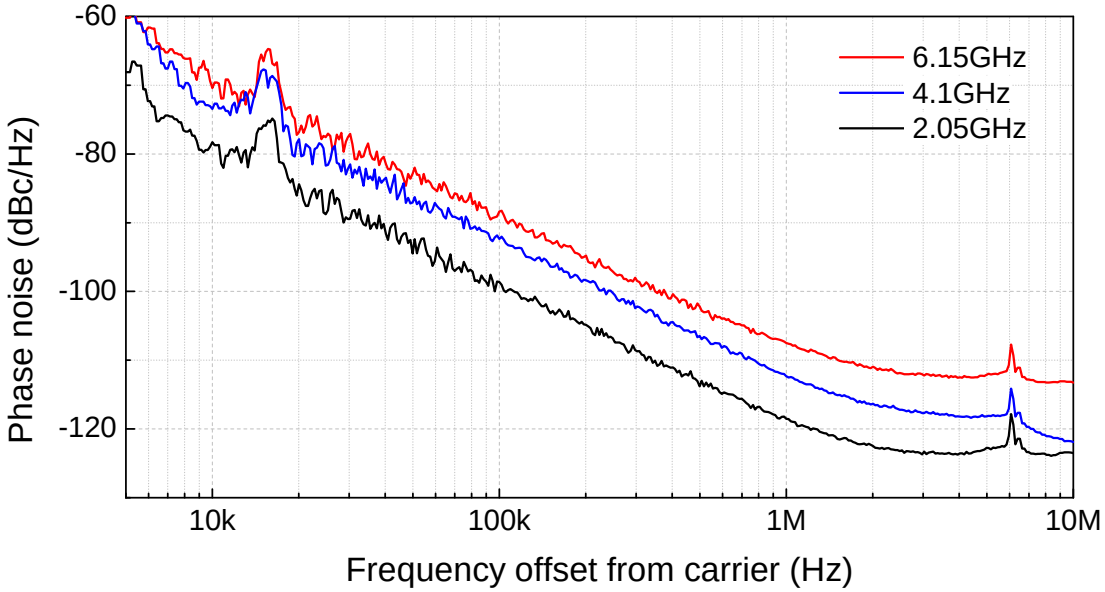

Figure 4.33: Comparison of phase noise of the oscillations at 2.05GHz, 4.1GHz and 6.15GHz. The phase noise for the higher harmonics of order n is worse than the fundamental by 20log(n)dB. The RF oscillation signal power is the same for all curves (-5dBm).

$$FOM = L(\Delta f) + 20log_{10}\left(\frac{\Delta f}{f_{osc}}\right) + 10log_{10}\left(\frac{P_{DC}}{1mW}\right) \tag{4.10}$$

The second term neutralizes the effect of the offset frequency Δf while taking the oscillator frequency into account. P_{DC} is measured in milli-Watts (mW). Table 4.1 compares the performance of the OAO presented here to other state-of-the-art chip-scale oscillator technologies. The phase noise is scaled to an oscillation frequency of 1GHz for a fair comparison. The FOM for our 2.05GHz OAO is completely dominated by the oscillator's DC power consumption. The large power consumption comprises of the laser power consumption (166mW), photodetector (250mW) and RF amplifier (320mW). The Santec TSL-510 laser used in our experiments has a power efficiency of 6%. Low power laser and photodetector development is an active area of research, and power scaling of on-chip lasers and

Table 4.1: Oscillator Figure Of Merit (FOM) comparison

Reference	Oscillation Frequency (GHz)	Technology	Phase noise at 100kHz offset (dBc/Hz)	DC Power Consumption (mW)	FOM (dBc/Hz)
[10]	0.06	MEMS	-135	0.35	-195
[14]	3.4	FBAR	-140	20	-216
[79]	30	OEO	-120	1800	-196
[80]	4.936	CMOS	-102	2	-162
This work	2.05,4.1,6.15	OAO	-110	740	-167

detectors should enable an OAO with FOM on par with state-of-the-art. Even in the current form, the OAO outperforms state-of-the-art in high performance high frequency CMOS oscillators.

Part II

MEMS Aided Photonics Applications

CHAPTER 5

ACOUSTO-OPTIC FREQUENCY MODULATION

Optical frequency modulation has been achieved in microstructures using surface acoustic waves to strain self-assembled InAs/GaAs quantum dots [81]. Photon generation at >GHz frequency spacing from a single pump laser has been realised in silicon nitride and silicon dioxide via nonlinear optical processes such as the optical Kerr effect [82] and stimulated Brillouin scattering [37, 38, 39]. It is difficult to exploit such non-linear optical phenomena in silicon, primarily owing to two-photon absorption that limits optical power handling. Wavelength conversion in silicon has been demonstrated using fundamentally all-optical schemes [83, 84, 85] and via free-carrier plasma dispersion effect [86], making their integration on micro-electronic chips challenging.

We analyzed opto-mechanical modulation in great detail in Chapter 2. Employing this scheme at GHz rates will provide valuable narrow-band acousto-optic modulators for direct conversion of electrical signals to optical intensity modulation that are valuable towards realizing a chip-scale opto-electronic oscillator (OEO) [77]. In addition to intensity modulation, it is desirable to achieve frequency modulation, which adds variable group delay into the optical field, thus potentially boosting phase noise performance of the OEO. This chapter presents an analysis of coincident intensity and frequency modulation in the coupled silicon opto-mechanical resonator. This design can open up avenues towards realizing a truly chip-scale OEO and enable on-chip Dense Wavelength Division Multiplexing (DWDM) using a single input laser. The next section presents the theoretical basis for the operation of this device. The final section covers experimental results obtained using our device.

5.1 A General Treatment of Coincident Amplitude Modulation (AM) and Frequency Modulation (FM)

Consider a sine wave carrier expressed by the general equation below:

$$s(t) = Acos(\omega_c t) \tag{5.1}$$

A is the amplitude and ω_c is the frequency of the carrier signal. When the signal is amplitude-modulated with a modulation index m_{AM} at frequency ω_m, the expression for the modulated signal can be written as follows:

$$\begin{aligned} s_{AM}(t) &= A[1 + m_{AM}cos(\omega_m t)]cos(\omega_c t) \\ &= Acos(\omega_c t) + \frac{m_{AM}A}{2}cos[(\omega_c + \omega_m)t] + \frac{m_{AM}A}{2}cos[(\omega_c - \omega_m)t] \end{aligned} \tag{5.2}$$

Thus, amplitude modulation generates symmetric sidebands around the carrier at frequencies $\omega_c + \omega_m$ and $\omega_c - \omega_m$. For 100% modulation, i.e. $m_{AM} = 1$, the amplitude of each band is half that of the carrier, which corresponds to 6dB lower power than carrier. In amplitude modulation, all the power injected into the signal via the modulating signal is added at the sidebands, without affecting power at the carrier frequency.

Consider frequency-modulation of the carrier at frequency ω_m with a modulation index m_{FM}. The modulated signal now has multiple frequency components:

$$s_{FM}(t) = A[cos(\omega_c t + m_{FM} sin(\omega_m t))]$$
$$= A[cos(\omega_c t)cos(m_{FM} sin(\omega_m t)) - sin(\omega_c t)sin(m_{FM} sin(\omega_m t))] \quad (5.3)$$

Noting that
$cos(m_{FM} sin(\omega_m t)) = \sum_{n=0}^{\infty} 2n J_{2n}(m_{FM}) cos(2n\omega_m t)$ and
$sin(m_{FM} sin(\omega_m t)) = \sum_{n=0}^{\infty} 2 J_{2n+1}(m_{FM}) sin([2n+1]\omega_m t)$, we can express the signal in terms of all its frequency components:

$$s_{FM}(t) = A[J_0(m_{FM})cos(\omega_c t) + \sum \infty_{n=0}(-1)^n J_n(m_{FM})[cos((\omega_c - n\omega_m)t)$$
$$+(-1)^n cos((\omega_c + n\omega_m)t)]] \quad (5.4)$$

The expression highlights the phase relation between all the frequency components. Each sideband is characterised by its order n. The vector sums of the odd-order sideband pairs are always in quadrature with the carrier component of the signal and the vector sums of the even-order sideband pairs are always collinear with the carrier component. The phase shift for the odd-order sidebands arises from the reversal of phase for the lower frequency sidebands with respect to the higher frequency sidebands. The power in the lower and higher frequency sidebands is the same for sidebands of all order. Unlike AM, FM affects the power at the carrier frequency. FM does not involve injecting power into the signal - the modulating signal results in redistribution of the power at the carrier frequency into all the sidebands.

From equations 5.2 and 5.4, it is clear that if a signal has coincidental AM and FM, the higher and lower frequency sidebands of the first order are asymmetric, i.e. the power in the higher frequency sideband is different from the power in the lower frequency sideband. The mismatch in power depends on the phase relationship between the AM and FM processes. It is also interesting to note the effect of introducing asymmetry in the intensities of lower and higher frequency sidebands in equation 5.4. The amplitude of the resulting signal is no longer constant, and has AM in addition to FM.

5.2 AM and FM in Opto-Mechanical Systems

Silicon opto-mechanical resonators operated in the resolved sideband regime stand out as strong candidates for optical frequency modulation (FM) owing to their strongly coupled mechanical and optical degrees of freedom [28]. This coupling mechanism is nonlinear and the non-adiabatic response of the intra-cavity optical field to changes in the cavity size can lead to modification of its mechanical dynamics. On the other hand, if the mechanical resonant mode of the cavity is actuated, the cavity executes oscillatory motion at this frequency which results in Doppler-shift of the circulating intra-cavity optical field, thus modulating its phase. In the frequency domain, this frequency modulation manifests itself as sidebands centered about the input laser frequency line, at a frequency separation that is equal to the frequency of the actuated mechanical resonance. The cavity density of states shapes the resultant sidebands leading to enhancement of only those sidebands that are coupled to the optical cavity, thus causing an asymmetry in the intensity of the lower and higher frequency sidebands. This asymmetry leads to an effective amplitude modulation (AM) of the laser light, in addition to

frequency modulation.

Recall from chapter 2, the expression for the intra-cavity light field in an optomechanical resonator exhbiting sinusoidal mechanical motion, as derived in equation 2.9:

$$a_p(t) = \frac{s}{\sqrt{\tau_{ex}}} \sum_{n=-\infty}^{+\infty} \frac{(-i)^n J_n(\beta)}{\frac{\kappa}{2} + i(\Delta + n\Omega_m)} exp[i(\omega_{opt} + n\Omega_m)t + i\beta cos(\Omega_m t)] \qquad (5.5)$$

Of particular interest are the cases where $\kappa/2 \gg (\Delta+\Omega_m)$ and $\kappa/2 \ll (\Delta+\Omega_m)$. The former case corresponds to unresolved motional sidebands. Noting that $J_{-n}(\beta) = (-1)^n J_n(\beta)$, it is easy to see that the lower and higher frequency primary sidebands are in phase with each other, resulting in predominant amplitude modulation. In the latter case of resolved motional sidebands, the phase relationship is reversed, leading to predominant frequency modulation. For other detuning values, the sidebands are highly asymmetric in the resolved sideband regime. When the detuning is zero, the motion of the optomechanical cavity leads to pure phase modulation of the laser light. For non-zero detuning, the cavity density of states leads to an asymmetry in the relative sideband intensities, which results in coincidental amplitude modulation and frequency modulation of the laser light.

5.3 Experimental Characterization of Optical Sidebands

We use the displacement amplifier array described in chapter 4 for demonstrating the asymmetry in optical sidebands. A high Q optical resonance with a loaded total quality factor ≈110,000 (see Figure 5.1) is chosen, which corresponds to a half width at half maximum linewidth of 881MHz for the optical cavity. This

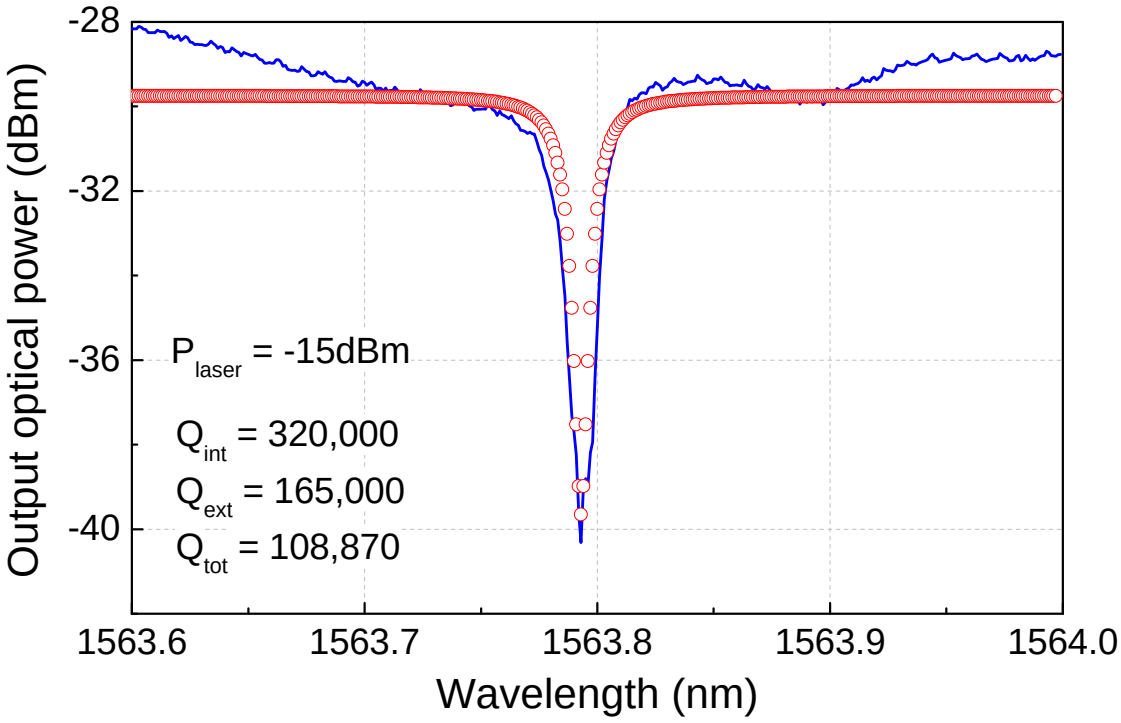

Figure 5.1: A high optical quality factor resonance with half width at half maximum linewidth of 881MHz.

satisfies the resolved sideband regime criterion for the compound radial expansion mode of vibration for the ring at 1.1GHz.

For observing the motion-generated optical sidebands for the modulator, we use a Thorlabs SA210-12B scanning Fabry-Perot (FP) interferometer. The confocal design of this FP Interferometer cavity is relatively insensitive to the alignment of the input beam. The tunable laser is blue detuned to the optical cavity and a bias-tee is used to apply a combination of DC bias voltage and AC voltage at the resonance frequency of the mechanical mode using an Agilent E8257D PSG Analog Signal Generator. Using an SA201 control box for the FP interferometer, the wavelength of the FP cavity is scanned across its entire range by sweeping the voltage on the piezo-controller in the control box. The transmitted light intensity

is measured using an internal photodiode, amplified by a transimpedance amplifier inside the control box, and displayed on an oscilloscope. As the FP cavity scans across wavelengths, its output on an oscilloscope shows a peak whenever it passes across a sideband. The controller also provides a trigger signal to the oscilloscope, which allows the oscilloscope to easily trigger at the beginning or the middle of the scan. The free spectral range (FSR) of the FP interferometer that we use is 1.5GHz, and this information is used to scale the x-axis of the oscilloscope output from units of time to frequency offset from pump laser. The root mean square (RMS) noise voltage of the photo-amplifier in the control box is 1.5mV for a gain setting of 1MV/A. The measured FSR for the cavity is 7.2ms and the full width half maximum (FWHM) linewidth is 35μs, which correspond to 1.5GHz and 7.2MHz respectively, and cavity finesse of 205. An illustration of the experimental setup is shown in Figure 5.2.

Figure 5.3 shows the calculated frequency spectrum showing the intensities of the sidebands for the modulator normalized to the input pump laser intensity for operation and 177.75GHz and 1.09GHz using equation 2.9. The relative detuning, defined as $\frac{2\Delta}{\kappa}$, is set to 0.5. The displacement amplitude was calculated by following the derivation in section 4.6. A displacement amplification factor of $\sqrt{7}$ was accounted for displacement at 1.09GHz.

Figure 5.4 shows measured sideband intensities for the two mechanical modes measured at different relative detuning values. Panels (a)-(b) show recorded optical sidebands at 177.75MHz. As expected, the asymmetry in the sidebands is very small for this mechanical resonant mode of the opto-mechanical cavity, on account of unresolved motional sidebands. A combination of 10V DC and 5dBm AC power was applied at the input electrode of the modulator. Maximum asym-

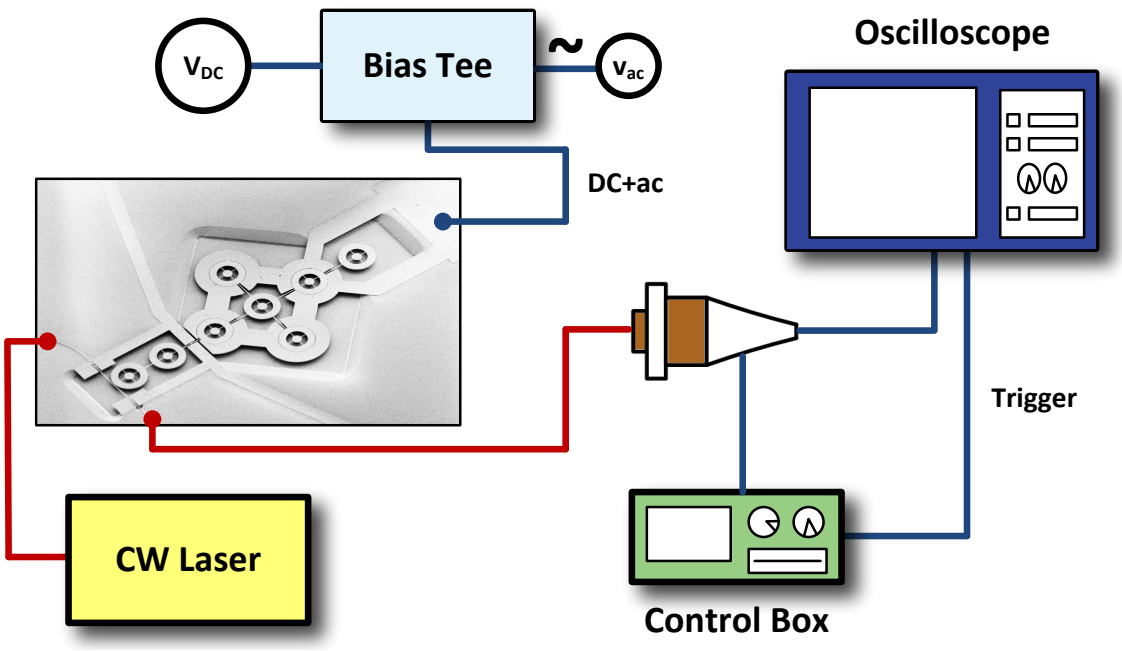

Figure 5.2: Experimental setup for characterization of the optical sidebands of the modulator using a scanning FP interferometer. The frequency of the applied AC voltage corresponds to the resonance frequency of the mechanical mode of interest.

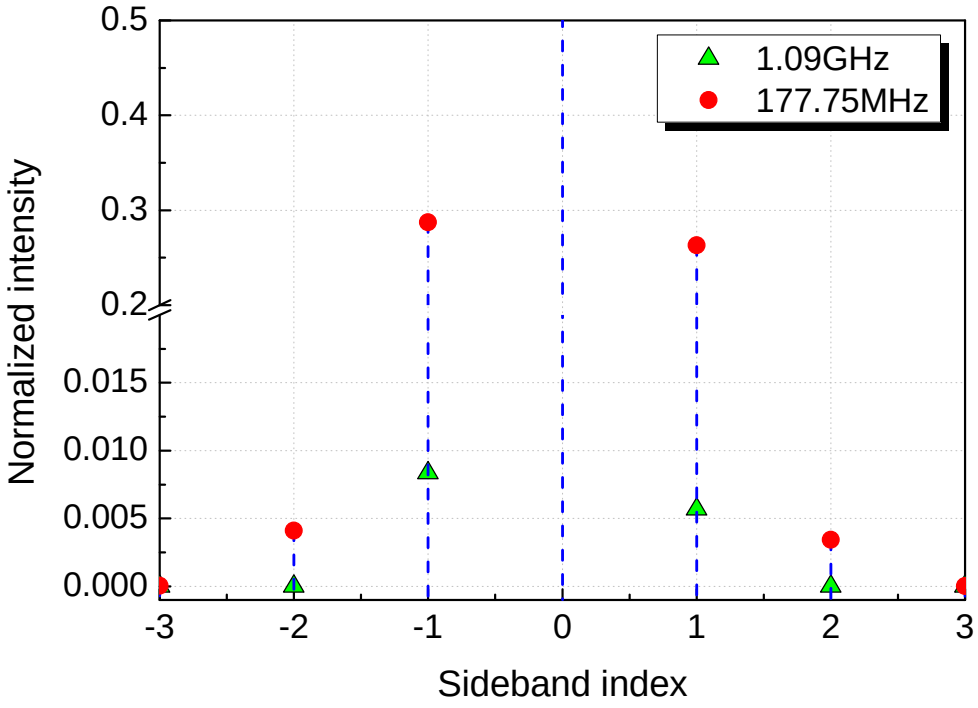

Figure 5.3: Calculated spectrum for the modulator response at 177.75MHz and 1.09GHz for relative detuning of 0.5. A combination of 10V DC and 5dBm AC power was considered at the input electrode for operation at 177.75MHz, and a combination of 20V DC and 8dBm AC power was accounted for at 1.09GHz. The primary sideband intensities are highly asymmetric for operation at 1.09GHz. The Y-axis has a break between 0.02 and 0.2 to clearly show the sideband intensities at both frequencies.

metry is observed for a relative detuning value of 0.5, which corresponds to the half maximum point of the optical cavity resonance. This is in sharp contrast to the highly asymmetric intensities observed in case of the mechanical resonant mode at 1.09GHz as shown in panels (d)-(e). A combination of 20V DC and 8dBm AC power was applied at the electrodes in this case. The asymmetry confirms the co-existence of AM and FM in the light field at the output of the modulator. The apparent mismatch in frequency of the positive and negative frequency sidebands is an artifact of the scan rate of the Fabry-Perot interferometer. It is possible to realize perfect FM with no AM by setting the detuning of the laser with respect to the cavity to zero, but this requires additional feedback loops, such as the Hansch-Couillaud technique [87]. The frequency modulation factor (modulation index) for an opto-mechanical cavity was defined in equation 2.9 as $\beta = \frac{g_{om}}{\Omega_0}$. The measured frequency modulation factor for our modulator operated at 1.09GHz is 0.067, which corresponds to a greater than 67X improvement over earlier reported numbers for silicon nanobeams [88]. This large modulation factor is significant for efficiently generating multiple laser lines in silicon.

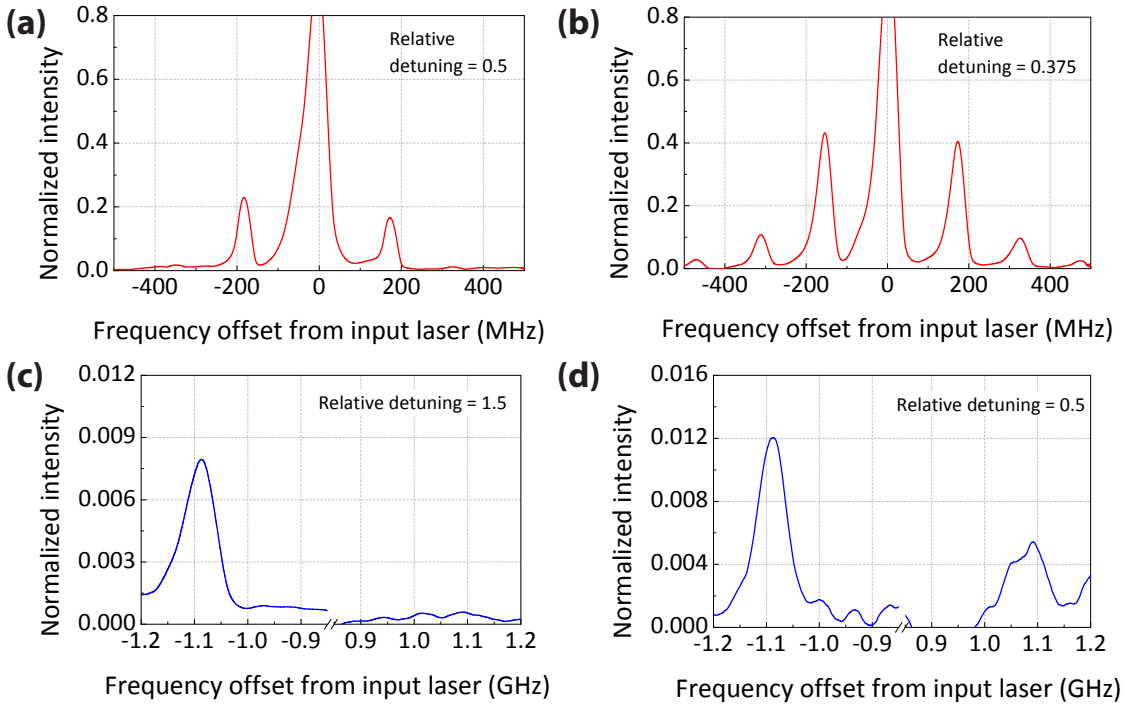

Figure 5.4: Measured optical spectrum at output of the modulator using a scanning FP interferometer. (a)-(b) When operated at 177.75MHz for relative detuning values 0.5 and 0.375, we observe almost symmetric lower and higher frequency sidebands in the optical spectrum on account of amplitude modulation of the laser light. The distorted shape of the laser line is an artifact of the scan. (d)-(e) The sidebands are highly asymmetric in the case of operation at 1.09GHz, which corresponds to resolved motional sidebands. Relative detuning of 1.5 corresponds to detuning on the order of the mechanical resonant frequency, resulting in maximum asymmetry. The free spectral range (FSR) of the FP interferometer used here is 1.5GHz, which leads to aliasing from adjacent sweeps and hence we only show the region of interest around $\pm$1.09GHz.

CHAPTER 6

ELECTRO-MECHANICAL PHOTODETECTOR

Cavity opto-mechanical systems offer a unique platform wherein the coherent interaction rate is larger than the thermal decoherence rate of the system, as realized in ground-state cooling experiments [88]. This interplay of light and motion opens up an array of novel applications in classical and quantum optics communication [89, 90, 91]. In the classical regime, opto-mechanical systems have enabled wide-band optical frequency conversion [92] and multi-channel all-optical radio frequency amplification [93]. Realization of an on-chip silicon communication platform is limited by photo-detectors needed to convert optical information to electrical signals for further signal processing.

Classical and quantum information transfer and storage utilize photons for long range communication [82, 94, 95]. Photons are appealing for such applications on account of their weak interaction with the environment and resiliency to thermal noise due to their high frequency. On the other hand, acoustic phonons have lower bandwidth and experience significantly higher losses associated with transmission, but can be delayed and stored for longer times and can interact resonantly with RF-microwave electronic systems. It has been proposed in the past that a hybrid phononic-photonic system could perform a range of tasks unreachable by purely photonic and phononic systems [41, 96, 97]. Furthermore, such a system should also be capable of being directly integrated with electronics used for processing radio-frequency (RF) signals. Achieving this in an all silicon chip-scale platform has been pursued with great zest, as silicon processing offers benefits in terms of lowering manufacturing cost, obtaining high yields, and promises seamless on-chip integration with electronics. However, as the field of silicon photonics has

grown, a theme that has emerged is that as a platform, silicon does not provide best-in-class devices for all tasks [98]. True monolithic integration of photonics devices with cutting-edge 28nm or smaller CMOS processes is a very challenging task. Making process modifications to support such integration will fundamentally change the models for transistors, at the cost of degrading their performance. Not modifying the process is an option, and recently researchers have shown that some photonic functionality can be integrated with minimal post-processing in a silicon-on-insulator (SOI) CMOS process [99]. A key component for CMOS compatible silicon photonics is a photodiode capable of detecting light in the near infrared. Various CMOS compatible photodiodes have been demonstrated [100, 101, 102] but they suffer from complex processing steps to overcome lattice mismatch issues, large area consumption and susceptibility to dark current. In this chapter, we present an alternate photodetector that responds opto-mechanically to optical intensity modulation, thus converting the signal from photon→phonon→electron, instead of depending on an avalanche or photoelectric process in a non-silicon material. This scheme is universal, and could potentially be of interest to opto-mechanical resonators fabricated in piezoelectric materials such as aluminum nitride [52], and materials with attractive mechanical and optical properties such as single crystalline diamond [103]. The experiments and theoretical analysis presented in this chapter constitute a purely classical demonstration of converting optical modulation to an RF electronic signal. The device we present here can, in principle, enable quantum state transfer as proposed in other opto-mechanical systems [96, 104].

Figure 6.1 shows an illustration showcasing the principle of operation of this detector using the coupled silicon opto-mechanical resonator. The opto-mechanical resonator located in close proximity to the waveguide is actuated via optical gra-

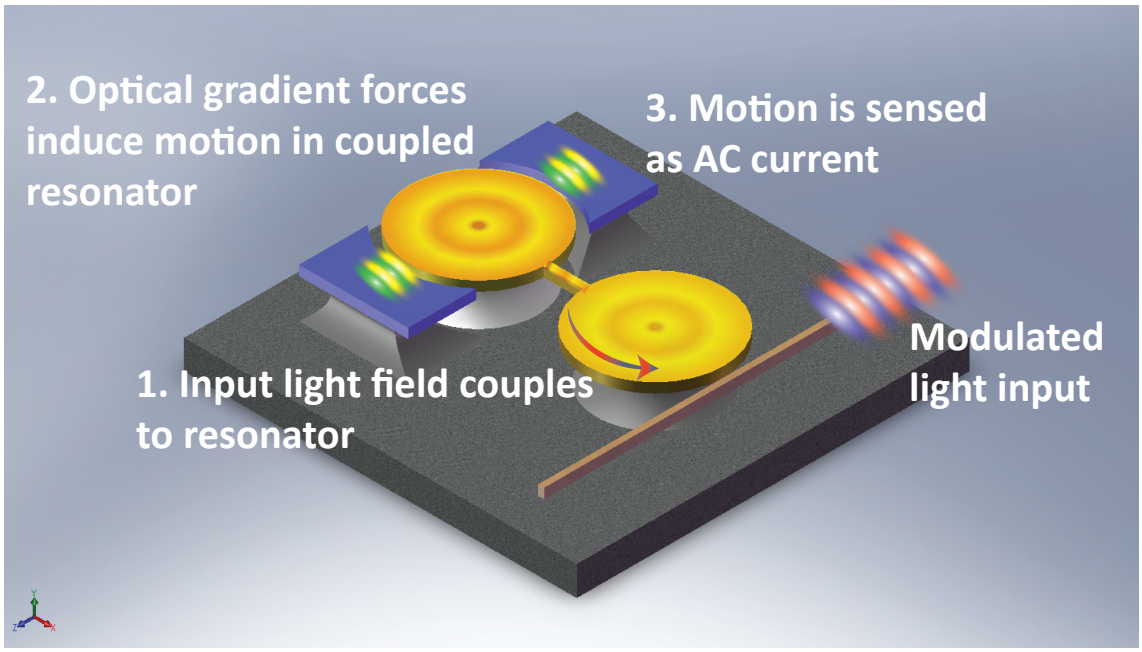

Figure 6.1: Illustration of operation of the electromechanical photodetector.

dient forces generated by the modulated input light field. These mechanical vibrations $\widetilde{x}(\Omega)$ are coupled to the other mechanical resonator flanked by electrodes via the coupling beam. The motion of this resonator is sensed via a high dynamic range electrostatic capacitive sense scheme, resulting in an AC current $(\widetilde{i}_{out}(\Omega))$ generated on account of modulation of the capacitance formed by the air gap between the resonator and the electrode.

6.1 Theoretical Framework

6.1.1 Optical gradient force actuation

Consider an input pump field $A_p(t) = A_{p0}(t) + \delta A_p(t)$, where the first term denotes static field amplitude and the second term is a dynamic modulated

term. Correspondingly the intra-cavity dropped field can be expressed similarly as $a_p(t) = a_{p0}(t) + \delta a_p(t)$, where:

$$a_{p0} = \frac{j\sqrt{\Gamma_{ex}}}{\frac{\Gamma_{tot}}{2} - j\Delta_p} A_{p0} \tag{6.1}$$

Here Δ_p is the detuning of the laser (ω_p) from the cavity resonance (ω_0) and Γ_{in}, Γ_{ex} and Γ_{tot} are the intrinsic cavity photon decay rate, photon decay rate associated with coupling to the cavity, and photon decay rate of the loaded optical cavity respectively. The intra-cavity field is normalized to the intra-cavity energy, $U_p = |a_p|^2$. The optical gradient force acting on the opto-mechanical resonator can then be expressed as follows [32]:

$$F_{grad} = -\frac{g_{OM} U_p}{\omega_p} \tag{6.2}$$

g_{OM} denotes the opto-mechanical coupling coefficient. The gradient force consists of two terms: $F_{grad}(t) = F_{grad,0}(t) + \delta F_{grad}(t)$. The first term is a static force whereas the second term is the dynamic component related to the laser light modulation $\delta U_p(t)$, given by:

$$\delta F_{grad}(t) = -\frac{g_{OM}\delta U_p}{\omega_p} = -\frac{g_{OM}}{\omega_p}\left[a^*_{p0}\delta a_p(t) + a_{p0}\delta a^*_p(t)\right] \tag{6.3}$$

The mechanical motion (x) of the cavity follows: $\ddot{x} + \Gamma_m\dot{x} + \Omega_m^2 x = \frac{F_{grad,0}(t)+\delta F_{grad}(t)+F_T}{m_{eff}}$, where m_{eff} is the effective mass of the mechanical mode with frequency Ω_m, Γ_m is the intrinsic mechanical damping rate, and F_T is the thermal Langevin force responsible for the thermal Brownian motion. The dynamic displacement of the resonator is affected largely by the dynamic gradient force, as the

thermal Langevin force is relatively much smaller in magnitude. The back-action of the mechanical motion changes the value of the resonant frequency and damping rate of mechanical motion. The spectral response of this force is given by [32]:

$$f_0(\Omega) = -\frac{2g_{OM}^2 U_{p0}\Delta_p}{\omega_p} \frac{\Delta_p^2 - \Omega^2 + \left(\frac{\Gamma_{tot}}{2}\right)^2 + j\Gamma_{tot}\Omega}{\left[(\Delta_p + \Omega)^2 + \left(\frac{\Gamma_{tot}}{2}\right)^2\right]\left[(\Delta_p - \Omega)^2 + \left(\frac{\Gamma_{tot}}{2}\right)^2\right]} \tag{6.4}$$

Define $\ell(\Omega) = \Omega_m^2 - \Omega^2 - j\Gamma_m\Omega - \frac{f_o(\Omega)}{m_{eff}}$. The dynamic mechanical displacement on account of the optical gradient force is given by:

$$\widetilde{x}(\Omega) = \frac{j\sqrt{\Gamma_{ex}}g_{OM}}{m_{eff}\omega_p\ell(\Omega)}\left[\frac{a_{p0}^*\delta\widetilde{A}_p(\Omega)}{j(\Delta_p + \Omega) - \frac{\Gamma_{tot}}{2}} + \frac{a_{p0}\delta\widetilde{A}_p^*(-\Omega)}{j(\Delta_p - \Omega) + \frac{\Gamma_{tot}}{2}}\right] \tag{6.5}$$

Here $\delta\widetilde{A}_p$ is the Fourier domain representation of the modulated input light field. This expression is complete in the sense that it accounts for motion actuated due to the optical gradient force acting on the resonator, and also the back-action induced by the motion on the optical field. Substituting equation 6.1 into equation 6.5 yields:

$$\widetilde{x}(\Omega) = \frac{-\Gamma_{ex}g_{OM}}{m_{eff}\omega_p\ell(\Omega)\left(\frac{\Gamma_{tot}}{2} - j\Delta_p\right)}\left[\frac{A_{p0}^*\delta\widetilde{A}_p(\Omega)}{j(\Delta_p + \Omega) - \frac{\Gamma_{tot}}{2}} + \frac{A_{p0}\delta\widetilde{A}_p^*(-\Omega)}{j(\Delta_p - \Omega) + \frac{\Gamma_{tot}}{2}}\right] \tag{6.6}$$

In the unresolved sideband regime, the equation above reduces to the limit $\lim_{\Omega\to 0}\widetilde{x}(\Omega)$:

$$\widetilde{x}(\Omega) \tag{6.7}$$

$$\approx \frac{-\Gamma_{ex} g_{OM} \left[-j\Delta_p \left(A^*_{p0} \delta\widetilde{A}_p(\Omega) + A_{p0} \delta\widetilde{A}^*_p(-\Omega) \right) \right]}{m_{eff}\omega_p \ell(\Omega) \left(\frac{\Gamma_{tot}}{2} - j\Delta_p \right) \left[\Delta_p^2 + \frac{\Gamma_{tot}^2}{4} \right]} \tag{6.8}$$

$$= \frac{j\Delta_p \Gamma_{ex} g_{OM} \delta P_{in}(\Omega)}{m_{eff}\omega_p \ell(\Omega) \left(\frac{\Gamma_{tot}}{2} - j\Delta_p \right) \left[\Delta_p^2 + \frac{\Gamma_{tot}^2}{4} \right]} \tag{6.9}$$

The derivation above assumes that the displacement amplitude of the resonator is small i.e. the perturbation of the detuning on account of mechanical motion is very small compared to the unperturbed detuning $\left(\frac{x(t)}{R}\omega_0 \ll \Delta_p \right)$. In the large amplitude regime, where the detuning oscillates between large positive and negative values, the small signal model derived above fails to hold. An extensive study of opto-mechanical oscillation amplitudes was recently presented by Poot et al. [105]. The optical backaction on the resonator enables radiation pressure induced self-sustained oscillations whose limit cycle is set by the dynamic range of the cavity. This sets a maximum limit on the amplitude of mechanical motion [105], which would amount to saturation of the motional current generated by the detector.

6.1.2 Electrostatic capactively transduced sense scheme

If C denotes the capacitance formed by the air gap between the resonator and the electrode, and g denotes the resonator-electrode gap, the motional current flowing into the electrode in response to the motion of the resonator and applied DC voltage, V_{dc} is expressed as:

$$i_{out}(t) = V_{dc}\frac{dC}{dt} = V_{dc}\frac{dC}{dg}\frac{dg}{dt} \tag{6.10}$$

The dynamic component of this current can then be written down as:

$$\widetilde{i}_{out}(\Omega) = V_{dc}\frac{dC}{dg}j\Omega\widetilde{x}(\Omega) = V_{dc}\frac{\epsilon_0 Rh\theta}{g^2}j\Omega\widetilde{x}(\Omega) \tag{6.11}$$

Here R, h and θ denote the outer radius of the resonator, device thickness and the electrode-resonator overlap angle respectively. Substituting equation 6.9 into equation 6.11, we get:

$$\frac{\widetilde{i}_{out}(\Omega)}{\delta P_{in}(\Omega)} = \frac{-\Delta_p\Gamma_{ex}g_{OM}V_{dc}\epsilon_0 Rh\theta\Omega}{g^2 m_{eff}\omega_p\ell(\Omega)\left(\frac{\Gamma_{tot}}{2} - j\Delta_p\right)\left[\Delta_p^2 + \frac{\Gamma_{tot}^2}{4}\right]} \tag{6.12}$$

The expression derived above in equation 6.12 can be interpreted as the "electromechanical responsivity" ($\Re_{em}$) of the detector.

6.2 Experimental Characterization

We choose the coupled micro-ring geometry with a resonator-electrode gap of 50nm described in Chapter 3 for the photodetector. Figure 6.2 shows a schematic of the experimental setup used to characterize the photodetector performance. Light from a Santec TSL-510 tunable diode laser is modulated with a Photline MXAN-LN-10 lithium niobate electro-optic intensity modulator (EOM). An Agilent N5230A network analyzer is used to characterize the detector efficiency. The input laser light is modulated by connecting the RF input of the modulator to port

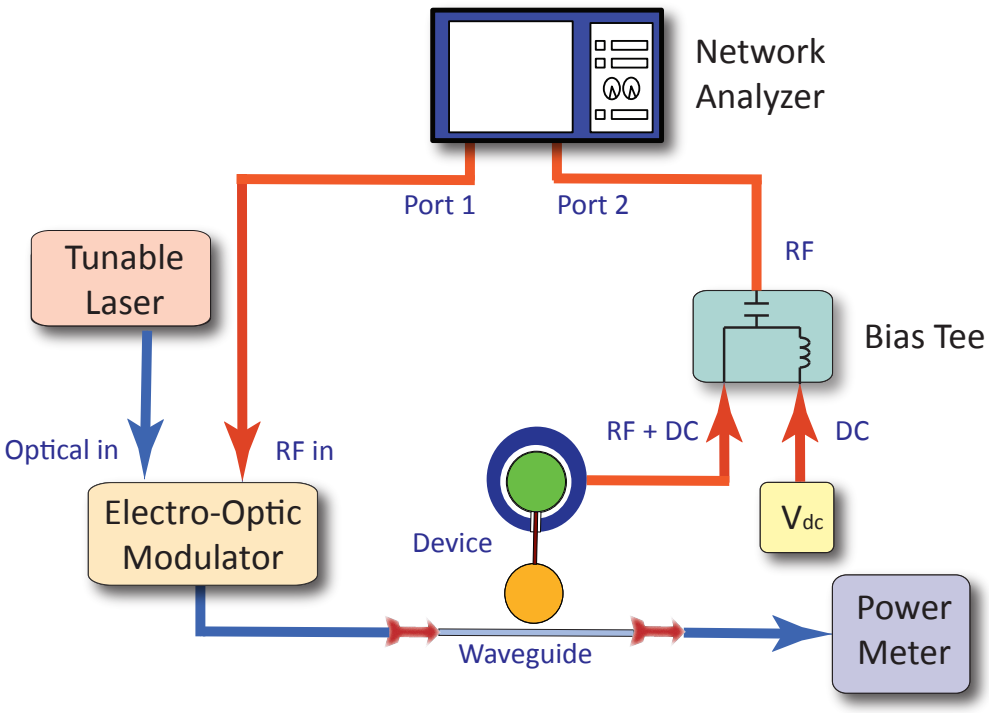

Figure 6.2: Schematic of the experimental setup used to characterize the silicon detector. Mechanical motion is actuated by modulating continuous wave laser light coupled into the opto-mechanical resonator using a Photline MXAN-LN-10 electro-optic modulator. The mechanical motion is sensed via electrostatic capacitive actuation by applying V_{dc} = 40V DC voltage at the electrode using a bias tee. A network analyzer is used to measure the 2-port transmission of the device.

1 of the network analyzer. The output power is sensed by connecting the signal from the metal bond pad to port 2 of the network analyzer.

The silicon opto-mechanical resonator has many optical resonances in the C-band as seen in Figure 6.3(a). For the purpose of this experiment we choose an overcoupled resonance at 1,548.9nm, with an extinction of 8dB shown in Figure 6.3(b). As derived in equation 6.12, the motional current amplitude is proportional to the cavity coupling rate, Γ_{ex}, and hence operating with an overcoupled resonance

is desirable. However, this also reduces the loaded optical quality factor, and hence there is a trade-off associated with overcoupling to the resonator. The rich optical spectrum of the resonator offers us a wide choice of optical resonances to choose from.

A DC bias voltage of 40V is applied at the metal bond pad using a bias tee. We apply an input RF power ($P_{in,RF}$) of 0dBm at port 1 of the network analyzer, and measure the output RF power (P_{out}) at port 2. The transmission of the device operated in this configuration corresponds to the "gain" of the photodetector ($P_{out}/P_{in,RF}$). Figure 6.4 shows the measured gain for the detector at various input laser power levels measured at the resonator (by discounting the coupling loss). The signals measured correspond to mechanical vibrations of the fundamental radial expansion mode at 174.2MHz and compound radial expansion mode at 1.198GHz (panel (a) and (b) respectively). The measured gain depends on the input laser power, akin to nanomechanical resonator based microwave amplification reported by Massel et al. [89].

The maximum laser power is set 4dB below the threshold for onset of radiation pressure induced self-oscillations of the fundamental radial expansion mode. Measurements were carried out at room temperature and 5mTorr pressure. The minimum detectable signal at the sense port of the network analyzer (port 2) is set by the receiver's noise floor at this port, which depends on the averaging factor used while carrying out the measurement. An averaging factor of 16 was used in all the measurements to optimize the sensitivity of the network analyzer. The RF power applied at port 1 of the network analyzer is 0dBm. The input laser wavelength is set to the 3-dB off resonance wavelength, and the laser is blue detuned with respect to the optical cavity. Measurements were carried out at room

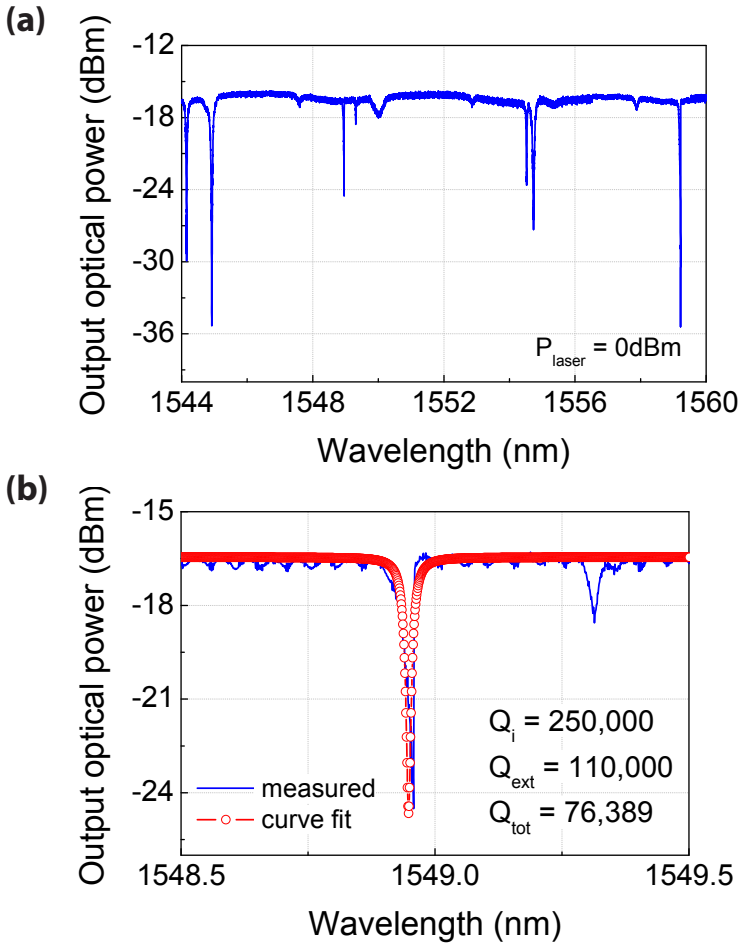

Figure 6.3: (a) Optical spectrum for the opto-mechanical resonator based silicon photodetector. The input laser power is +2dBm. The connectors and grating couplers add 8dB loss at each facet. (b) High optical Q resonance used to operate the photodetector. We intentionally choose an overcoupled resonance in order to measure larger motional current.

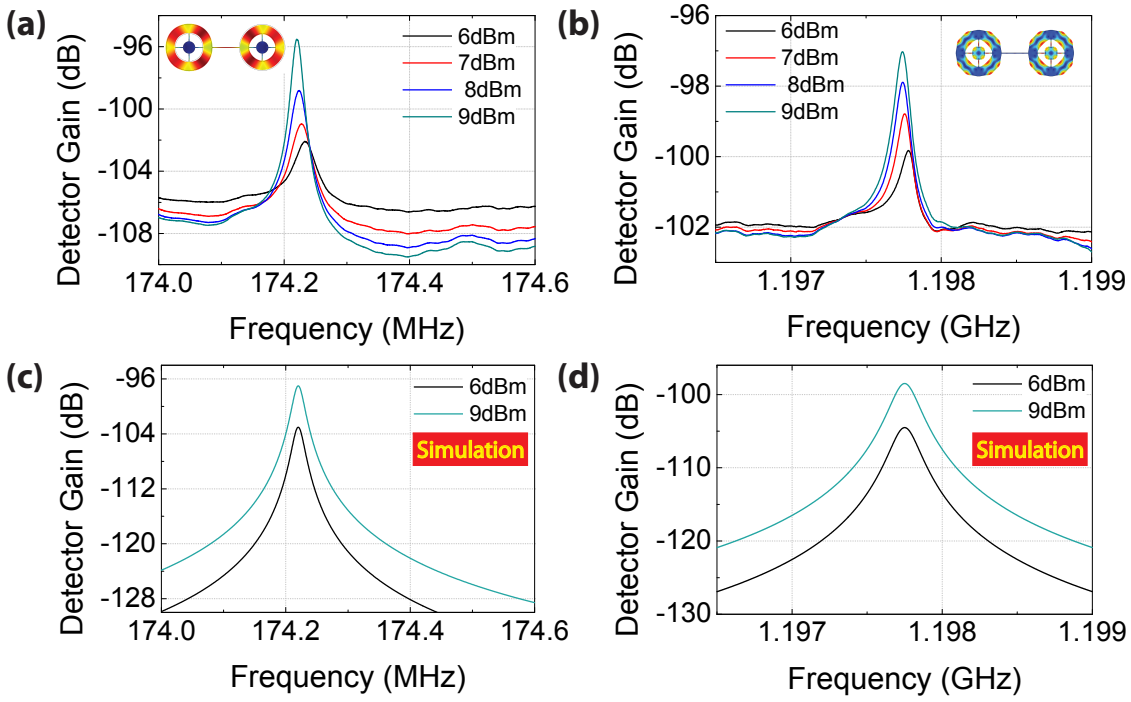

Figure 6.4: Frequency spectra for the detector gain ($P_{out}/P_{in,RF}$) measured using network analyzer. Measured detection of optical modulation for (a) fundamental radial expansion mode at 174.2MHz, and (b) compound radial expansion mode at 1.198GHz. The insets in panels (a) and (b) show the corresponding finite element method (FEM) simulated mechanical mode-shapes. (c) Simulated transmission at frequencies near the fundamental radial expansion resonance frequency for laser power = +6dBm and +9dBm. (d) Simulated transmission at frequencies near the compound radial expansion resonance frequency for laser power = +6dBm and +9dBm. Simulations for expected gain are based on equation 6.11. Measurements were carried out at room temperature and a pressure of 5mTorr.

temperature and a pressure of 5mTorr. The measured mechanical quality factors at 174.2MHz and 1.198GHz are 8,700 and 6,300 respectively. Substituting all the experimental parameters into equation 6.11 and calculating the output power, $P_{out} = \frac{|i_{out}|^2 R}{2}$, where $R = 50\Omega$ is the load resistance, yields a conversion gain of -97dB at 174.2MHz, and -98dB at 1.198GHz for +9dBm input laser power. The simulated gain at frequencies near 174.2MHz and 1.198GHz are shown in Figure 6.4(c) and (d), which closely match measured gain values. The shift of the mechanical resonance frequency with increasing input laser power is attributed to thermal heating of the device due to absorption of light coupled into the optical cavity. Native single crystal silicon resonators have negative temperature coefficient of frequency (TCF), and hence larger optical power coupling into the cavity lowers the mechanical resonance frequency. This shift in frequency is negligibly small compared to the intrinsic mechanical resonance frequency $\left(\frac{\Delta\Omega_m}{\Omega_m} \sim 0.1\%\right)$ and hence this effect is not taken into account in simulation.

The conversion of signal from photons to phonons results in a conversion loss of Ω_m/ω_p, which is to be expected, as evident in equation 6.12. The loss values at 174.2MHz and 1.198GHz are -60dB and -52dB respectively. Gaining insights from equation 6.12, one could envisage a detector design with larger gain that benefits from higher optical quality factor (Q_{tot}) resonances, smaller resonator-electrode gaps (g), and smaller detuning (Δ_p). However, choosing a smaller detuning value could potentially launch the device into radiation pressure induced self-oscillations [105], which leads to amplitude saturation.

In conclusion, this constitutes the first experimental demonstration of an on-chip electro-mechanical detector fabricated on a CMOS SOI platform. The electro-mechanical sense scheme enables a high dynamic range detection medium, and

we observe efficient signal detection at 174.2MHz all the way up to 1.198GHz. The resonant nature of this scheme makes this device a narrow-band detector, whose bandwidth is limited by the quality factor of the mechanical resonance. The sense scheme is universal, and can also be used for detection of optical modulation induced by radiation pressure vibrations, which has successfully been demonstrated at GHz rates in silicon [41]. This electro-mechanical detector thus introduces a valuable component in the library of existing novel opto-mechanical devices.

CHAPTER 7

CONCLUSION AND FUTURE WORK

This thesis focused on scaling conventional electrostatic capacitive MEMS transduction to frequencies beyond GHz. To this end, an array of coupled silicon opto-mechanical resonators was employed in a feedback loop to demonstrate oscillations at 2.05GHz. The process flow for post-release photolithography on a MEMS device developed in this thesis will find useful applications across various areas in MEMS, where the release step was conventionally considered the final processing step while fabricating a device. Rayleigh scattering in optical resonators was explored for boosting the displacement sensitivity at frequencies beyond 3GHz (see appendix E), and future research efforts could focus on employing a combination of all the techniques developed here with advances in fabrication technology to design MEMS oscillators for the microwave X-band, both in silicon and in various other materials such as aluminum nitride, lithium niobate and CVD diamond. A combination of radiation pressure induced oscillations along with closed-loop forced feedback oscillations in the same opto-mechanical resonator could be investigated to further lower the phase noise in opto-mechanical oscillators. Both oscillation phenomena have been well characterized individually [105, 106], and the technology developed as part of this thesis should enable bringing together both these phenomena and studying the dynamics involved. Some of the other potential novel experiments and applications that could benefit from the work presented in this dissertation are highlighted below.

7.1 Future Experiments

7.1.1 Unreleased opto-mechanical oscillator (OMO)

Conventional OMO designs have involved fabricating released resonators, that face problems of thermal optical nonlinearities and are not robust designs. Releasing such resonators could also present fabrication challenges that make their realization in a CMOS compatible process fairly complicated. Unreleased resonators, on the other hand, demonstrate fairly linear optical resonances over a large range of input laser power. The cladding surrounding the resonator also enhances the optical quality factor of these resonators due to reduced surface scattering losses, as discussed in Chapter 3. Optical frequency comb generation has been demonstrated in similar silicon nitride micro-ring resonators [107, 108]. Whether unreleased resonators are realized in a CMOS or custom process, their implementation provides high yield, low cost, robustness in harsh environments, and minimal or no-packaging solutions. As a result of the leakage of acoustic energy by wave paths into the surrounding medium, the mechanical performance of an unreleased resonator is degraded relative to its released counterpart. This energy loss can be mitigated by adding acoustic isolation structures [109]. Integrating acoustic Bragg reflectors (ABRs) with an unreleased opto-mechanical resonator to design for simultaneously high optical and mechanical quality factors could potentially enable realization of an unreleased opto-mechanical oscillator. Moreover it is possible to design ABRs to realize GHz range frequencies using unreleased micro-ring resonators, which would otherwise be practically challenging to achieve [19]. The mechanical resonance frequency depends solely on the width of the ring resonator whereas the free spectral range of the optical frequency comb depends solely on

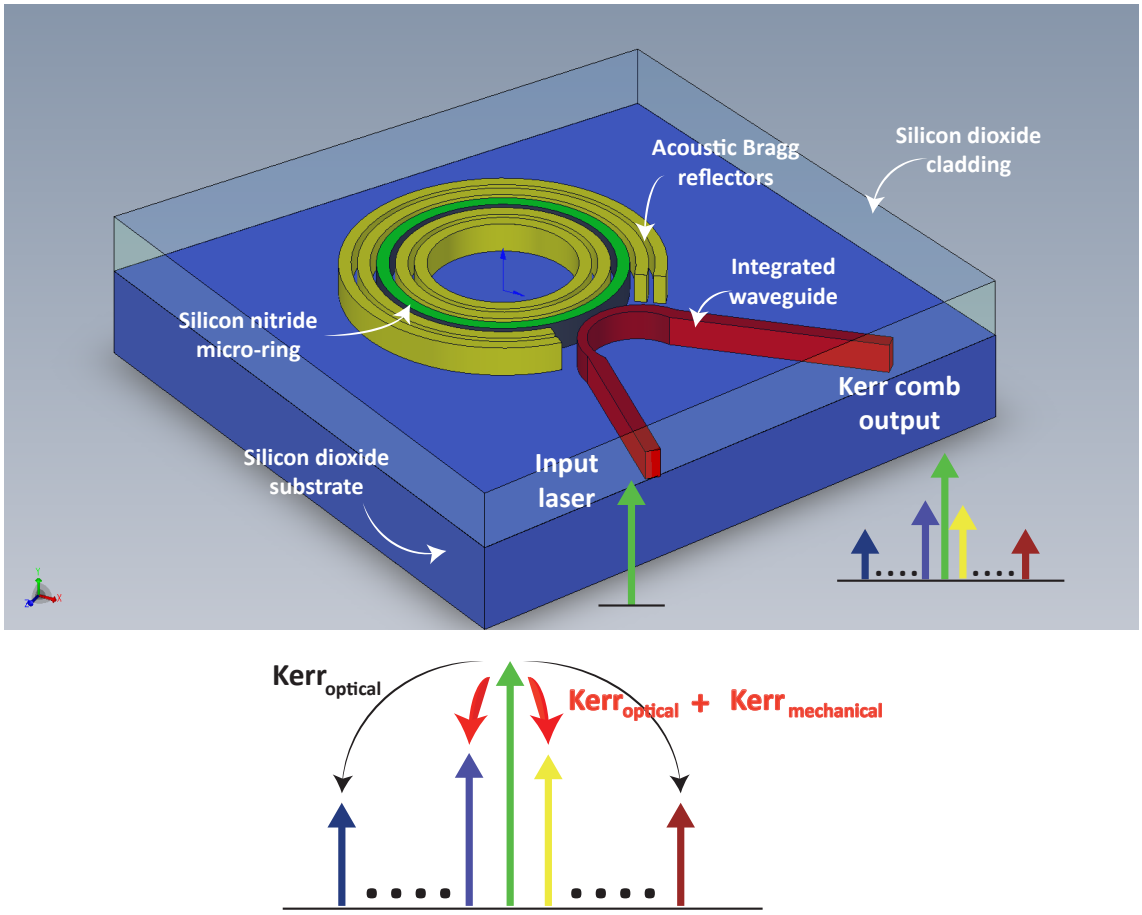

Figure 7.1: Illustration of a silica-cladded silicon nitride micro-ring resonator for generation of Kerr and acousto-optic frequency combs. Acoustic Bragg reflectors help confine the mechanical energy thereby leading to high mechanical quality factors. Operating with optical input power beyond the threshold for optical frequency comb generation and radiation pressure induced oscillations of the mechanical mode could potentially be employed to generate coincident combs by designing the mechanical resonance frequency equal to the free spectral range (FSR) of the optical frequency comb lines.

the circumference of the ring and not the width. By matching these two frequencies, one could design a hybrid acousto-optic modulated micro-comb that would open up avenues for frequency comb stabilization via acousto-optic modulation in a manner similar to recent demonstrations in hycrid electro-optically modulated micro-combs [110]. Figure 7.1 shows an illustration of such a scheme.

7.1.2 2D Opto-mechanical gyroscope

The state-of-the-art in gyroscopey is the hemispehrical resonator gyroscope (HRG) manufactured by Northrop Grumman, which is a navigational grade gyroscope used in inertial navigation units and satellite platform positioning [111]. However, this gyroscope is expensive, bulky, and laborious to manufacture. Chip-scale MEMS gyroscopes typically use electrostatic actuation which require metal electrodes to be integrated with the device. On the other hand, dielectric materials have lesser internal damping, and a gyroscope designed in such a material platform could benefit from the high mechanical quality factors [112, 113]. Opto-mechanical transduction could be utilized to both actuate and read off the vibrations. NASA JPL's silicon disc resonator gyroscope (Si DRG) is currently being commercialized and, through independent Army testing, has proven to be the highest performing MEMS gyroscope in the world [114]. the structure is based on concentric rings with arcs cut into the rings to provide more flexibility, better accuracy and performance, and reduced shock sensitivity. Figure 7.2 shows an SEM of a DRG resonator with outer radius 60μm fabricated in silicon nitride following the process flow detailed in Chapter 3. A pump-probe setup was used to interrogate the mechanical modes of this structure.

Figure 7.3 (a) shows a schematic of the experimental setup. A high power pump

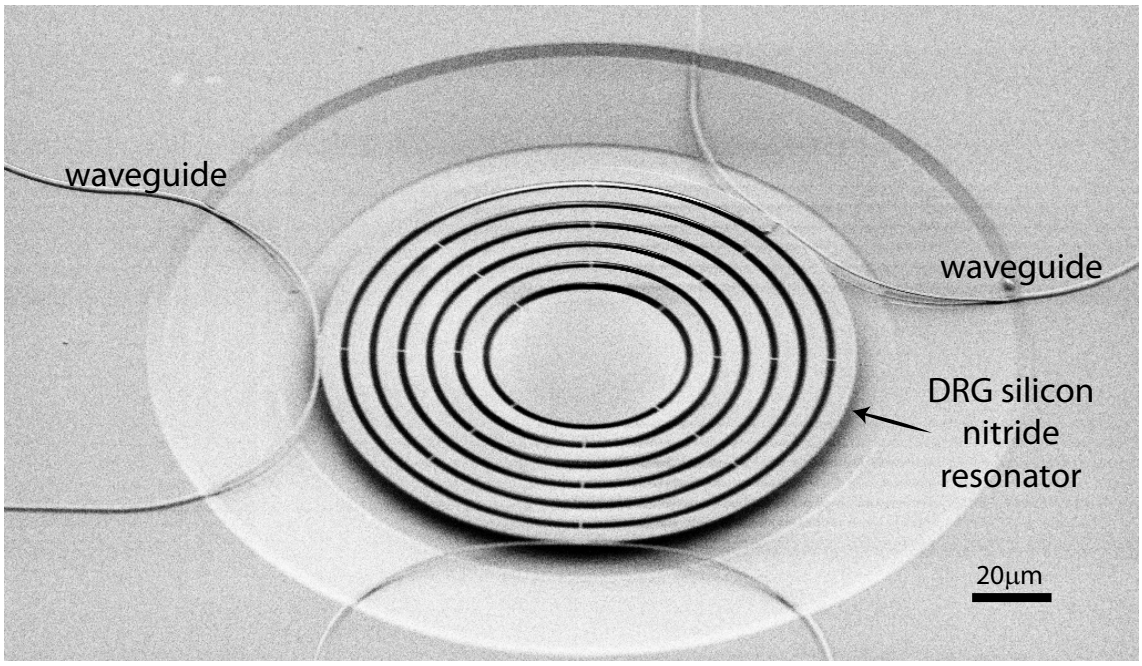

Figure 7.2: SEM of a silicon nitride DRG resonator fabricated in the process flow described in Chapter 3. Multiple waveguides can be employed to probe the motion of the device at various points.

laser coupled into an optical resonance of the opto-mechanical resonator is modulated using an electro-optic modulator (EOM) to launch mechanical vibrations in the resonator via optical gradient forces. A low power probe laser is also coupled into the same waveguide along with the pump using a 50:50 power combiner. The probe laser is coupled to a different optical resonance of the resonator. As the resonator vibrates in response to the optical gradient force, the probe laser is modulated and can be used to sense the vibrations. An optical filter is used to filter out the pump at the output such that the photodetector converts the modulation information carried solely by the probe laser into an RF signal. Using a network analyzer, we can obtain an electro-opto-mechanical transmission spectrum for the silicon nitride DRG as shown in Figure 7.3 (b). Two pairs of orthogonal wineglass modes are identified, and one could optimize the mechanical design to obtain high mechanical quality factors to design an opto-mechanically transduced gyroscope. Figure 7.2 also shows a DRG integrated with multiple waveguides to probe the resonator at various points along its circumference.

In addition to designing high performance RF MEMS oscillators, this thesis also focused on developing MEMS techniques to realize applications and conduct fundamental studies benefitting the photonics community. The displacement amplifier array of coupled opto-mechanical resonators was employed to demonstrate acousto-optic frequency modulation. The electro-mechanical photodetector demonstration using the device developed in this thesis could also potentially be employed for photon-phonon state transfer [115], and extend the applicability of opto-mechanics.

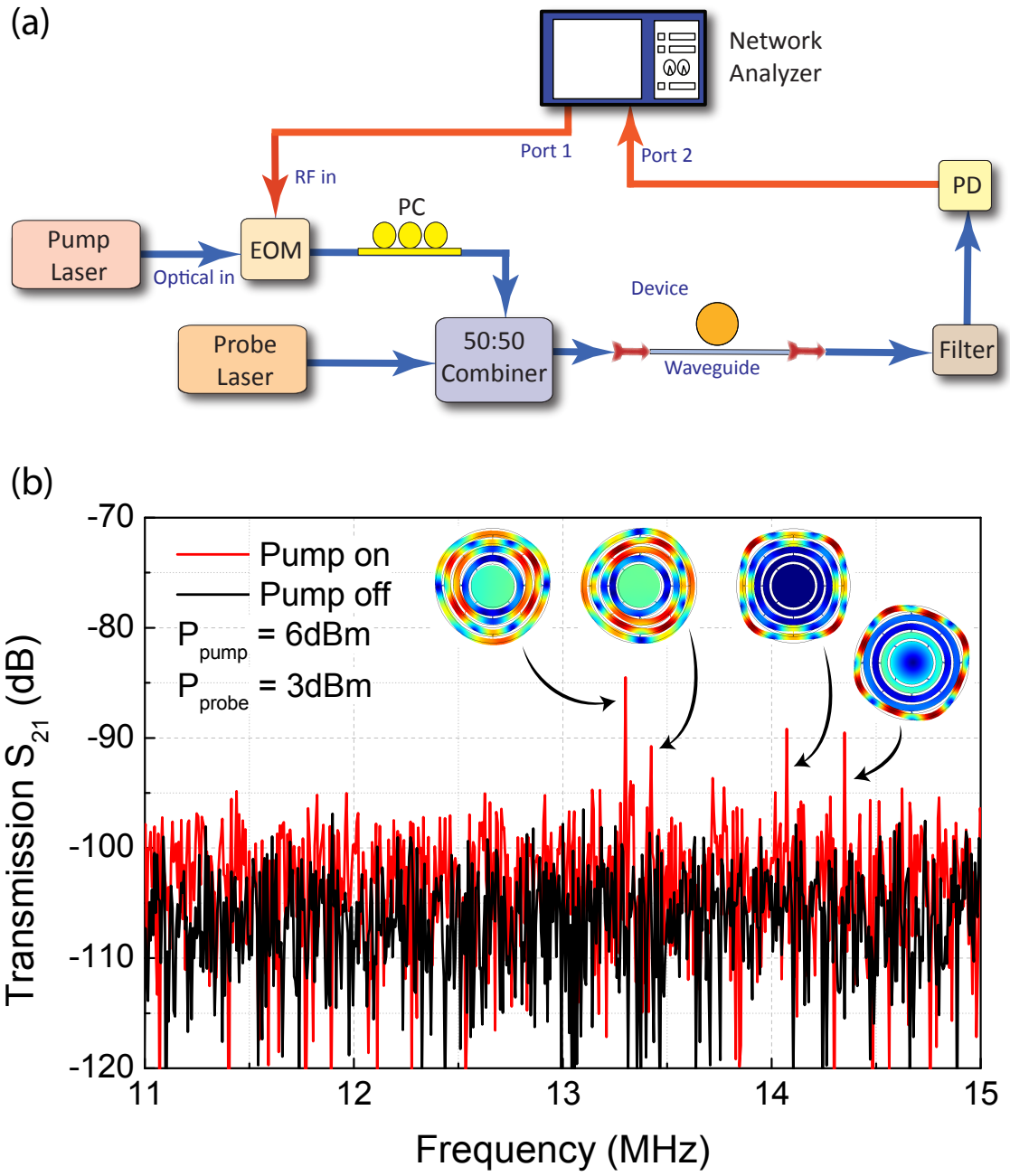

Figure 7.3: (a) Pump-probe setup used to interrogate the mechanical modes of the DRG design. (b) Electro-mechanical transmission spectrum of the DRG design showing two pairs of orthogonal wineglass mechanical modes suitable for gyroscopy.

APPENDIX A

PROCESS FLOW FOR FABRICATING SILICON NITRIDE OPTO-MECHANICAL RESONATORS

The starting substrate for the fabrication of the silicon nitride opto-mechanical resonator is a silica on silicon wafer with 4μm thermal oxide on silicon substrate.

1. Measure SOI stack

Equipment : Filmetrics

Measure stack height to establish oxide thickness

2. MOS clean

Equipment : MOS clean wet bench

Recipe: 10 minutes dip in 1:1:6 NH_4OH:H_2O_2:H_2O at 70°C

10 minutes dip in 1:1:6 HCl:H_2O_2:H_2O at 70°C

Rinse in De-Ionized (DI) H_2O

3. LPCVD silicon nitride deposition

Equipment : LPCVD nitride furnace - B4

Recipe: 100 minutes standard nitride deposition recipe to obtain 300nm Si_3N_4.

4. Surface clean/preparation

Equipment : General chemistry hood

Recipe: 2 minutes dip in Surpass 3000 with ultrasonic agitation

Rinse in DI H_2O

5. Resist spin

Equipment : E-beam resist spinner

Recipe: Spin ma-N 2403 e-beam resist with parameters:

Speed = 3000rpm, ramp = 2000 rpm/s, time = 30s

Hard bake at 90°C for 1 minute

6. E-beam lithography

Equipment : JEOL 9500 e-beam lithography system

Recipe: Expose at 5nA with dose of 550μC/cm^2 using proximity correction.

7. Develop

Equipment : Electron beam resist hood

Recipe : 75s in 726MIF developer

8. Resist height measurement

Equipment: P-10 profilometer

Recipe: Measure step height of the resist across alignment marks

9. Descum

Equipment: Oxford 81 etcher

Recipe:Oxygen plasma clean on empty chamber, time = 10 minutes

Oxygen plasma clean recipe on sample, time = 8s

10. Nitride etch

Equipment: Oxford 100 etcher

Recipe: Oxygen plasma clean on blank Si wafer, time = 10 minutes

CHF_3O_2 nitride etch season on blank Si wafer for 3 minutes

CHF_3O_2 nitride etch on sample, time = 4 minutes 7 seconds

11. Metrology

Equipment : P-10 profilometer and Filmetrics

Recipe: Measure step height on P-10 profilometer and silicon nitride - buried oxide stack on filmetrics. Use measurements to determine if nitride device layer is completely etched.

12. Resist strip

Equipment : YES asher

Recipe: Use parameters O_2 flow rate = 100ssccm, Power = 1000W, Temperature = 150°C, Time = 180s.

13. Step height measurement

Equipment : P-10 profilometer

Recipe: Measure step height on P-10 profilometer after resist removal to obtain depth of over etch into oxide.

14. PECVD oxide deposition

Equipment: GSI PECVD

Recipe: Oxygen plasma clean, time = 15 minutes

Low dep rate PECVD oxide recipe on dummy wafer for 10 minutes, followed by 10 minutes clean

Low dep rate PECVD oxide recipe on sample for 10 minutes, followed by 10 minutes clean

15. Metrology

Equipment : P-10 profilometer and Filmetrics

Recipe: Measure step height on P-10 profilometer and oxide - silicon nitride - buried oxide stack on filmetrics. Use measurements to determine if 1μm thick oxide cladding is achieved.

16. Resist spin

Equipment : Photo resist spinners

Recipe: Spin SPR 220-3.0 photoresist with parameters:

Speed = 3000rpm, ramp = 1000 rpm/s, time = 30s

Hard bake at 115°C for 90s

17. Expose - release mask

Equipment : ABM contact aligner

Recipe: Exposure time of 8s

Post exposure bake at 115°C for 90s

18. Develop

Equipment : General chemistry hoods

Recipe: 90s in 726MIF developer

19. Partial cladding etch

Equipment: Oxford 82 etcher

Recipe:Oxygen plasma clean on empty chamber, time = 10 minutes

CHF_3O_2 oxide etch recipe on empty chamber, time = 10 minutes

CHF_3O_2 oxide etch recipe on sample, time = 10 minutes

20. Hard bake

Equipment : Photoresist/E-beam resist hotplates

Recipe: 20 minutes at 140°C

21. Timed release etch

Equipment : Acid Hood

Recipe: 36 minutes 30 seconds in BOE 6:1

22. Resist strip and CPD preparation

Equipment : Base/Solvent Hood

Recipe:10 minutes dip in acetone for resist removal

5 minutes rinse in 1:1 isopropyl alcohol:DI H_2O

5 minutes rinse in isopropyl alcohol

23. Critical point drying Equipment : Critical point dryer

Recipe: Transfer samples to critical point dryer without exposing to air and run standard recipe.

APPENDIX B

PROCESS FLOW FOR FABRICATING SILICON OPTO-MECHANICAL RESONATORS WITH ALD PARTIAL AIR GAPS

The starting substrate for the fabrication of the coupled micro-ring silicon opto-acoustic oscillator is a silicon on insulator wafer with 250nm thick high resistivity (10-20 ohm-cm) (100) silicon device layer on 3μm buried oxide.

1. Measure SOI stack

Equipment : Filmetrics

Measure stack height to establish device layer Si and buried oxide thickness

2. MOS clean

Equipment : MOS clean wet bench

Recipe: 10 minutes dip in 1:1:6 NH_4OH:H_2O_2:H_2O at 70°C

10 minutes dip in 1:1:6 HCl:H_2O_2:H_2O at 70°C

Rinse in De-Ionized (DI) H_2O

3. Thermal oxidation : hard mask creation

Equipment : Wet/Dry Oxide furnace - B2

Recipe: 24 minutes at 900°C using wet HCl oxidation to obtain 60nm oxide hard mask.

4. Surface clean/preparation

Equipment : Acid chemical hood

Recipe: 2 minutes dip in Nanostrip

Rinse in DI H_2O

5. Resist spin

Equipment : E-beam resist spinner

Recipe: Spin ma-N 2403 e-beam resist with parameters:

Speed = 5000rpm, ramp = 2000 rpm/s, time = 30s

Hard bake at 90°C for 1 minute

6. E-beam lithography

Equipment : JEOL 9500 e-beam lithography system

Recipe: Expose at 2nA with dose of 1000μC/cm^2 for waveguides, 800μC/cm^2 for gratings, 600μC/cm^2 for the resonators and 500μC/cm^2 for the electrical routing and probe pads. For arrayed resonators, use 550μC/cm^2 and for arrayed electrodes, use 400μC/cm^2.

7. Develop

Equipment : Electron beam resist hood

Recipe : 75s in 726MIF developer

8. Resist height measurement

Equipment: P-10 profilometer

Recipe: Measure step height of the resist across alignment marks

9. Descum

Equipment: Oxford 81 etcher

Recipe:Oxygen plasma clean on empty chamber, time = 10 minutes

Oxygen plasma clean recipe on sample, time = 9s

10. Oxide hard mask etch

Equipment: Oxford 100 etcher

Recipe: Oxygen plasma clean on blank Si wafer, time = 10 minutes

CHF_3O_2 oxide etch season on blank Si wafer for 3 minutes

CHF_3O_2 oxide etch on sample, time = 52 seconds

11. Metrology

Equipment : P-10 profilometer and Filmetrics

Recipe: Measure step height on P-10 profilometer and Oxide hard mask - silicon - buried oxide stack on filmetrics. Use measurements to determine if oxide hard mask is completely etched.

12. Resist strip

Equipment : Oxford 81

Recipe: Oxygen plasma clean on sample, time = 105s

13. Step height measurement

Equipment : P-10 profilometer

Recipe: Measure step height on P-10 profilometer after resist removal to obtain depth of over etch into silicon

14. Silicon device layer etch

Equipment : Plasmatherm PT 770

Recipe: Season on dummy silicon wafer using process flow ssridar.prc for 4 minutes

Etch sample using ssridar.prc for 50s

15. Metrology

Equipment : P-10 profilometer and Filmetrics

Recipe: Measure step height on P-10 profilometer and oxide hard mask - silicon - buried oxide stack on filmetrics. Use measurements to verify complete etch of silicon device layer.

16. Oxide hard mask removal

Equipment: Oxford 82 etcher

Recipe: Oxygen plasma clean, time = 10 minutes

CHF_3O_2 oxide etch season on dummy wafer for 3 minutes

CHF_3O_2 oxide etch on sample, time = 36s

17. Resist spin

Equipment : Photo resist spinners

Recipe: Spin SPR 220-3.0 photoresist with parameters:

Speed = 3000rpm, ramp = 1000 rpm/s, time = 30s

Hard bake at 115°C for 90s

18. Expose - ion implant mask

Equipment : ABM contact aligner

Recipe: Exposure time of 8s

Post exposure bake at 115°C for 90s

19. Develop

Equipment : General chemistry hoods

Recipe : 80s in 726MIF developer

20. Ion implantation

Equipment : Eaton Ion Implanter

Recipe : Boron ion implantation at 30keV, Dose = 2e15. Keep current low to prevent photoresist burning.

21. Resist strip

Equipment : General Chemistry hood

Recipe:10 mins acetone dip with ultrasonic agitation

5 minutes isopropyl alcohol dip

Rinse with DI H_2O

22. MOS clean

Equipment : MOS clean wet bench

Recipe: 10 minutes dip in 1:1:6 NH_4OH:H_2O_2:H_2O at 70°C

10 minutes dip in 1:1:6 HCl:H_2O_2:H_2O at 70°C

Rinse in DI H_2O

23. Furnace anneal

Equipment : MOS clean anneal furnace - B1

Recipe: Load sample at 800°C

5 minutes 900°C nitrogen anneal

Unload at 7% unload rate at 650°C

24. Surface clean/preparation

Equipment : Acid Chemical Hood

Recipe: 2 minutes dip in Nanostrip

Rinse in DI H_2O

Dehydration bake at 200°C for 5 minutes

25. LOR resist spin

Equipment : Photo resist spinners

Recipe: Spin LOR5A photoresist with parameters:

Speed = 500rpm, ramp = 1000 rpm/s, time = 10s

Speed = 3000rpm, ramp = 500 rpm/s, time = 50s

Hard bake at 170°C for 5 minutes

26. SPR 220-3.0 resist spin

Equipment : Photo resist spinners

Recipe: Spin SPR 220-3.0 photoresist with parameters:

Speed = 3000rpm, ramp = 1000 rpm/s, time = 30s

Hard bake at 115°C for 90s

27. Expose - metal mask

Equipment : ABM contact aligner

Recipe: Exposure time of 12s

Post exposure bake at 115°C for 90s

28. Develop

Equipment : General chemistry hoods

Recipe : 270s in 726MIF developer

29. Metal evaporation

Equipment : SC4500 odd-hour evaporator

Recipe : Evaporate 25nm nickel , followed by 25nm titanium and 50nm platinum, without exposing the sample to air between steps

30. Lift-off

Equipment : General chemistry hoods

Recipe: 20 mins acetone dip with ultrasonic agitation

5 minutes isopropyl alcohol dip

Rinse with DI H_2O

31. Furnace anneal

Equipment : MOS metal anneal furnace - C2

Recipe: Load sample at 400°C

30 minutes 400°C 5% H_2/N_2 anneal

Unload at 10% unload rate at 400°C

32. Surface preparation

Equipment : Acid Hood

Recipe: 30s dip in Buffered Oxide Etchant (BOE) 30:1

Rinse in DI H_2O

33. Vapor prime Equipment : HMDS Vapor Prime oven

Recipe: Standard HMDS vapor prime recipe

34. Resist spin

Equipment : Photo resist spinners

Recipe: Spin SPR 220-3.0 photoresist with parameters:

Speed = 3000rpm, ramp = 1000 rpm/s, time = 30s

Hard bake at 115°C for 90s

35. Expose - release mask

Equipment : ABM contact aligner

Recipe: Exposure time of 8s

Post exposure bake at 115°C for 90s

36. Develop

Equipment : General chemistry hoods

Recipe: 90s in 726MIF developer

37. Hard bake

Equipment : Photoresist/E-beam resist hotplates

Recipe: 20 minutes at 140°C

38. Timed release etch

Equipment : Acid hood

Recipe: 23 minutes 30 seconds in BOE 6:1

39. Resist strip and CPD preparation

Equipment : Base/solvent hood

Recipe:10 minutes dip in acetone for resist removal

5 minutes rinse in 1:1 isopropyl alcohol:DI H_2O

5 minutes rinse in isopropyl alcohol

40. Critical point drying Equipment : Critical point dryer

Recipe: Transfer samples to critical point dryer without exposing to air and run standard recipe

41. Atomic Layer Deposition (ALD) of alumina

Equipment: Oxford ALD FlexAL

Recipe: Season ALD chamber by running Al_2O_3 300° plasma recipe for 100 cycles

Al_2O_3 300° plasma recipe on sample for 400 cycles

42. Resist spray coating Equipment : Suss MicroTec Gamma cluster tool

Recipe: Spray coat 1:10 S1818:acetone to a thickness of 7μm using SidTallur_S1805_MEMS recipe.

43. Soft bake

Equipment : Photoresist/E-beam resist hotplates

Recipe: 60s at 90°C

44. Expose - metal mask (to remove ALD material from bond-pads)

Equipment : ABM contact aligner Recipe: Exposure time of 100s

45. Develop and Al_2O_3 etch

Equipment : General chemistry hoods

Recipe:6 minutes in 726MIF developer

2 minutes rinse in DI water

46. Resist strip and CPD preparation

Equipment : General chemistry hoods

Recipe:10 minutes dip in acetone for resist removal

5 minutes rinse in 1:1 isopropyl alcohol:DI H_2O

5 minutes rinse in isopropyl alcohol

47. Critical point drying Equipment : Critical point dryer

Recipe: Transfer samples to critical point dryer without exposing to air and run standard recipe

APPENDIX C

SIMULTANEOUS RADIATION PRESSURE INDUCED HEATING AND COOLING OF AN OPTO-MECHANICAL RESONATOR

The ultimate sensitivity of optical sensing of mechanical motion is fundamentally set by the Standard Quantum Limit (SQL) [106]. However, well before the SQL is reached, backaction forces may dominate and severely alter the dynamics of the intrinsic mechanical motion of the sensor. Due to a combination of large mechanical oscillations and necessary saturation of amplification, the noise floor of the opto-mechanical sensor increases, rendering it ineffective at transducing small signals. Parametric instability is predicted to be a potential problem in the context of the advanced Laser Interferometer Gravitational Observatory (LIGO) [116] and, more generally, in many cavity opto-mechanical systems designed for ultra-precise sensing. This can be controlled by designing elaborate feedback schemes [116, 106]. In this chapter, we demonstrate amplification of one mechanical resonance in a silicon nitride micro-mechanical ring resonator while simultaneously cooling another mechanical resonance by exploiting two closely spaced optical whispering gallery mode cavity resonances. The possibility of simultaneous heating and cooling can open up avenues in studying coherent phonon exchange and phonon dynamics between different acoustic modes, and be of interest in MEMS gyroscopes and studying aspects of condensed-matter and many-body physics at the macro-scale.

For this demonstration, we use the silicon nitride opto-mechanical resonator discussed in chapter 3. We probe the interaction between the optical and mechanical modes of the ring resonator using an avalanche photodetector to convert motion induced intensity modulation into RF signals as described in chapter 3. We choose an optical mode with an optical quality factor of $\approx$ 200,000 (and intrinsic

Q > 500,000) and the laser wavelength is fixed such that it corresponds to a 3dB drop in optical transmission off-resonance. At low input laser powers (5dBm), the input light coupled into the cavity is modulated by the Brownian noise motion of the mechanical modes of the micro-ring as shown in Figure C.1. The fundamental radial expansion mode of the micro-ring at a frequency of 41.97MHz causes strong intensity modulation of the laser light as compared to a group of azimuthal composite mechanical modes around 77MHz. This can be attributed to higher effective path length change associated with the radial expansion mode, which causes greater modulation of the laser light [28].

The fundamental radial expansion mode of the ring at 41.97MHz has mechanical Q $\approx$ 2,000 measured in air. As we increase the laser power, self-sustained oscillations are observed for this mode above the input threshold power as shown in Figure C.2. The sharp threshold behavior is characteristic of radiation pressure induced parametric instability [28]. Figures C.3 and C.4 show heating and cooling of this mechanical mode obtained by blue detuning and red detuning the laser with respect to the cavity respectively. The mechanical mode is heated by blue detuning the input laser light (1550.55nm) with respect to the cavity (1550.6nm). The linewidth of the peak narrows and the frequency increases, as expected for heating of the mechanical mode. When the laser is red detuned (1550.672nm) with respect to the cavity, the mechanical mode is cooled. The linewidth increases from 42.4kHz to 92.5kHz as the laser power is increased from 10dBm to 14dBm. This corresponds to an effective temperature of 138K. The effective temperature is inferred by the linewidth of the mechanical resonance [117].

Interaction of mechanical modes of nanomechanical resonators with multiple optical modes has been shown before [118], which enables both heating and cool-

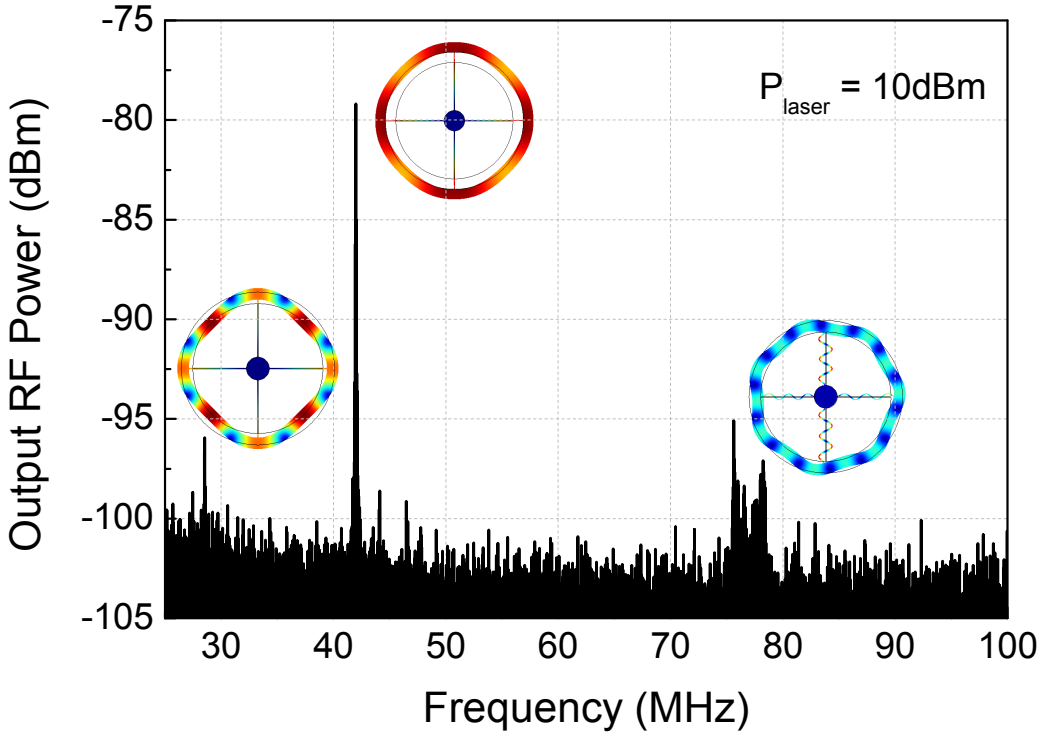

Figure C.1: RF spectrum at the output of the avalanche photodetector. The peaks observed correspond to the Brownian noise mechanical motion of the micro-ring. The fundamental radial expansion mode of the micro-ring at a frequency of 41.97MHz causes strong intensity modulation of the laser light as compared to a group of azimuthal composite mechanical modes around 77MHz. Finite element method (FEM) simulations of the mechanical mode shapes are shown as insets.

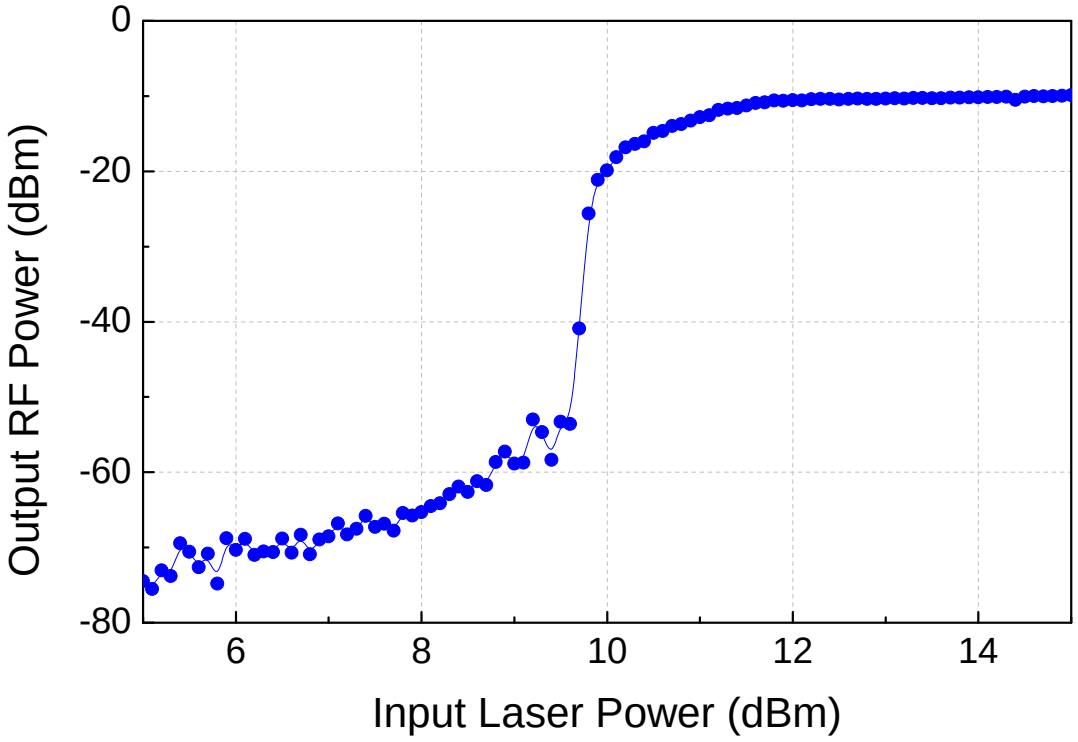

Figure C.2: Variation of RF power at the output of the photodetector with the input laser power, for the fundamental radial expansion mode of the micro-ring at 41.97MHz. As the laser power is increased, self-sustained oscillations are observed for this mode. The sharp threshold behavior shown is characteristic of radiation pressure induced parametric instability.

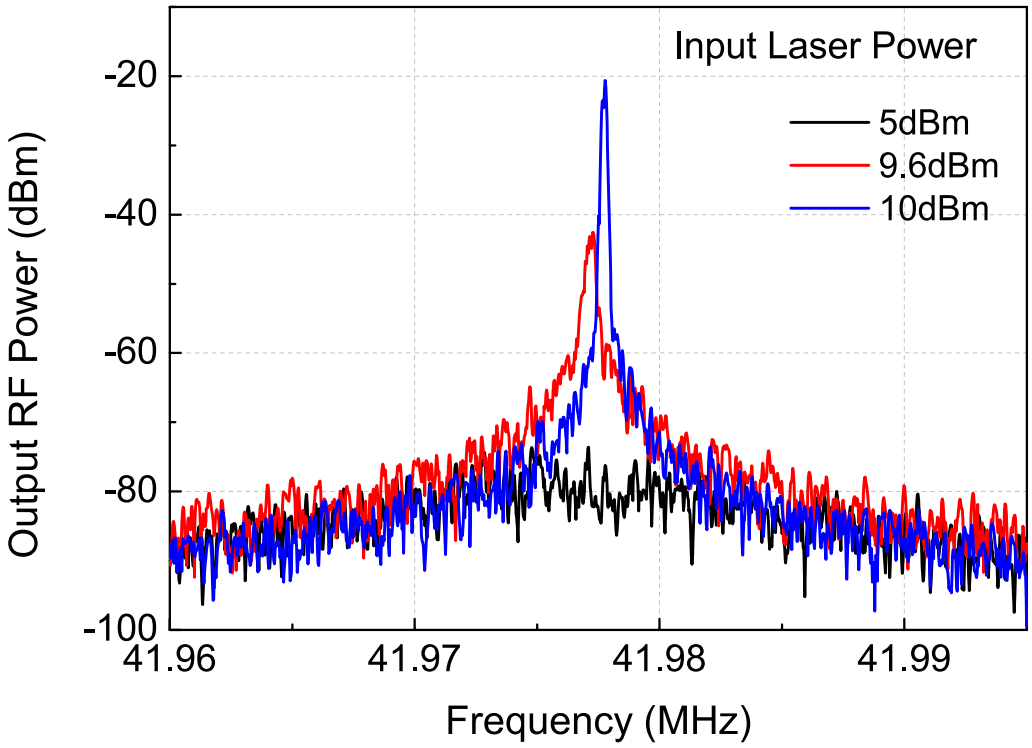

Figure C.3: The mechanical mode is heated by blue detuning the input laser light (1550.55nm) with respect to the cavity (1550.6nm). The linewidth of the peak narrows and the frequency increases (blue curve), as expected for heating of the mechanical mode.

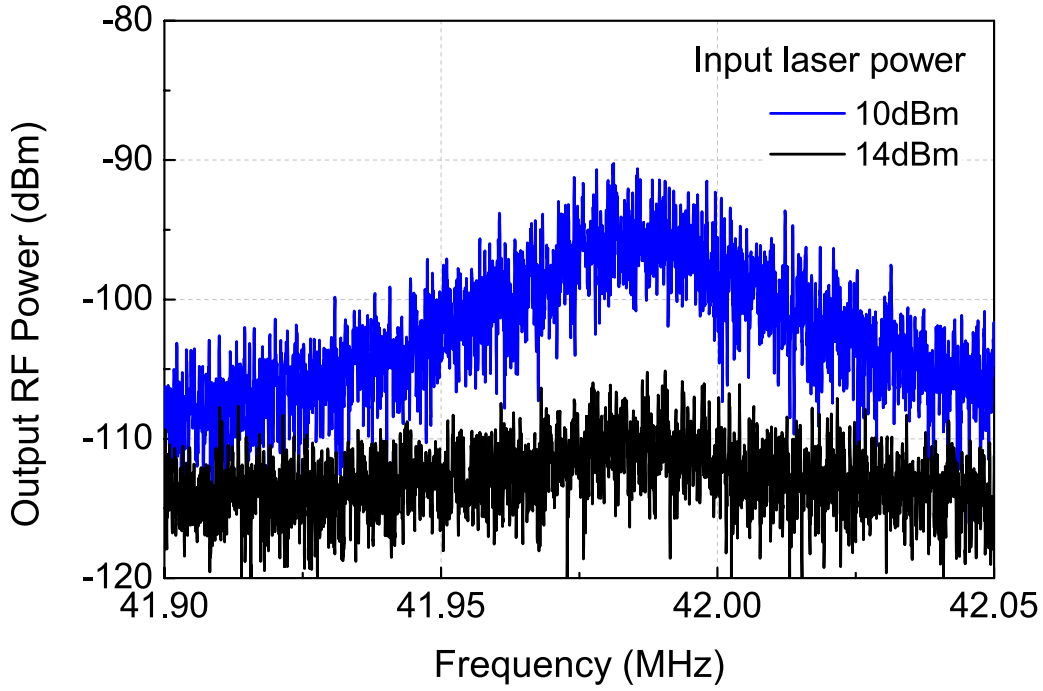

Figure C.4: When the laser is red detuned (1550.672nm) with respect to the cavity, the mechanical mode is cooled. The linewidth increases from 42.4kHz to 92.5kHz as the laser power is increased from 10dBm (blue curve) to 14dBm (black curve). This corresponds to an effective temperature of 138K.

ing. However, this scheme causes either heating or cooling of the mechanical mode, depending on which optical resonance is pumped. Here we explore the feasibility of using two closely spaced whispering gallery modes to simultaneously achieve heating of one mechanical mode while cooling another mechanical mode using a single pump laser. The micro-ring resonator heats up due to thermal absorption as the laser power is increased, which leads to the characteristic shark fin optical spectrum [119] owing to temperature dependence of the modal refractive index. Due to the rich mode spectrum of a silicon nitride micro-ring resonator, situations may arise where the resonator has multiple optical mode families. The modal refractive indices of these mode families may have different temperature dependence. As shown in Figure C.5, one of the optical modes is far more sensitive to the laser power. As such, it is possible to fix the laser wavelength such that the pump laser light is red detuned with respect to one of the cavity modes and blue detuned with respect to the other in thermal equilibrium [119].

Figure C.6 shows increased RF power for the Brownian noise motion peaks when the laser power is increased. The laser light (1550.55nm) is blue detuned with respect to the pair of optical resonances at 1550.6nm. Figure C.7 shows the RF spectrum when the laser (1550.587nm) is blue detuned with respect to one optical resonance and red detuned with respect to the other. In this case, the fundamental radial mode of vibration is heated as the pump laser power is increased while a group of azimuthal composite mechanical modes is cooled. Figure C.8 shows the cooling of these modes more clearly, with the linewidth for the mode at 76.7MHz increasing from 150kHz to 250kHz as the laser power is increased from 10dBm to 11dBm. This corresponds to an effective temperature of 180K.

The possibility of simultaneous heating and cooling of mechanical modes can

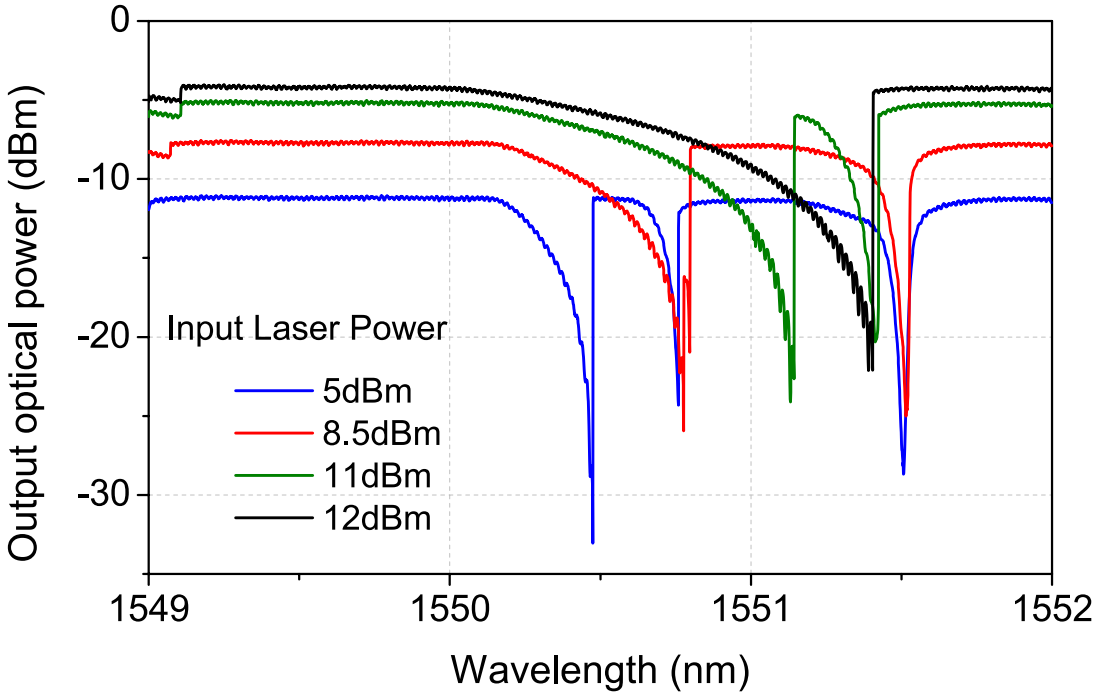

Figure C.5: Optical spectrum of the silicon nitride opto-mechanical resonator for different input laser powers. The modal refractive indices of multiple optical mode families have different temperature dependence. The shark-fin shape of the optical resonances is attributed to thermal absorption.

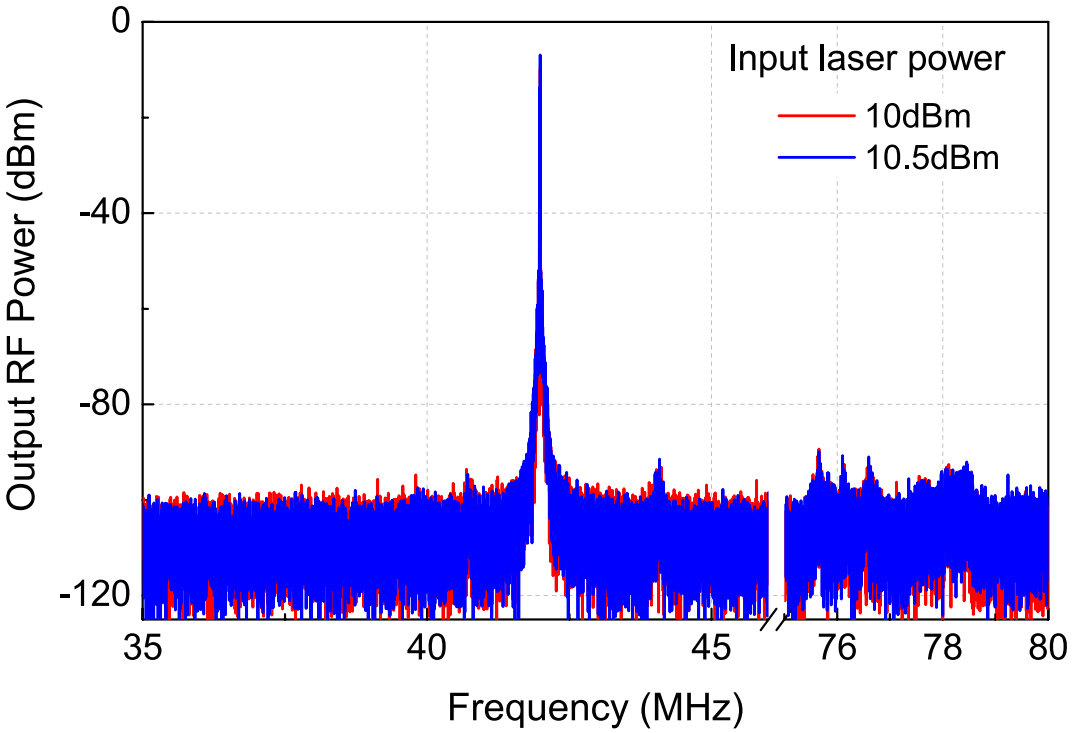

Figure C.6: When the laser light (1550.55nm) is blue detuned with respect to the pair of optical resonances around 1550.6nm, the RF power for the Brownian noise motion peaks when the laser power is raised from 10dBm (red curve) to 10.5dBm (blue curve).

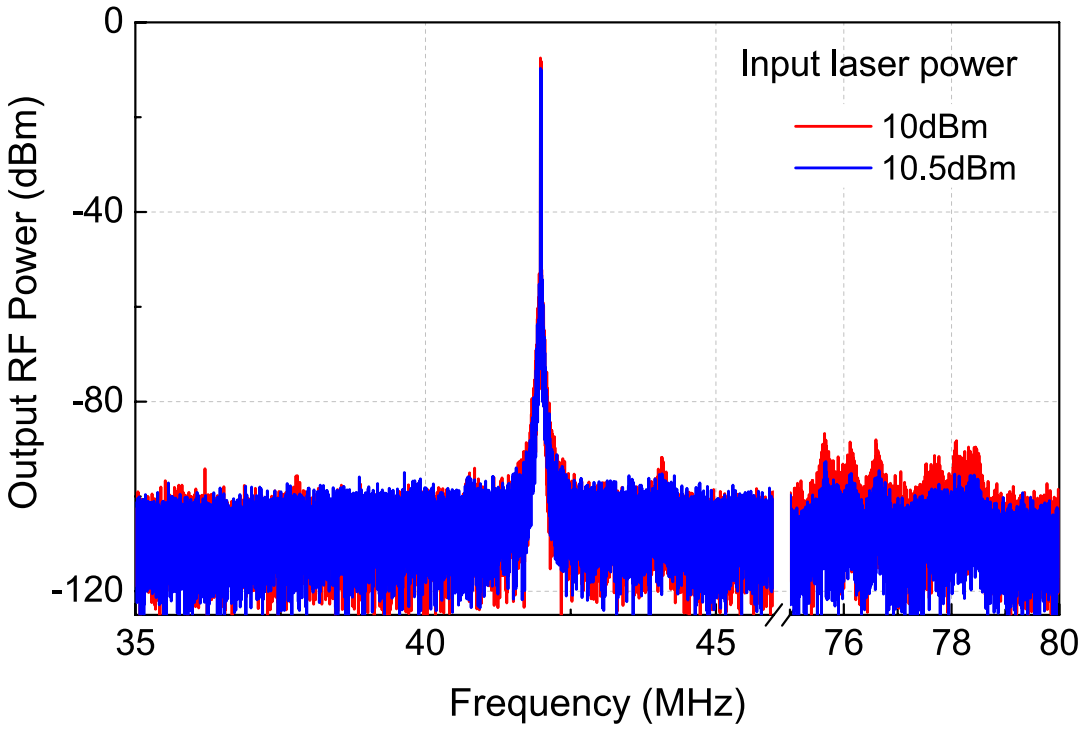

Figure C.7: RF spectrum when the laser (1550.587nm) is blue detuned with respect to one optical resonance and red detuned with respect to the other. In this case, the fundamental radial mode of vibration at 41.97MHz is heated as the pump laser power is increased from 10dBm (red curve) to 10.5dBm (blue curve), while a group of azimuthal composite mechanical modes centered around 77MHz is cooled.

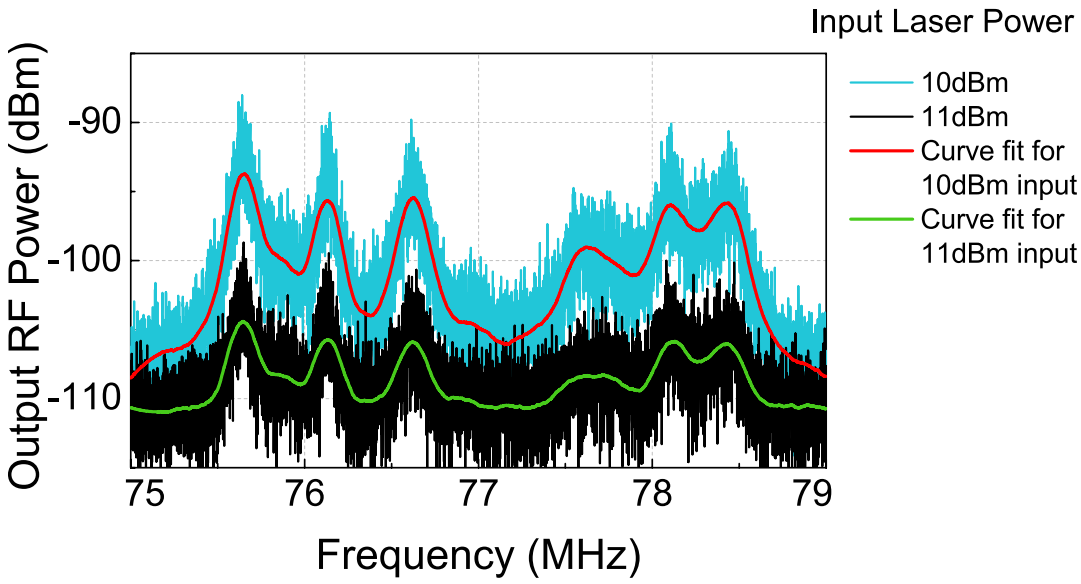

Figure C.8: Increasing the laser input power from 10dBm (blue curve) to 11dBm (black curve) results in cooling of the composite mechanical modes of the resonator. For instance, the linewidth of the mode at 76.7MHz increases from 150kHz to 250kHz by increasing the laser power. This corresponds to an effective temperature of 180K. The red and green curves are smoothed curve fits for the blue and black curves respectively.

open up avenues in studying coherent phonon exchange and phonon dynamics between different acoustic modes, mediated by an optical media and enable significant advances in ultra-precise sensing. Mode-matched MEMS gyroscopes simultaneously require high Q along the drive and sense axis for improved sensitivity. However the high Q along sense axis reduces the effective bandwidth of the sensor. Simultaenously heating (to achieve narrow linewidths along the drive axis) and cooling (maintaining high signal to noise ratio (SNR) while increasing bandwidth) promises high sensitivity and high resolution, while maintaining large bandwidth and high dynamic range. Cooling multiple closely spaced mechanical modes to groundstate will also provide an exciting toolset for studying aspects of condensed-matter and many-body physics at the macro-scale.

APPENDIX D

ANALYTICAL MODEL FOR MOTIONAL IMPEDANCE IN PARTIAL GAP TRANSDUCTION

Assumptions

This chapter presents an analytical treatment of this problem, and insights derived from the equations presented here enable the designer to optimize resonator designs for low motional impedances. The model presented here makes several assumptions to simplify the derivation. Consider a schematic of a beam resonator shown in Figre D.1 for illustration. The resonator body comprises of a resonator body of length L and dielectric of length d_2 at both ends. The air gap is d_1 and the dielectric on the electrode has length d_e. The dielectric constant of the dielectric is ϵ_2 and that of air is ϵ_1. The various assumptions made are:

1. No acoustic mismatch between dielectric and resonator body
2. Dielectric on the electrode is rigid
3. Expressions for electrostatic forces are independent of the mode shape
4. Sense current calculation requires:
   (a) Accounting for both displacement in x (motion at the free end) and displacement in y (motion at the interface between resonator and dielectric)
   (b) Expressing x displacement in terms of y displacement.

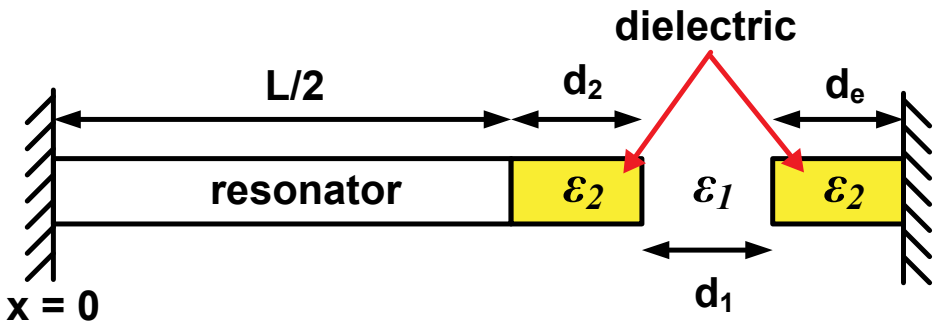

Figure D.1: Schematic highlighting half the resonator geometry for a beam resonator for illustrating model assumptions and methodology.

Methodology

The model essentially follows the derivation for motional impedance presented in [73]. As listed in steps 4-5 below, we need to also account for motion at the resonator-dielectric interface and air-dielectric interface.

1. Write down the equation for mode shape in the resonator assuming no acoustic mismatch
2. Express total capacitance between electrode and resonator body (dielectric and air gap combination) in terms of displacements.
3. Express forces in the form $F_i = \frac{V^2}{2}\frac{\partial C_{tot}}{\partial x_i}$ where V is the total applied voltage, C_{tot} is the total capacitance and x_i is the corresponding displacement
4. Write down displacement amplitude, and hence the velocity amplitude at the free end of the resonator in terms of effective force (sum of individual forces shaped by the mode shape), stiffness and the quality factor
5. Use these expressions to write down sense current as $i_{sense} = V_{dc}\frac{\partial C_{tot}}{\partial t} = V_{dc}\frac{\partial C_{tot}}{\partial gap}\frac{\partial gap}{\partial t}$, where V_{dc} is the DC bias applied across the resonator

6. Express the motional resistance R_x in terms of the applied RF voltage v_{ac} as $R_x = \frac{v_{ac}}{i_{sense}}$
7. Comparing the expression for effective force from step 4 with $F_{net} = \eta v_{ac}$, find the effective electromechanical transduction factor η
8. Expressions for the inductance and capacitance are given by $L_x = \frac{M}{\eta^2}, C_x = \frac{\eta^2}{K}$, where M is the effective mass and K is the stiffness of the mechanical resonator

Equations for a beam resonator

The equations for a beam resonator can be obtained by following the methodology presented above. For the schematic presented in fig. 1, the mode shape can be written as in equation D.1, where U_0 is the amplitude of displacement, $k_n = \frac{(2n+1)\pi}{L+2d_2}$ $(n = 1, 2, 3, ...)$ is the wave number and Ω is the angular mechanical resonance frequency.

$$u(x) = U_0 sin\left(k_n x\right) e^{j\Omega t} \tag{D.1}$$

The total capacitance, C_{tot} can be written as

$$C_{tot} = \frac{\epsilon_2 \epsilon_1 A}{\epsilon_1 d_e + \epsilon_2 \left(d_1 + d_2\right) + x\left(\epsilon_1 - \epsilon_2\right) - \epsilon_1 y} \tag{D.2}$$

where A is the cross sectional area across the capacitor plates. The forces acting on the resonator-dielectric and air-dielectric interfaces can be written as follows, where V is the voltage applied at the electrode. For our purposes we use expressions obtained by substituting $x = d_2$ and $y = 0$. Moreover, we have $\frac{V^2}{2} = V_{dc} v_{ac}$.

$$F_1 = \frac{V^2}{2}\frac{\partial C_{tot}}{\partial y} = \frac{V^2}{2}\frac{\epsilon_2\epsilon_1^2 A}{\left[\epsilon_1 d_e + \epsilon_2\left(d_1+d_2\right) + x\left(\epsilon_1-\epsilon_2\right) - \epsilon_1 y\right]^2} \tag{D.3}$$

$$F_2 = \frac{V^2}{2}\frac{\partial C_{tot}}{\partial x} = -\frac{V^2}{2}\frac{\epsilon_2\epsilon_1 A\left(\epsilon_1-\epsilon_2\right)}{\left[\epsilon_1 d_e + \epsilon_2\left(d_1+d_2\right) + x\left(\epsilon_1-\epsilon_2\right) - \epsilon_1 y\right]^2} \tag{D.4}$$

$$F_{net} = F_1 sin\left(\frac{k_n L}{2}\right) + F_2 \tag{D.5}$$

The expression for displacement can be written down as in equations D.6 and D.7 using the expression for stiffness (K) from [72].

$$U_0 = \frac{F}{|b\Omega_0|} = \frac{F}{|m\Omega_0^2/Q|} = \frac{FQ}{K} \tag{D.6}$$

$$\Rightarrow U_0 = \frac{2Q\left(L+2d_2\right)}{Y(2n+1)^2\pi^2}\frac{\epsilon_1\epsilon_2 V_{dc} v_{ac}\left[\epsilon_1 sin\left(\frac{k_n L}{2}\right) - \left(\epsilon_1-\epsilon_2\right)\right]}{\left[\epsilon_2 d_1 + \epsilon_1 d_2 + \epsilon_1 d_e\right]^2} \tag{D.7}$$

Then the sense current can be written as

$$i_{sense} = V_{dc}\frac{\partial C_{tot}}{\partial t} = V_{dc}\frac{\partial C_{tot}}{\partial gap}\frac{\partial gap}{\partial t} = V_{dc}\frac{\partial C_{tot}}{\partial y}\frac{\partial y}{\partial t} \tag{D.8}$$

While carrying out this derivation, we should express x in terms of y. The reason for this is that motion at the free end also contributes to the sense current which would not be captured if we only carry out a partial differentiation of C_{tot} with y.

$$x = d_2 + \frac{y}{sin\left(\frac{k_n L}{2}\right)}, \frac{\partial y}{\partial t} = 2\pi f_n U_0 sin\left(\frac{k_n L}{2}\right) \tag{D.9}$$

Thus we can get an expression for $R_x = \frac{v_{ac}}{i_{sense}}$ as follows:

$$R_x = \frac{v_{ac}}{i_{sense}} = \frac{(2n+1)\pi\sqrt{Y\rho}}{2QV_{dc}^2\epsilon_1^2\epsilon_2^2 A} \frac{\left[\epsilon_2 d_1 + \epsilon_1 d_2 + \epsilon_1 d_e\right]^4}{\left[\epsilon_1 sin\left(\frac{k_n L}{2}\right) - (\epsilon_1 - \epsilon_2)\right]^2} \tag{D.10}$$

We can obtain η from equation D.5, and thus express L_x and C_x as follows:

$$L_x = \frac{v_{ac}}{i_{sense}} = \frac{\rho\left(L + 2d_2\right)}{V_{dc}^2\epsilon_1^2\epsilon_2^2 A} \frac{\left[\epsilon_2 d_1 + \epsilon_1 d_2 + \epsilon_1 d_e\right]^4}{\left[\epsilon_1 sin\left(\frac{k_n L}{2}\right) - (\epsilon_1 - \epsilon_2)\right]^2} \tag{D.11}$$

$$C_x = \frac{v_{ac}}{i_{sense}} = \frac{2V_{dc}^2\epsilon_1^2\epsilon_2^2 A\left(L + 2d_2\right)}{Y\pi^2(2n+1)^2} \frac{\left[\epsilon_1 sin\left(\frac{k_n L}{2}\right) - (\epsilon_1 - \epsilon_2)\right]^2}{\left[\epsilon_2 d_1 + \epsilon_1 d_2 + \epsilon_1 d_e\right]^4} \tag{D.12}$$

To establish the validity of this model, let us consider the case for air gap transduction with zero ALD material deposition. In this case, equation D.10 reduces to

$$R_x = \frac{v_{ac}}{i_{sense}} = \frac{(2n+1)\pi d_1^4\sqrt{Y\rho}}{2QV_{dc}^2\epsilon_1^2 A} \tag{D.13}$$

which exactly matches the well established analytical expression for conventional air gap transduction [73]. Similarly, for the case of internal dielectric transduction, where the gap is completely filled with the ALD material, we obtain the following expression for R_x:

$$R_x = \frac{v_{ac}}{i_{sense}} = \frac{\pi\left(d_2 + d_e\right)^4\sqrt{Y\rho}}{2QV_{dc}^2\epsilon_2^2 A\left[sin\left(\frac{k_0 L}{2}\right)\right]^2} \tag{D.14}$$

This expression also matches the equation for the fundamental mode for internal dielectric transduced resonators in literature [72]. Thus our model serves

as a bridge between the two well established models for air gap transduction and internal dielectric transduction.

Equations for a disk resonator

Beam resonators have significant mode distortion at the resonator-electrode interface [71] that are not accounted for in this model. However, we can establish the validity of this model by deriving a similar set of equations for disk resonators which do not have mode distortion.

Consider the disk resonator geometry in Figure D.2. The mode shape for disk resonators can be written as follows, where $k_0 = \Omega_0 (R + d_2) \sqrt{\frac{\rho(1-\nu^2)}{E}}$ [13]:

$$u(r) = A \frac{k_0}{R} J_1 \left(\frac{k_0 r}{R} \right) e^{j\Omega t} \tag{D.15}$$

The total capacitance can be written as follows (t denotes thickness of the device layer):

$$C_{tot} = \frac{t}{\frac{1}{\theta\epsilon_2} log_e \left(\frac{r+d_2+d_1+d_e}{R+d_2+d_1} \right) + \frac{1}{\theta\epsilon_1} log_e \left(\frac{R+d_2+d_1}{R+d_2+x} \right) + \frac{1}{2\pi\epsilon_2} log_e \left(\frac{R+d_2+x}{R+y} \right)} \tag{D.16}$$

One can derive the stiffness (and hence effective mass) from the modeling presented in [31]

$$K = \pi \rho t (R + d_2)^2 \Omega_0^2 \frac{J_2^2 (k_0)}{J_1 (k_0)} \tag{D.17}$$

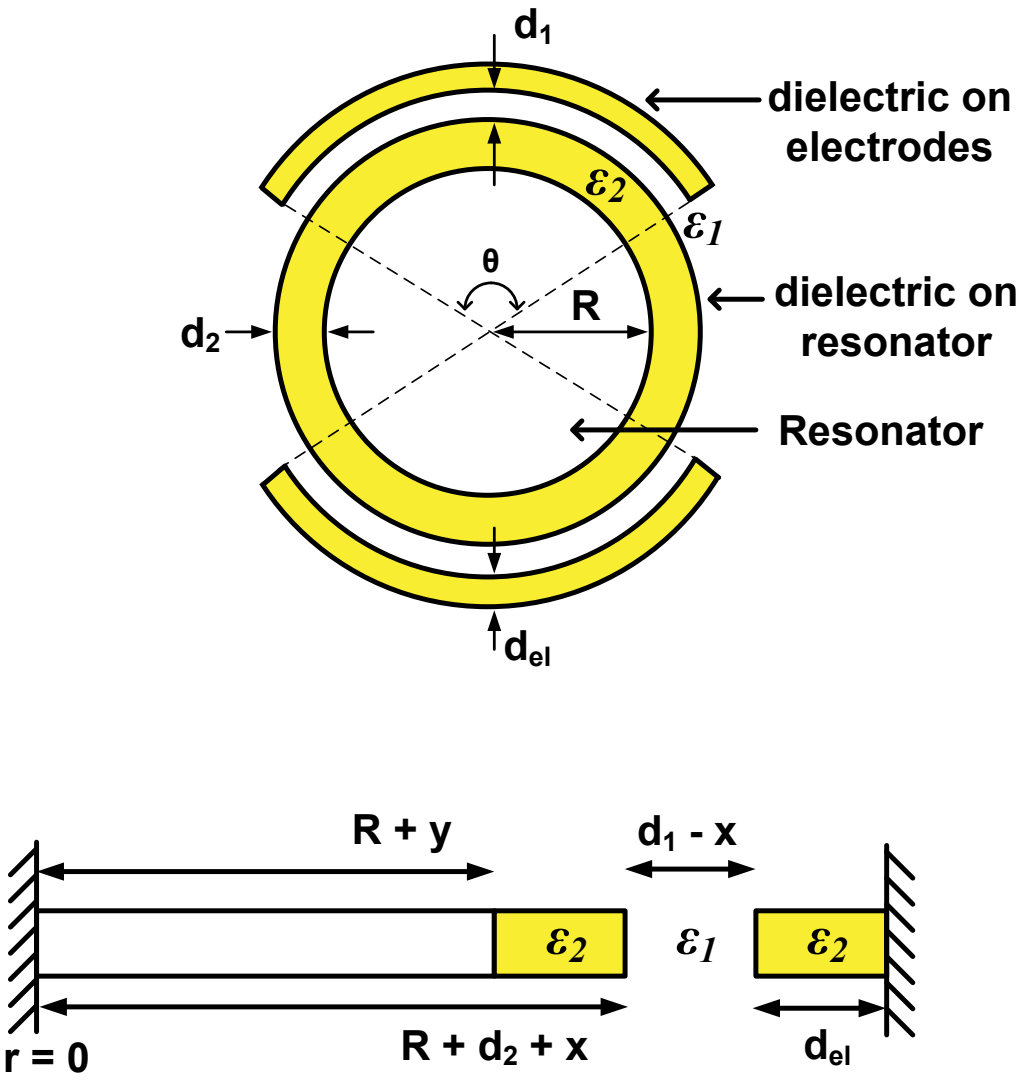

Figure D.2: Schematic for a partial gap disk resonator highlighting (top) the geometry, (bottom) displacements at various interfaces

The forces and hence the effective force can be written down following the same methodology for a beam resonator as follows:

$$F_{1_{y=x=0}} = \frac{V^2}{2}\frac{\partial C_{tot}}{\partial y} = V_{dc} v_{ac} \frac{\partial C_{tot}}{\partial y} \tag{D.18}$$

$$F_{2_{y=x=0}} = \frac{V^2}{2}\frac{\partial C_{tot}}{\partial x} = V_{dc} v_{ac} \frac{\partial C_{tot}}{\partial x} \tag{D.19}$$

$$F_{net} = \frac{F_1 J_1\left(\frac{k_0 R}{R+d_2}\right)}{J_1\left(k_0\right)} + F_2 \tag{D.20}$$

The sense current and displacement terms can similarly be obtained:

$$i_{sense} = V_{dc}\frac{\partial C_{tot}}{\partial y}\frac{\partial y}{\partial t} \tag{D.21}$$

$$x = \frac{y J_1\left(k_0\right)}{J_1\left(\frac{k_0 R}{R+d_2}\right)}, \frac{\partial y}{\partial t} = \Omega_0 U_0 \frac{J_1\left(\frac{k_0 R}{R+d_2}\right)}{J_1\left(k_0\right)} \tag{D.22}$$

Thus we obtain following expressions for R_x, L_x and C_x:

$$R_x = \frac{\pi \rho t \left(R+d_2\right)^2 \Omega_0 J_2^2\left(k_0\right)}{Q V_{dc}^2 J_1\left(\frac{k_0 R}{R+d_2}\right)\left[\frac{J_1\left(\frac{k_0 R}{R+d_2}\right)}{J_1(k_0)}\frac{\partial C_{tot}}{\partial y} + \frac{\partial C_{tot}}{\partial x}\right]_{x=y=0}\left[\frac{\partial C_{tot}}{\partial y}\right]_{x=\frac{y J_1(k_0)}{J_1\left(\frac{k_0 R}{R+d_2}\right)}, x=y=0}} \tag{D.23}$$

$$L_x = \frac{\pi \rho t \left(R+d_2\right)^2 J_2^2\left(k_0\right)}{J_1\left(k_0\right)\left(V_{dc}\left[\frac{J_1\left(\frac{k_0 R}{R+d_2}\right)}{J_1(k_0)}\frac{\partial C_{tot}}{\partial y} + \frac{\partial C_{tot}}{\partial x}\right]_{x=0,y=0}\right)^2} \tag{D.24}$$

$$C_x = \frac{J_1(k_0)\left(V_{dc}\left[\frac{J_1\left(\frac{k_0 R}{R+d_2}\right)}{J_1(k_0)}\frac{\partial C_{tot}}{\partial y} + \frac{\partial C_{tot}}{\partial x}\right]_{x=0,y=0}\right)^2}{\pi\rho t\left(R+d_2\right)^2\Omega_0^2 J_2^2(k_0)} \tag{D.25}$$

Using the equations and methodology developed here, one can choose a suitable high dielectric constant (ϵ_2) ALD material and deposition thickness (d_2, d_e) to lower the motional resistance for capacitive air gap transduction. For a more realistic model, there are many additional factors to be considered for the case of partial air gap transduced resonators, such as motion of the dielectric, acoustic mismatch between the dielectric and resonator body, stress in the resonator, to name a few.

APPENDIX E

RAYLEIGH SCATTERING ENHANCED DISPLACEMENT SENSITIVITY AT BEYOND GHZ FREQUENCIES

For transduction of signals with mechanical frequencies in the resolved sideband regime using a singlet WGM optical resonance, we see in Figure E.1, that both the Stokes and anti-Stokes motional sidebands lie outside the optical cavity and hence the component of the intra-cavity energy at the mechanical resonance frequency is diminished, as compared to transduction of signals in the unresolved sideband regime. To counter this inefficiency, we explore the possibility of exploiting Rayleigh scattering induced optical mode splitting in optical whispering gallery mode (WGM) resonators [120] to transduce signals in the resolved sideband regime more efficiently, by using the optical mode doublet to boost the Stokes sideband. Consider the case of an opto-mechanical transducer sensed using modulation of CW laser light coupled to a back-scattering induced doublet optical resonance instead of a single optical WGM resonance as shown in Figure E.1.

E.1 Theoretical Formulation

Back-scattering centers in the resonator cause the degeneracy of the clockwise (CW) and the counter clockwise propagating modes to be lifted and lead to splitting of the otherwise originally degenerate optical modes [120, 121, 122]. The coupling of the two modes is quantified in terms of a coupling quality factor Q_u. The transmission equation for the single optical resonance in equation 2.12 now transforms to the following owing to the mode splitting [123]:

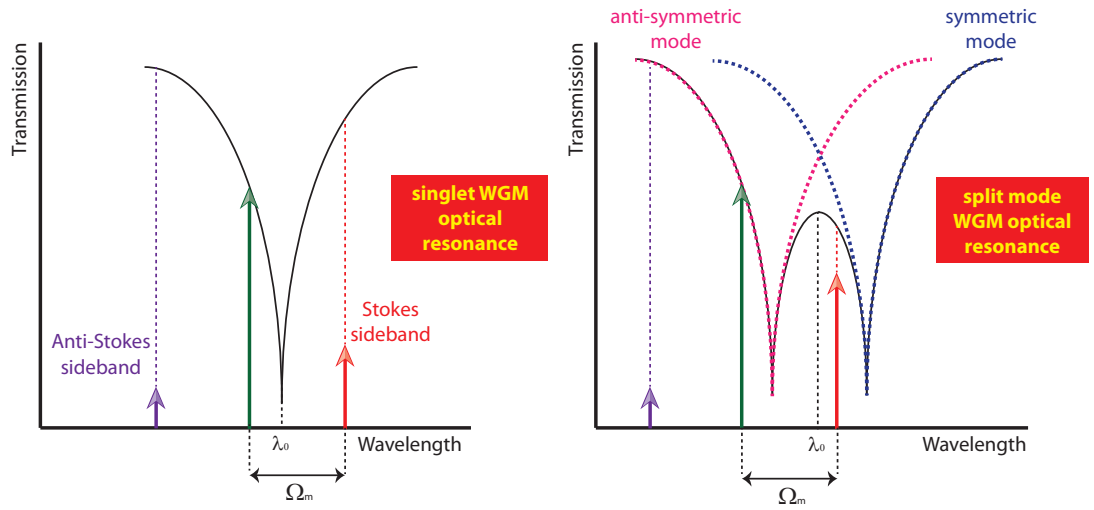

Figure E.1: Illustration of Rayleigh scattering induced optical mode splitting for enhancement of transduction efficiency of the optical sense scheme. The Stokes sideband amplitude is boosted by the presence of the second optical resonance as seen in the right panel.

$$T(\omega) = \left| 1 - \frac{1}{2Q_{ext}} \left(\frac{1}{j\left(\delta + \frac{1}{2Q_u}\right) + \frac{1}{2Q_{int}} + \frac{1}{2Q_{ext}}} + \frac{1}{j\left(\delta - \frac{1}{2Q_u}\right) + \frac{1}{2Q_{int}} + \frac{1}{2Q_{ext}}} \right) \right|^2 \tag{E.1}$$

Following a coupled mode approach, the mean field amplitudes of the coupled CW and CCW modes may be written in terms of the input field, $\overline{s}$ as follows [122] (see Figure E.2):

$$\overline{a}_{CW} = \overline{s}\sqrt{\Gamma_{ext}} \frac{j\Delta - \frac{\Gamma_{tot}}{2}}{\Delta^2 - \frac{\Gamma_{tot}^2}{4} - \frac{\gamma^2}{4} + j\Delta\Gamma_{tot}} \tag{E.2}$$

$$\overline{a}_{CCW} = \frac{-j\frac{\gamma}{2}}{j\Delta - \frac{\Gamma_{tot}}{2}} \overline{a}_{CW} \tag{E.3}$$

Here we assume that only the clockwise mode is pumped by the input field.

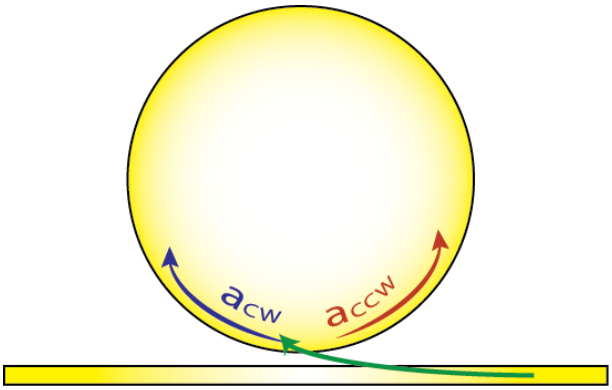

Figure E.2: Illustration of clockwise (CW) and counter-clockwise (CCW) propagating optical modes

This is in turn coupled to the counterclockwise mode via the scattering rate γ. Γ_{ext} is the decay rate associated with coupling of photons to the optical cavity and Γ_{tot} is the loaded cavity photon decay rate. The detuning Δ is specified for the originally degenerate optical mode, with optical resonance frequency ω_{opt}. We also assume that γ and Γ_{tot} are the same for both optical modes. The CW mode is coupled to the output field via $\overline{s}_{out} = \overline{s} - \overline{a}_{CW}\sqrt{\Gamma_{ext}}$. The coupling of the CW and CCW modes leads to formation of a mode doublet, which can be transformed into a pair of symmetric and antisymmetric modes [118], $\widehat{b}_1 = \frac{\overline{a}_{CW}+\overline{a}_{CCW}}{\sqrt{\Gamma_{ext}}}$ and $\widehat{b}_2 = \frac{\overline{a}_{CW}-\overline{a}_{CCW}}{\sqrt{\Gamma_{ext}}}$, representing the lower and higher frequency modes respectively. The frequencies of these modes are $\omega_1 = \omega_{opt} - \frac{\omega_{opt}}{2Q_u}$ and $\omega_2 = \omega_{opt} + \frac{\omega_{opt}}{2Q_u}$ respectively. Thus, the detuning values of the input laser line with respect to these two modes are $\Delta_1 = \Delta + \frac{\omega_{opt}}{2Q_u}$ and $\Delta_2 = \Delta - \frac{\omega_{opt}}{2Q_u}$ respectively.

Following the derivations in [32, 118], we can write down the intra-cavity field values for $\widehat{b}_1$ and $\widehat{b}_2$ in presence of mechanical motion $x(t) = x_0 sin(\Omega_m t)$, which corresponds to modulation index $\beta = \frac{x_0}{R}\frac{\omega_{opt}}{\Omega_m}$:

$$\widehat{b}_{1,intra} = \overline{s}\frac{\sqrt{\Gamma_{ext}}\left[j\Delta + \frac{\Gamma_{tot}}{2}\right]\left[j\left(\Delta + \frac{\gamma}{2}\right) + \frac{\Gamma_{tot}}{2}\right]}{\Delta^2 - \frac{\Gamma_{tot}^2}{4} - \frac{\gamma^2}{4} + j\Delta\Gamma_{tot}} \sum_{n=-\infty}^{+\infty} \frac{(-i)^n J_n(\beta_1)}{\frac{\Gamma_{tot}}{2} + j\left(\Delta_1 + n\Omega_m\right)} e^{j[(\omega_{opt}+n\Omega_m)t+\beta_1 cos(\Omega_m t)]} \quad \text{(E.4)}$$

$$\widehat{b}_{2,intra} = \overline{s}\frac{\sqrt{\Gamma_{ext}}\left[j\Delta + \frac{\Gamma_{tot}}{2}\right]\left[j\left(\Delta + \frac{\gamma}{2}\right) + \frac{\Gamma_{tot}}{2}\right]}{\Delta^2 - \frac{\Gamma_{tot}^2}{4} - \frac{\gamma^2}{4} + j\Delta\Gamma_{tot}} \sum_{n=-\infty}^{+\infty} \frac{(-i)^n J_n(\beta_2)}{\frac{\Gamma_{tot}}{2} + j\left(\Delta_2 + n\Omega_m\right)} e^{j[(\omega_{opt}+n\Omega_m)t+\beta_2 cos(\Omega_m t)]} \quad \text{(E.5)}$$

The total intra-cavity energy is given by $|\overline{a}_{CW}|^2 + |\overline{a}_{CCW}|^2$. In Figure E.3, we plot the total intra-cavity energy in the case of an optical doublet, and compare it to $\left|\widehat{b}_{2,intra}\right|^2$ to get an idea of the net improvement contributed by presence of the other optical resonance, $\widehat{b}_1$. We assume Δ = 11GHz, Q_{tot} = 70,000, Q_{ext} = 50,000, Q_u = 20,000, λ_{opt} = 1,564nm, x_0 = 6.75pm, R = 9.5μm. The frequency separation between the two optical modes in this case is 9.59GHz. We can clearly see the large boost in intra-cavity energy provided by the optical doublet for the Stokes sideband for the case where the mechanical frequency assumed is 8GHz.

E.2 Experimental Characterization

We identify a split optical resonance and a singlet optical resonance in our 2 coupled ring silicon acousto-optic modulator. Figures E.4 (a) and (b) show transmission spectra for the optical modes. To test the validity of this theory, we study the electro-mechanical transmission using the doublet resonance at 1,556.9nm and the

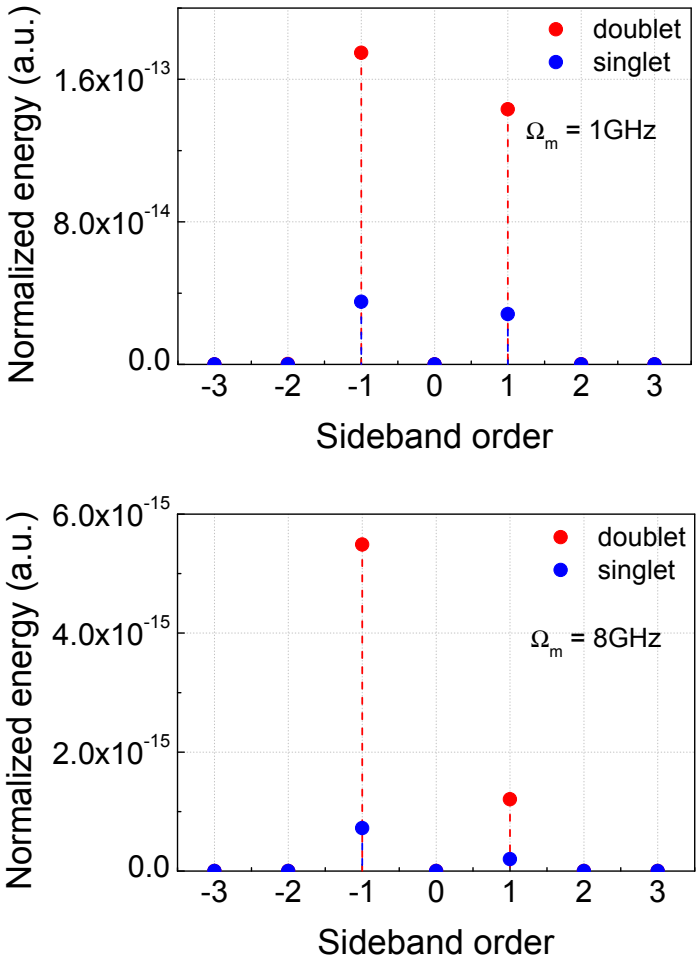

Figure E.3: Comparison of sideband amplitudes normalized to pump energy for two mechanical modes at 1GHz and 8GHz in case of singlet and doublet resonances. The frequency separation between the two optical modes in this case is 9.59GHz. We can clearly see the large boost in intra-cavity energy provided by the optical doublet for the Stokes sideband for the case where the mechanical frequency assumed is 8GHz. The pump laser line (sideband order = 0) is suppressed for easy visualization.

singlet resonance at 1,561nm. The frequency difference between the two resonances in the optical doublet is 9.63GHz.

As we clearly see in Figure E.5, the doublet resonance boosts the transduction of signals at higher frequencies (5GHz - 10GHz) owing to the second optical resonance. The enhancement is most pronounced at 5.25GHz and 8.2GHz, where the insertion loss improves by 25dB and 14dB respectively. Also, it enables us to observe signals at frequencies all the way up to 9.1GHz and 9.8GHz, which are not possible using the singlet optical resonance.

Next we examine this coupled resonator system following the partial gap process flow to improve the electrostatic drive transduction efficiency. This process is used to reduce the resonator electrode gap from 130nm to 50nm via ALD alumina (Al_2O_3). We identify an optical doublet resonance in this device with a frequency splitting of 3.86GHz (see Figure E.6).

Figure E.7 shows a comparison of the electromechanical transmission spectra recorded in this device using the doublet resonance, in comparison to transduction using a singlet resonance with loaded optical quality factor ≈60,000.

Comparing this to Figure E.5, it is easy to observe the larger signal strengths recorded using a doublet resonance in combination with partial gap transduction. The resonator thickness prior to ALD is 220nm. Depositing 40nm ALD alumina on all surfaces of the resonator predominantly changes the thickness, thereby changing the effective mass of the mechanical mode m_{eff} and hence the mechanical resonance frequency $\left(\Omega_{mech} \propto \sqrt{\frac{1}{m_{eff}}}\right)$. Thus, the resonance frequencies are roughly expected to lower by a factor of $\sqrt{\frac{\rho_{Si}*220}{\rho_{Si}*220+\rho_{Al_2O_3}*80}} \approx 0.83$. We experimentally observe a shift in the mechanical resonance frequencies for the radial mode family

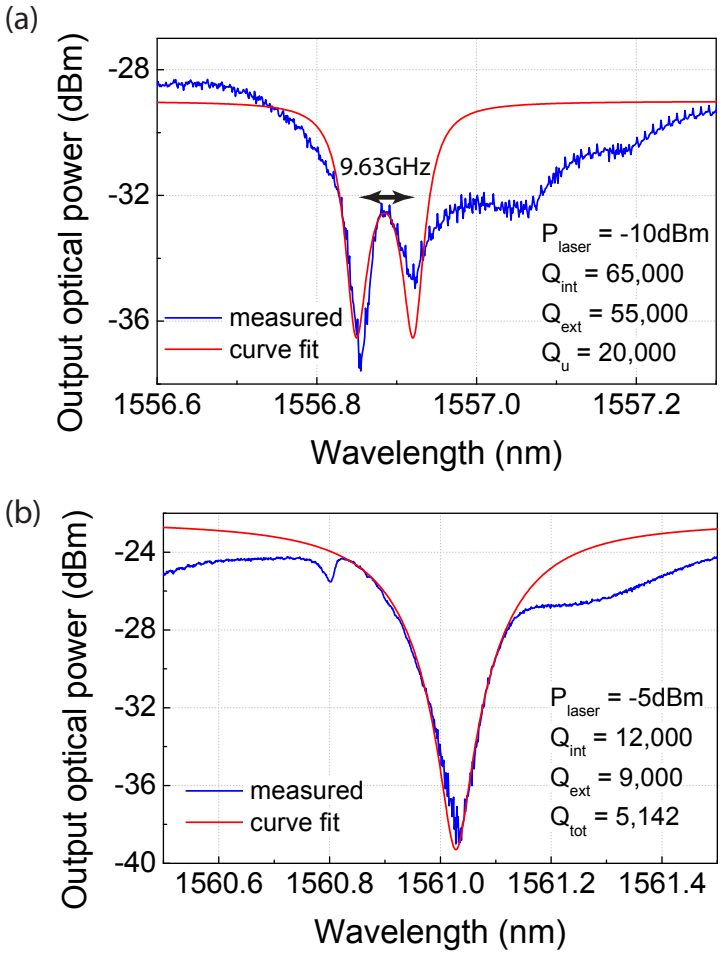

Figure E.4: (a) A split optical resonance for the silicon coupled ring resonator. The frequency difference between the two resonances in the optical doublet is 9.63GHz. (b) A singlet optical resonance for the silicon coupled ring resonator with loaded optical quality factor ≈5,000.

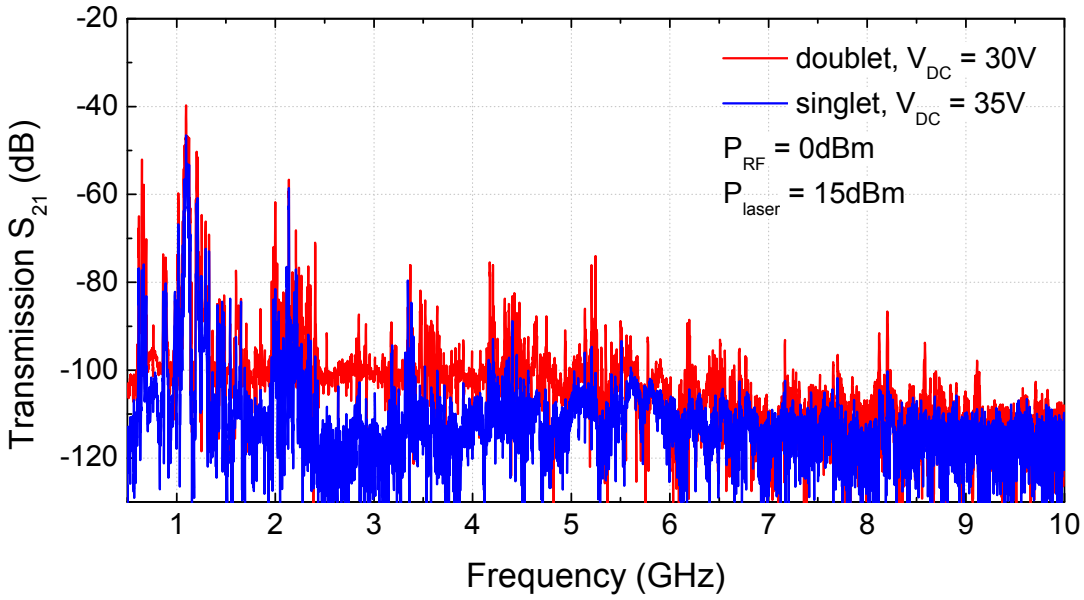

Figure E.5: Wide electromechanical transmission spectrum for the coupled ring resonator. The signals at higher frequencies have larger amplitudes when we employ the optical doublet for sensing motion.

from 1.1GHz to 1GHz for the fundamental mode, from 4.4GHz to 4GHz for the fourth order mode and so on for each mode order. Notable signal strength enhancement is observed for the fourth order mode (32dB increase from -78dB to -46dB) and the sixth order mode (28dB increase from -90dB to -62dB) compared to a singlet resonance without ALD. The mass loading on account of ALD also lowers the mechanical quality factors (980 for the fourth order radial mode post-ALD, 3,500 pre-ALD). The amplitude of motion is directly proportional to the mechanical quality factor Q_{mech} and varies as inverse-squared power of the resonator-electrode gap g and the frequency Ω_{mech} $\left(U_0 \propto \frac{Q_{mech}}{\Omega_{mech} g^2}\right)$ as derived in equation D.7. The lowering of the mechanical quality factor counters the enhancement due to reduced gap and hence no improvement in signal strength is noticed at frequencies beyond 7GHz. The signal strength is largest at the mechanical resonance frequencies whose values are close to the frequency split in the optical resonances, on account of maximum

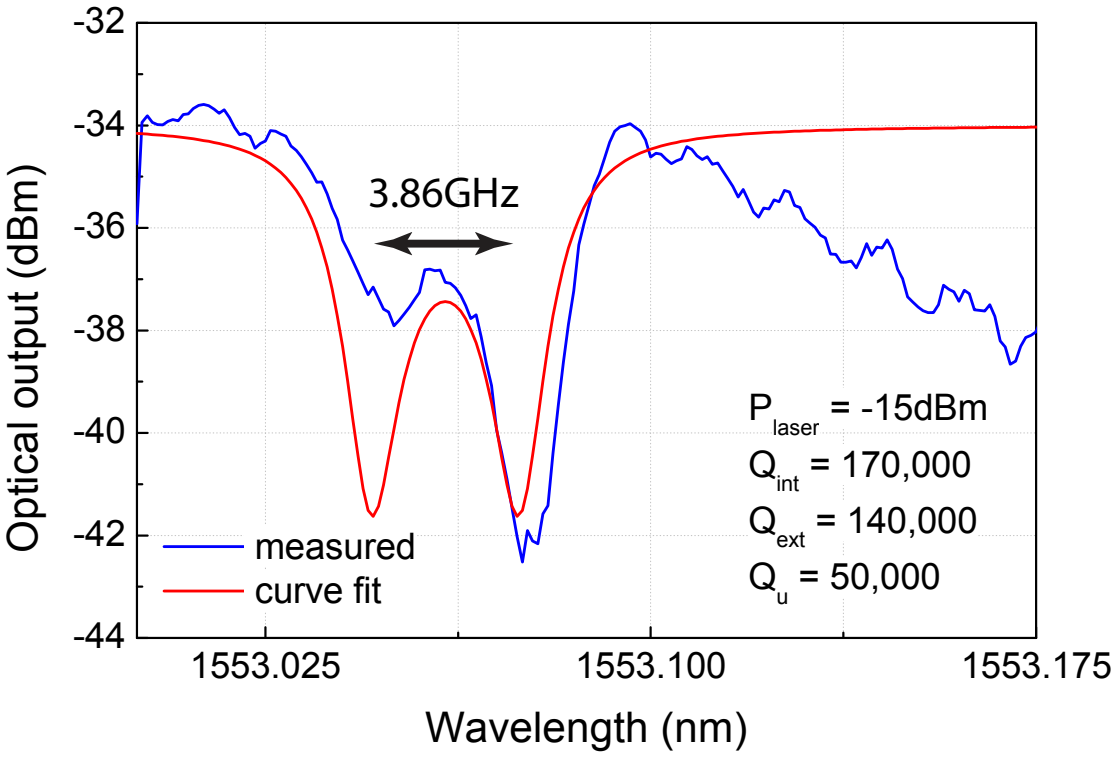

Figure E.6: A split optical resonance with a frequency splitting of 3.86GHz between the modes in a 50nm gap ALD coated 2-ring resonator.

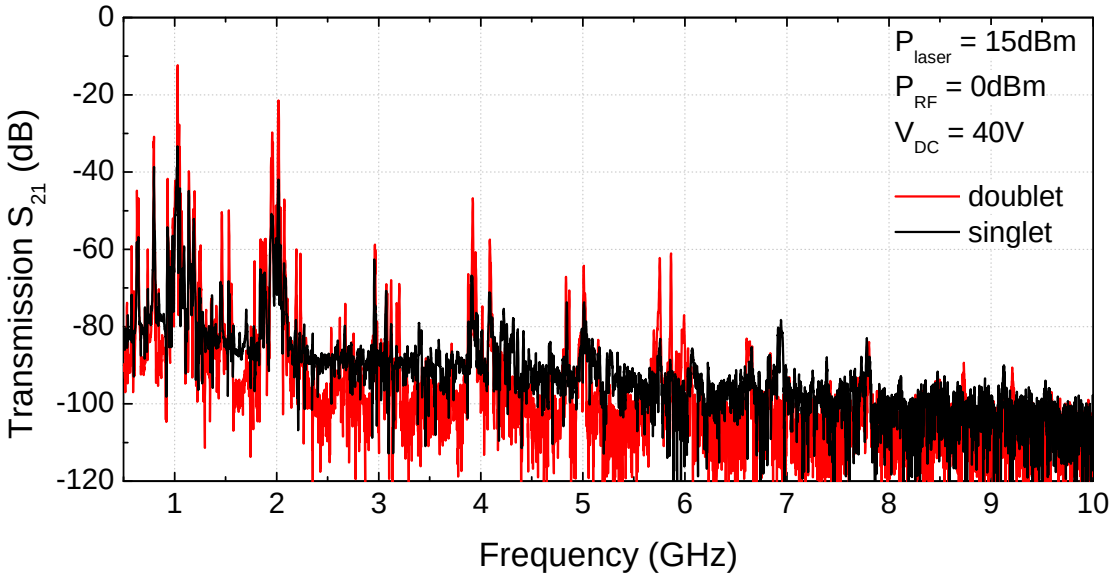

Figure E.7: Electromechanical transmission spectra for a 50nm gap resonator highlighting the efficacy of combining the doublet-based sensing scheme with a partial gap transduced drive scheme. The signal strength for the fourth order radial mode at 4GHz shows an improvement of 32dB over the signal recorded at 4.4GHz in Figure E.5 pre-ALD using a singlet resonance.

overlap of the Stokes sideband with the adjacent optical mode. This frequency split could be engineered via changing the resonator-waveguide gap using electrostatic transduction [124] thus providing a tunable mode selection mechanism. The universal nature of this sense scheme could also potentially push other transduction mechanisms such as piezo-opto-mechanical and all optical schemes to frequencies in the microwave X-band, thereby adding to the vast variety of experiments that could be realized using opto-mechanics.

BIBLIOGRAPHY

[1] M. Frerking, "Fifty years of progress in quartz crystal frequency standards," in *Frequency Control Symposium, 1996. 50th., Proceedings of the 1996 IEEE International.*, 1996, pp. 33–46.

[2] S. Fujishima, "The history of ceramic filters," *Ultrasonics, Ferroelectrics and Frequency Control, IEEE Transactions on*, vol. 47, no. 1, pp. 1–7, 2000.

[3] J. T. M. van Beek and R. Puers, "A review of mems oscillators for frequency reference and timing applications," *Journal of Micromechanics and Microengineering*, vol. 22, no. 1, p. 013001, 2012. [Online]. Available: http://stacks.iop.org/0960-1317/22/i=1/a=013001

[4] L. S. Lacaita A and S. C, *Integrated Frequency Synthesizers for Wireless Systems.* Cambridge: Cambridge University Press, 2007.

[5] C.-C. Nguyen, "Mems technology for timing and frequency control," *Ultrasonics, Ferroelectrics and Frequency Control, IEEE Transactions on*, vol. 54, no. 2, pp. 251–270, 2007.

[6] C. S. Lam, "A review of the recent development of mems and crystal oscillators and their impacts on the frequency control products industry," in *Ultrasonics Symposium, 2008. IUS 2008. IEEE*, 2008, pp. 694–704.

[7] S. Tabatabaei and A. Partridge, "Silicon mems oscillators for high-speed digital systems," *Micro, IEEE*, vol. 30, no. 2, pp. 80–89, 2010.

[8] C. Enz, J. Baborowski, J. Chabloz, M. Kucera, C. Muller, D. Ruffieux, and N. Scolari, "Ultra low-power mems-based radio for wireless sensor networks," in *Circuit Theory and Design, 2007. ECCTD 2007. 18th European Conference on*, 2007, pp. 320–331.

[9] G. Ho, K. Sundaresan, S. Pourkamali, and F. Ayazi, "Temperature compensated ibar reference oscillators," in *Micro Electro Mechanical Systems, 2006. MEMS 2006 Istanbul. 19th IEEE International Conference on*, 2006, pp. 910–913.

[10] Y.-W. Lin, S.-S. Li, Z. Ren, and C.-C. Nguyen, "Low phase noise array-composite micromechanical wine-glass disk oscillator," in *Electron Devices Meeting, 2005. IEDM Technical Digest. IEEE International*, 2005, pp. 4 pp.–281.

[11] S. Sridaran and S. Bhave, "1.12ghz opto-acoustic oscillator," in *Micro Electro Mechanical Systems (MEMS), 2012 IEEE 25th International Conference on*, 2012, pp. 664–667.

[12] B. Otis and J. Rabaey, "A 300μw 1.9-ghz cmos oscillator utilizing micromachined resonators," *Solid-State Circuits, IEEE Journal of*, vol. 38, no. 7, pp. 1271–1274, 2003.

[13] S. Rai, Y. Su, A. Dobos, R. Kim, R. Ruby, W. Pang, and B. Otis, "A 1.5ghz cmos/fbar frequency reference with $\pm$10ppm temperature stability," in *Frequency Control Symposium, 2009 Joint with the 22nd European Frequency and Time forum. IEEE International*, 2009, pp. 385–387.

[14] R. Ruby, "Positioning fbar technology in the frequency and timing domain," in *Frequency Control and the European Frequency and Time Forum (FCS), 2011 Joint Conference of the IEEE International*, 2011, pp. 1–10.

[15] C. Zuo, J. van der Spiegel, and G. Piazza, "1.05 ghz mems oscillator based on lateral-field-excited piezoelectric aln resonators," in *Frequency Control Symposium, 2009 Joint with the 22nd European Frequency and Time forum. IEEE International*, 2009, pp. 381–384.

[16] C. Zuo, J. V. der Spiegel, and G. Piazza, "Switch-less dual-frequency reconfigurable cmos oscillator using one single piezoelectric aln mems resonator with co-existing s0 and s1 lamb-wave modes," in *Micro Electro Mechanical Systems (MEMS), 2011 IEEE 24th International Conference on*, 2011, pp. 177–180.

[17] S. Bhave, "Hybrid mems resonators and oscillators," in *Frequency Control and the European Frequency and Time Forum (FCS), 2011 Joint Conference of the IEEE International*, 2011, pp. 1–6.

[18] H. Chandrahalim, D. Weinstein, L. F. Cheow, and S. Bhave, "Channel-select micromechanical filters using high-k dielectrically transduced mems resonators," in *Micro Electro Mechanical Systems, 2006. MEMS 2006 Istanbul. 19th IEEE International Conference on*, 2006, pp. 894–897.

[19] W. Wang and D. Weinstein, "Deep trench capacitor drive of a 3.3 ghz unreleased si mems resonator," in *Electron Devices Meeting (IEDM), 2012 IEEE International*, 2012, pp. 15.1.1–15.1.4.

[20] D. Weinstein and S. A. Bhave, "The resonant body transistor," *Nano*

Letters, vol. 10, no. 4, pp. 1234–1237, 2010, pMID: 20180594. [Online]. Available: http://pubs.acs.org/doi/abs/10.1021/nl9037517

[21] W. Wang, L. Popa, R. Marathe, and D. Weinstein, "An unreleased mm-wave resonant body transistor," in *Micro Electro Mechanical Systems (MEMS), 2011 IEEE 24th International Conference on*, 2011, pp. 1341–1344.

[22] E. Hwang, A. Driscoll, and S. Bhave, "Platform for jfet-based sensing of rf mems resonators in cmos technology," in *Electron Devices Meeting (IEDM), 2011 IEEE International*, 2011, pp. 20.4.1–20.4.4.

[23] E. Hwang and S. Bhave, "Transduction of high-frequency micromechanical resonators using depletion forces in p-n diodes," *Electron Devices, IEEE Transactions on*, vol. 58, no. 8, pp. 2770–2776, 2011.

[24] C. Rembe and R. Muller, "Measurement system for full three-dimensional motion characterization of mems," *Microelectromechanical Systems, Journal of*, vol. 11, no. 5, pp. 479–488, 2002.

[25] J. V. Knuuttila, P. T. Tikka, and M. M. Salomaa, "Scanning michelson interferometer for imaging surface acoustic wave fields," *Opt. Lett.*, vol. 25, no. 9, pp. 613–615, May 2000. [Online]. Available: http://ol.osa.org/abstract.cfm?URI=ol-25-9-613

[26] H. Chandrahalim, S. Bhave, R. Polcawich, J. Pulskamp, B. Pourat, S. Boedecker, and C. Rembe, "Heterodyne laser-doppler interferometric characterization of contour-mode resonators above 1 ghz," in *Ultrasonics Symposium (IUS), 2009 IEEE International*, 2009, pp. 1044–1049.

[27] V. B. Braginsky, *Measurement of Weak Forces in Physics Experiments*. University of Chicago Press, Chicago, 1977.

[28] T. J. Kippenberg and K. J. Vahala, "Cavity opto-mechanics," *Opt. Express*, vol. 15, no. 25, pp. 17 172–17 205, Dec 2007. [Online]. Available: http://www.opticsexpress.org/abstract.cfm?URI=oe-15-25-17172

[29] A. Cho, "Putting light's light touch to work as optics meets mechanics," *Science*, vol. 328, no. 5980, pp. 812–813, 2010. [Online]. Available: http://www.sciencemag.org/content/328/5980/812.short

[30] L. Ding, C. Baker, P. Senellart, A. Lemaitre, S. Ducci, G. Leo, and I. Favero, "High frequency gaas nano-optomechanical disk resonator,"

Phys. Rev. Lett., vol. 105, p. 263903, Dec 2010. [Online]. Available: http://link.aps.org/doi/10.1103/PhysRevLett.105.263903

[31] Z. Hao, S. Pourkamali, and F. Ayazi, "Vhf single-crystal silicon elliptic bulk-mode capacitive disk resonators-part i: design and modeling," *Microelectromechanical Systems, Journal of*, vol. 13, no. 6, pp. 1043–1053, 2004.

[32] J. Rosenberg, Q. Lin, and O. Painter, "Static and dynamic wavelength routing via the gradient optical force," *Nature photonics*, vol. 3, pp. 478–483, July 2009.

[33] M. Hossein-Zadeh, H. Rokhsari, A. Hajimiri, and K. J. Vahala, "Characterization of a radiation-pressure-driven micromechanical oscillator," *Phys. Rev. A*, vol. 74, p. 023813, Aug 2006. [Online]. Available: http://link.aps.org/doi/10.1103/PhysRevA.74.023813

[34] S. Tallur, S. Sridaran, S. Bhave, and T. Carmon, "Phase noise modeling of opto-mechanical oscillators," in *Frequency Control Symposium (FCS), 2010 IEEE International*, 2010, pp. 268–272.

[35] Q. Lin, J. Rosenberg, X. Jiang, K. J. Vahala, and O. Painter, "Mechanical oscillation and cooling actuated by the optical gradient force," *Phys. Rev. Lett.*, vol. 103, p. 103601, Aug 2009. [Online]. Available: http://link.aps.org/doi/10.1103/PhysRevLett.103.103601

[36] Q. P. Unterreithmeier, E. M. Weig, and J. P. Kotthaus, "Universal transduction scheme for nanomechanical systems based on dielectric forces," *Nature*, vol. 458, pp. 1001–1004, April 2009.

[37] M. Tomes and T. Carmon, "Photonic micro-electromechanical systems vibrating at x-band (11-ghz) rates," *Phys. Rev. Lett.*, vol. 102, p. 113601, Mar 2009. [Online]. Available: http://link.aps.org/doi/10.1103/PhysRevLett.102.113601

[38] H. Shin, W. Qiu, R. Jarecki, J. A. Cox, R. H. O. III, A. Starbuck, Z. Wang, and P. T. Rakich, "Tailorable stimulated brillouin scattering in nanoscale silicon waveguides," *Nature Communications*, vol. 4, p. 1944, June 2013.

[39] J. Li, H. Lee, T. Chen, and K. J. Vahala, "Characterization of a high coherence, brillouin microcavity laser on silicon," *Opt. Express*, vol. 20, no. 18, pp. 20 170–20 180, Aug 2012. [Online]. Available: http://www.opticsexpress.org/abstract.cfm?URI=oe-20-18-20170

[40] A. A. Savchenkov, A. B. Matsko, V. S. Ilchenko, D. Seidel, and L. Maleki, "Surface acoustic wave opto-mechanical oscillator and frequency comb generator," *Opt. Lett.*, vol. 36, no. 17, pp. 3338–3340, Sep 2011. [Online]. Available: http://ol.osa.org/abstract.cfm?URI=ol-36-17-3338

[41] M. Eichenfield, J. Chan, R. M. Camacho, K. J. Vahala, and O. Painter, "Optomechanical crystals," *Nature*, vol. 462, pp. 78–82, October 2009.

[42] W. C. Jiang, X. Lu, J. Zhang, and Q. Lin, "High-frequency silicon optomechanical oscillator with an ultralow threshold," *Opt. Express*, vol. 20, no. 14, pp. 15 991–15 996, Jul 2012. [Online]. Available: http://www.opticsexpress.org/abstract.cfm?URI=oe-20-14-15991

[43] G. S. Wiederhecker, L. Chen, A. A. Gondarenko, and M. Lipson, "Controlling photonic structures using optical forces," *Nature*, vol. 462, pp. 633–636, November 2009.

[44] A. Gondarenko, J. S. Levy, and M. Lipson, "High confinement micron-scale silicon nitride high q ring resonator," *Opt. Express*, vol. 17, no. 14, pp. 11 366–11 370, Jul 2009. [Online]. Available: http://www.opticsexpress.org/abstract.cfm?URI=oe-17-14-11366

[45] S. S. Verbridge, J. M. Parpia, R. B. Reichenbach, L. M. Bellan, and H. G. Craighead, "High quality factor resonance at room temperature with nanostrings under high tensile stress," *Journal of Applied Physics*, vol. 99, no. 12, p. 124304, 2006. [Online]. Available: http://link.aip.org/link/?JAP/99/124304/1

[46] M. I. Cheema and A. G. Kirk, "Accurate determination of the quality factor and tunneling distance of axisymmetric resonators for biosensing applications," *Opt. Express*, vol. 21, no. 7, pp. 8724–8735, Apr 2013. [Online]. Available: http://www.opticsexpress.org/abstract.cfm?URI=oe-21-7-8724

[47] Q. Wang, Y. Huang, T.-H. Loh, D. K. T. Ng, and S.-T. Ho, "Thin-film stack based integrated grin coupler with aberration-free focusing and super-high na for efficient fiber-to-nanophotonic-chip coupling," *Opt. Express*, vol. 18, no. 5, pp. 4574–4589, Mar 2010. [Online]. Available: http://www.opticsexpress.org/abstract.cfm?URI=oe-18-5-4574

[48] C. Doerr, L. Chen, Y.-K. Chen, and L. Buhl, "Wide bandwidth silicon nitride grating coupler," *Photonics Technology Letters, IEEE*, vol. 22, no. 19, pp. 1461–1463, 2010.

[49] X. Chen and H.-K. Tsang, "Nanoholes grating couplers for coupling between silicon-on-insulator waveguides and optical fibers," *Photonics Journal, IEEE*, vol. 1, no. 3, pp. 184–190, 2009.

[50] D. Geuzebroek, E. Klein, H. Kelderman, F. Tan, D. Klunder, and A. Driessen, "Thermally tuneable, wide fsr switch based on micro-ring resonators," in *IEEE/LEOS Benelux Chapter 2002 Annual Symposium*, T. D. Visser, D. Lenstra, and H. F. Schouten, Eds. Amsterdam, the Netherlands: Vrije Universiteit Amsterdam, 2002, pp. 155–158. [Online]. Available: http://doc.utwente.nl/58195/

[51] D. Leeson, "A simple model of feedback oscillator noise spectrum," *Proceedings of the IEEE*, vol. 54, no. 2, pp. 329–330, 1966.

[52] X. Sun, X. Zhang, M. Poot, C. Xiong, and H. X. Tang, "A superhigh-frequency optoelectromechanical system based on a slotted photonic crystal cavity," *Applied Physics Letters*, vol. 101, no. 22, pp. 221 116–221 116–5, 2012.

[53] S. Sridaran and S. A. Bhave, "Electrostatic actuation of silicon optomechanical resonators," *Opt. Express*, vol. 19, no. 10, pp. 9020–9026, May 2011. [Online]. Available: http://www.opticsexpress.org/abstract.cfm?URI=oe-19-10-9020

[54] S. Wang, S. Chandorkar, A. Graham, M. Messana, J. Salvia, and T. Kenny, "Encapsulated mechanically coupled fully-differential breathe-mode ring filters with ultra-narrow bandwidth," in *Solid-State Sensors, Actuators and Microsystems Conference (TRANSDUCERS), 2011 16th International*, 2011, pp. 942–945.

[55] C. Huang, J. Fan, R. Zhang, and L. Zhu, "Internal frequency mixing in a single optomechanical resonator," *Applied Physics Letters*, vol. 101, no. 23, p. 231112, 2012. [Online]. Available: http://link.aip.org/link/?APL/101/231112/1

[56] W.-T. Hsu and K. Cioffi, "Low phase noise 70 mhz micromechanical reference oscillators," in *Microwave Symposium Digest, 2004 IEEE MTT-S International*, vol. 3, 2004, pp. 1927–1930 Vol.3.

[57] J. Salvia, R. Melamud, S. A. Chandorkar, S. Lord, and T. Kenny, "Real-time temperature compensation of mems oscillators using an integrated micro-oven and a phase-locked loop," *Microelectromechanical Systems, Journal of*, vol. 19, no. 1, pp. 192–201, 2010.

[58] A. Samarao and F. Ayazi, "Combined capacitive and piezoelectric transduction for high performance silicon microresonators," in *Micro Electro Mechanical Systems (MEMS), 2011 IEEE 24th International Conference on*, 2011, pp. 169–172.

[59] L.-W. Hung and C.-C. Nguyen, "Capacitive-piezoelectric aln resonators with q >12,000," in *Micro Electro Mechanical Systems (MEMS), 2011 IEEE 24th International Conference on*, 2011, pp. 173–176.

[60] T. Rocheleau, T. Naing, Z. Ren, and C.-C. Nguyen, "Acoustic whispering gallery mode resonator with q>109,000 at 515mhz," in *Micro Electro Mechanical Systems (MEMS), 2012 IEEE 25th International Conference on*, 2012, pp. 672–675.

[61] Y. Xie, *Micromechanical Extensional Wine-Glass Mode Ring Resonators For Wireless Communications*. University of Michigan., 2006. [Online]. Available: http://books.google.com/books?id=VzyfVaHEVgQC

[62] R. Tabrizian, M. Rais-Zadeh, and F. Ayazi, "Effect of phonon interactions on limiting the f.q product of micromechanical resonators," in *Solid-State Sensors, Actuators and Microsystems Conference, 2009. TRANSDUCERS 2009. International*, 2009, pp. 2131–2134.

[63] P. G. Steeneken, J. J. M. Ruigrok, S. Kang, J. T. M. van Beek, J. Bontemps, and J. J. Koning, "Parameter Extraction and Support-Loss in MEMS Resonators," *ArXiv e-prints*, Apr. 2013.

[64] T. Roszhart, "The effect of thermoelastic internal friction on the q of micromachined silicon resonators," in *Solid-State Sensor and Actuator Workshop, 1990. 4th Technical Digest., IEEE*, 1990, pp. 13–16.

[65] A. Duwel, R. Candler, T. Kenny, and M. Varghese, "Engineering mems resonators with low thermoelastic damping," *Microelectromechanical Systems, Journal of*, vol. 15, no. 6, pp. 1437–1445, 2006.

[66] R. Lifshitz and M. L. Roukes, "Thermoelastic damping in micro- and nanomechanical systems," *Phys. Rev. B*, vol. 61, pp. 5600–5609, Feb 2000. [Online]. Available: http://link.aps.org/doi/10.1103/PhysRevB.61.5600

[67] M. Demirci and C.-C. Nguyen, "Mechanically corner-coupled square microresonator array for reduced series motional resistance," *Microelectromechanical Systems, Journal of*, vol. 15, no. 6, pp. 1419–1436, 2006.

[68] Y. Lin, W.-C. Li, I. Gurin, S.-S. Li, Y.-W. Lin, Z. Ren, B. Kim, and C.-C. Nguyen, "Digitally-specified micromechanical displacement amplifiers," in *Solid-State Sensors, Actuators and Microsystems Conference, 2009. TRANSDUCERS 2009. International*, 2009, pp. 781–784.

[69] S. Pourkamali, G. Ho, and F. Ayazi, "Low-impedance vhf and uhf capacitive silicon bulk acoustic-wave resonators - part ii: Measurement and characterization," *Electron Devices, IEEE Transactions on*, vol. 54, no. 8, pp. 2024–2030, 2007.

[70] Y.-W. Lin, S.-S. Li, Z. Ren, and C.-C. Nguyen, "Low phase noise array-composite micromechanical wine-glass disk oscillator," in *Electron Devices Meeting, 2005. IEDM Technical Digest. IEEE International*, 2005, pp. 4 pp.–281.

[71] T. Cheng and S. Bhave, "High-q, low impedance polysilicon resonators with 10 nm air gaps," in *Micro Electro Mechanical Systems (MEMS), 2010 IEEE 23rd International Conference on*, 2010, pp. 695–698.

[72] D. Weinstein and S. Bhave, "Internal dielectric transduction in bulk-mode resonators," *Microelectromechanical Systems, Journal of*, vol. 18, no. 6, pp. 1401–1408, 2009.

[73] V. Kaajakari, A. Alastalo, and T. Mattila, "Electrostatic transducers for micromechanical resonators: free space and solid dielectric," *Ultrasonics, Ferroelectrics and Frequency Control, IEEE Transactions on*, vol. 53, no. 12, pp. 2484–2489, 2006.

[74] M. Akgul, B. Kim, Z. Ren, and C. T.-C. Nguyen, "Capacitively transduced micromechanical resonators with simultaneous low motional resistance and q>70,000," *Tech. Digest 2008 Solid-State Sensor, Actuator, and Microsystems Workshop, Hilton Head, South Carolina*, pp. 6–10, 2008.

[75] K. Wang and C.-C. Nguyen, "High-order medium frequency micromechanical electronic filters," *Microelectromechanical Systems, Journal of*, vol. 8, no. 4, pp. 534–556, 1999.

[76] A. Hajimiri, "Noise in phase-locked loops," in *Mixed-Signal Design, 2001. SSMSD. 2001 Southwest Symposium on*, 2001, pp. 1–6.

[77] X. S. Yao and L. Maleki, "Optoelectronic microwave oscillator," *J. Opt. Soc. Am. B*, vol. 13, no. 8, pp. 1725–1735, Aug 1996. [Online]. Available: http://josab.osa.org/abstract.cfm?URI=josab-13-8-1725

[78] E. C. Levy, M. Horowitz, and C. R. Menyuk, "Modeling optoelectronic oscillators," *J. Opt. Soc. Am. B*, vol. 26, no. 1, pp. 148–159, Jan 2009. [Online]. Available: http://josab.osa.org/abstract.cfm?URI=josab-26-1-148

[79] L. Maleki, "Sources: The optoelectronic oscillator," *Nature Photonics*, no. 5, pp. 728–730, 2011. [Online]. Available: http://www.nature.com/nphoton/journal/v5/n12/full/nphoton.2011.293.html

[80] G. Li and E. Afshari, "A distributed dual-band lc oscillator based on mode switching," *Microwave Theory and Techniques, IEEE Transactions on*, vol. 59, no. 1, pp. 99–107, 2011.

[81] M. Metcalfe, S. M. Carr, A. Muller, G. S. Solomon, and J. Lawall, "Resolved sideband emission of InAs/GaAs quantum dots strained by surface acoustic waves," *Phys. Rev. Lett.*, vol. 105, p. 037401, Jul 2010. [Online]. Available: http://link.aps.org/doi/10.1103/PhysRevLett.105.037401

[82] T. J. Kippenberg, R. Holzwarth, and S. A. Diddams, "Microresonator-based optical frequency combs," *Science*, vol. 332, no. 6029, pp. 555–559, 2011. [Online]. Available: http://www.sciencemag.org/content/332/6029/555.abstract

[83] B. Jalali, V. Raghunathan, D. Dimitropoulos, and O. Boyraz, "Raman-based silicon photonics," *Selected Topics in Quantum Electronics, IEEE Journal of*, vol. 12, no. 3, pp. 412–421, 2006.

[84] R. Espinola, J. Dadap, J. Richard Osgood, S. McNab, and Y. Vlasov, "C-band wavelength conversion in silicon photonic wire waveguides," *Opt. Express*, vol. 13, no. 11, pp. 4341–4349, May 2005. [Online]. Available: http://www.opticsexpress.org/abstract.cfm?URI=oe-13-11-4341

[85] H. Fukuda, K. Yamada, T. Shoji, M. Takahashi, T. Tsuchizawa, T. Watanabe, J. ichi Takahashi, and S. ichi Itabashi, "Four-wave mixing in silicon wire waveguides," *Opt. Express*, vol. 13, no. 12, pp. 4629–4637, Jun 2005. [Online]. Available: http://www.opticsexpress.org/abstract.cfm?URI=oe-13-12-4629

[86] Q. Xu, V. R. Almeida, and M. Lipson, "Micrometer-scale all-optical wavelength converter on silicon," *Opt. Lett.*, vol. 30, no. 20, pp. 2733–2735, Oct 2005. [Online]. Available: http://ol.osa.org/abstract.cfm?URI=ol-30-20-2733

[87] A. Schliesser, R. Riviere, G. Anetsberger, O. Arcizet, and T. J. Kippenberg,

"Resolved-sideband cooling of a micromechanical oscillator," *Nature Physics*, no. 4, pp. 415–419, April 2008.

[88] J. Chan, T. P. M. Alegre, A. H. Safavi-Naeini, J. T. Hill, A. Krause, S. Groblacher, M. Aspelmeyer, and O. Painter, "Laser cooling of a nanomechanical oscillator into its quantum ground state," *Nature*, no. 478, pp. 89–92, October 2011.

[89] F. Massel, T. T. Heikkila, J.-M. Pirkkalainen, S. U. Cho, H. Saloniemi, P. J. Hakonen, and M. A. Sillanpaa, "Microwave amplification with nanomechanical resonators," *Nature*, no. 480, pp. 351–354, December 2011.

[90] D. W. C. Brooks, T. Botter, S. Schreppler, T. P. Purdy, N. Brahms, and D. M. Stamper-Kurn, "Non-classical light generated by quantum-noise-driven cavity optomechanics," *Nature*, no. 488, pp. 476–480, August 2012.

[91] C. Dong, V. Fiore, M. C. Kuzyk, and H. Wang, "Optomechanical dark mode," *Science*, vol. 338, no. 6114, pp. 1609–1613, 2012. [Online]. Available: http://www.sciencemag.org/content/338/6114/1609.abstract

[92] J. T. Hill, A. H. Safavi-Naeini, J. Chan, and O. Painter, "Coherent optical wavelength conversion via cavity optomechanics," *Nature Communications*, no. 3, p. 1196, November 2012.

[93] H. Li, Y. Chen, J. Noh, S. Tadesse, and M. Li, "Multichannel cavity optomechanics for all-optical amplification of radio frequency signals," *Nature Communications*, no. 3, p. 1091, October 2012.

[94] G. Agrawal, *Fiber-Optic Communication Systems*, ser. Wiley Series in Microwave and Optical Engineering. Wiley, 2012. [Online]. Available: http://books.google.com/books?id=yGQ4n1-r2eQC

[95] L.-M. Duan, M. D. Lukin, J. I. Cirac, and P. Zoller, "Long-distance quantum communication with atomic ensembles and linear optics," *Nature*, no. 414, p. 1091, September 2001.

[96] A. H. Safavi-Naeini and O. Painter, "Proposal for an optomechanical traveling wave phononphoton translator," *New Journal of Physics*, vol. 13, no. 1, p. 013017, 2011. [Online]. Available: http://stacks.iop.org/1367-2630/13/i=1/a=013017

[97] M. Davanço, J. Chan, A. H. Safavi-Naeini, O. Painter, and K. Srini-

vasan, "Slot-mode-coupled optomechanical crystals," *Opt. Express*, vol. 20, no. 22, pp. 24 394–24 410, Oct 2012. [Online]. Available: http://www.opticsexpress.org/abstract.cfm?URI=oe-20-22-24394

[98] T. Baehr-Jones, T. Pinguet, P. L. Guo-Qiang, S. Danziger, D. Prather, and M. Hochberg, "Myths and rumours of silicon photonics," *Nature Photonics*, no. 6, pp. 206–208, March 2012.

[99] J. S. Orcutt, B. Moss, C. Sun, J. Leu, M. Georgas, J. Shainline, E. Zgraggen, H. Li, J. Sun, M. Weaver, S. Urošević, M. Popović, R. J. Ram, and V. Stojanović, "Open foundry platform for high-performance electronic-photonic integration," *Opt. Express*, vol. 20, no. 11, pp. 12 222–12 232, May 2012. [Online]. Available: http://www.opticsexpress.org/abstract.cfm?URI=oe-20-11-12222

[100] M. W. Geis, S. J. Spector, M. E. Grein, J. U. Yoon, D. M. Lennon, and T. M. Lyszczarz, "Silicon waveguide infrared photodiodes with >35 ghz bandwidth and phototransistors with 50 aw-1 response," *Opt. Express*, vol. 17, no. 7, pp. 5193–5204, Mar 2009. [Online]. Available: http://www.opticsexpress.org/abstract.cfm?URI=oe-17-7-5193

[101] K. Preston, Y. H. D. Lee, M. Zhang, and M. Lipson, "Waveguide-integrated telecom-wavelength photodiode in deposited silicon," *Opt. Lett.*, vol. 36, no. 1, pp. 52–54, Jan 2011. [Online]. Available: http://ol.osa.org/abstract.cfm?URI=ol-36-1-52

[102] C. T. DeRose, D. C. Trotter, W. A. Zortman, A. L. Starbuck, M. Fisher, M. R. Watts, and P. S. Davids, "Ultra compact 45 ghz cmos compatible germanium waveguide photodiode with low dark current," *Opt. Express*, vol. 19, no. 25, pp. 24 897–24 904, Dec 2011. [Online]. Available: http://www.opticsexpress.org/abstract.cfm?URI=oe-19-25-24897

[103] B. J. M. Hausmann, I. B. Bulu, P. B. Deotare, M. McCutcheon, V. Venkataraman, M. L. Markham, D. J. Twitchen, and M. Lonar, "Integrated high-quality factor optical resonators in diamond," *Nano Letters*, vol. 13, no. 5, pp. 1898–1902, 2013. [Online]. Available: http://pubs.acs.org/doi/abs/10.1021/nl3037454

[104] V. Fiore, Y. Yang, M. C. Kuzyk, R. Barbour, L. Tian, and H. Wang, "Storing optical information as a mechanical excitation in a silica optomechanical resonator," *Phys. Rev. Lett.*, vol. 107, p. 133601, Sep 2011. [Online]. Available: http://link.aps.org/doi/10.1103/PhysRevLett.107.133601

[105] M. Poot, K. Y. Fong, M. Bagheri, W. H. P. Pernice, and H. X. Tang, "Backaction limits on self-sustained optomechanical oscillations," *Phys. Rev. A*, vol. 86, p. 053826, Nov 2012. [Online]. Available: http://link.aps.org/doi/10.1103/PhysRevA.86.053826

[106] G. I. Harris, U. L. Andersen, J. Knittel, and W. P. Bowen, "Feedback-enhanced sensitivity in optomechanics: Surpassing the parametric instability barrier," *Phys. Rev. A*, vol. 85, p. 061802, Jun 2012. [Online]. Available: http://link.aps.org/doi/10.1103/PhysRevA.85.061802

[107] Y. Okawachi, K. Saha, J. S. Levy, Y. H. Wen, M. Lipson, and A. L. Gaeta, "Octave-spanning frequency comb generation in a silicon nitride chip," *Opt. Lett.*, vol. 36, no. 17, pp. 3398–3400, Sep 2011. [Online]. Available: http://ol.osa.org/abstract.cfm?URI=ol-36-17-3398

[108] K. Saha, Y. Okawachi, B. Shim, J. S. Levy, R. Salem, A. R. Johnson, M. A. Foster, M. R. E. Lamont, M. Lipson, and A. L. Gaeta, "Modelocking and femtosecond pulse generation in chip-based frequency combs," *Opt. Express*, vol. 21, no. 1, pp. 1335–1343, Jan 2013. [Online]. Available: http://www.opticsexpress.org/abstract.cfm?URI=oe-21-1-1335

[109] W. Wang and D. Weinstein, "Acoustic bragg reflectors for q-enhancement of unreleased mems resonators," in *Frequency Control and the European Frequency and Time Forum (FCS), 2011 Joint Conference of the IEEE International*, 2011, pp. 1–6.

[110] P. Del'Haye, S. B. Papp, and S. A. Diddams, "Hybrid electro-optically modulated microcombs," *Phys. Rev. Lett.*, vol. 109, p. 263901, Dec 2012. [Online]. Available: http://link.aps.org/doi/10.1103/PhysRevLett.109.263901

[111] D. M. Rozelle, "The hemispherical resonator gyro: From wineglass to the planets," in *Proceedings of the 19th AAS/AIAA Space Flight Mechanics Meeting*, 2009, pp. 1157–1178.

[112] L. Fegely, D. Hutchison, and S. Bhave, "Isotropic etching of 111 scs for wafer-scale manufacturing of perfectly hemispherical silicon molds," in *Solid-State Sensors, Actuators and Microsystems Conference (TRANSDUCERS), 2011 16th International*, 2011, pp. 2295–2298.

[113] E. Eklund and A. Shkel, "Glass blowing on a wafer level," *Microelectromechanical Systems, Journal of*, vol. 16, no. 2, pp. 232–239, 2007.

[114] R. L. Kubena and D. T. Chang, "Disc resonator gyroscopes," 2009, uS Patent 7,581,443.

[115] J. Bochmann, A. Vainsencher, D. D. Awschalom, and A. N. Cleland, "Nanomechanical coupling between microwave and optical photons," *Nature Physics*, 2013. [Online]. Available: http://www.nature.com/nphys/journal/vaop/ncurrent/full/nphys2748.html

[116] L. Ju, D. G. Blair, C. Zhao, S. Gras, Z. Zhang, P. Barriga, H. Miao, Y. Fan, and L. Merrill, "Strategies for the control of parametric instability in advanced gravitational wave detectors," *Classical and Quantum Gravity*, vol. 26, no. 1, p. 015002, 2009. [Online]. Available: http://stacks.iop.org/0264-9381/26/i=1/a=015002

[117] C. Metzger, I. Favero, A. Ortlieb, and K. Karrai, "Optical self cooling of a deformable fabry-perot cavity in the classical limit," *Phys. Rev. B*, vol. 78, p. 035309, Jul 2008. [Online]. Available: http://link.aps.org/doi/10.1103/PhysRevB.78.035309

[118] G. Anetsberger, E. Weig, J. Kotthaus, and T. Kippenberg, "Cavity optomechanics and cooling nanomechanical oscillators using microresonator enhanced evanescent near-field coupling," *Comptes Rendus Physique*, vol. 12, no. 910, pp. 800 – 816, 2011.

[119] T. Carmon, L. Yang, and K. Vahala, "Dynamical thermal behavior and thermal self-stability of microcavities," *Opt. Express*, vol. 12, no. 20, pp. 4742–4750, Oct 2004. [Online]. Available: http://www.opticsexpress.org/abstract.cfm?URI=oe-12-20-4742

[120] M. L. Gorodetsky, A. D. Pryamikov, and V. S. Ilchenko, "Rayleigh scattering in high-q microspheres," *J. Opt. Soc. Am. B*, vol. 17, no. 6, pp. 1051–1057, Jun 2000. [Online]. Available: http://josab.osa.org/abstract.cfm?URI=josab-17-6-1051

[121] M. Borselli, K. Srinivasan, P. E. Barclay, and O. Painter, "Rayleigh scattering, mode coupling, and optical loss in silicon microdisks," *Applied Physics Letters*, vol. 85, no. 17, pp. 3693–3695, 2004. [Online]. Available: http://link.aip.org/link/?APL/85/3693/1

[122] T. J. Kippenberg, S. M. Spillane, and K. J. Vahala, "Modal coupling in traveling-wave resonators," *Opt. Lett.*, vol. 27, no. 19, pp. 1669–1671, Oct 2002. [Online]. Available: http://ol.osa.org/abstract.cfm?URI=ol-27-19-1669

[123] Q. Li, Z. Zhang, F. Liu, M. Qiu, and Y. Su, "Dense wavelength conversion and multicasting in a resonance-split silicon microring," *Applied Physics Letters*, vol. 93, no. 8, p. 081113, 2008. [Online]. Available: http://link.aip.org/link/?APL/93/081113/1

[124] M.-C. Tien, S. Mathai, J. Yao, and M. Wu, "Tunable mems actuated microring resonators," in *Optical MEMS and Nanophotonics, 2007 IEEE/LEOS International Conference on*, 2007, pp. 177–178.